

Portland State University

PDXScholar

Dissertations and Theses

Dissertations and Theses

1-1-2010

Polyaniline Nanofibers as the Hole Transport Medium in an Inverse Dye-Sensitized Solar Cell

Ian Brock Hesselsweet
Portland State University

Follow this and additional works at: https://pdxscholar.library.pdx.edu/open_access_etds

Let us know how access to this document benefits you.

Recommended Citation

Hesselsweet, Ian Brock, "Polyaniline Nanofibers as the Hole Transport Medium in an Inverse Dye-Sensitized Solar Cell" (2010). *Dissertations and Theses*. Paper 710.

<https://doi.org/10.15760/etd.710>

This Dissertation is brought to you for free and open access. It has been accepted for inclusion in Dissertations and Theses by an authorized administrator of PDXScholar. Please contact us if we can make this document more accessible: pdxscholar@pdx.edu.

Polyaniline Nanofibers as the Hole Transport Medium in an Inverse
Dye-Sensitized Solar Cell

by

Ian Brock Hesselsweet

A dissertation submitted in partial fulfillment of the
requirements for the degree of

Doctor of Philosophy
in
Chemistry

Dissertation Committee:

Carl Wamser, Chair

Mingdi Yan

Shankar Rananavare

Robert Strongin

Rolf Könenkamp

Portland State University

© 2010

ABSTRACT

In order to become a viable alternative to silicon photovoltaics, dye-sensitized solar cells must overcome several issues primarily resulting from their use of a liquid electrolyte. Much research has gone into correcting these shortcomings by replacing the liquid electrolyte with solid-state hole-transport media. Using these solid-state materials brings new difficulties, such as completely filling the pores in the TiO₂ nanostructure, and achieving good adhesion with the dye-coated TiO₂. A novel approach to addressing these difficulties is the inverse dye-sensitized solar cell design. In this method the devices are constructed in reverse order, with the solid-state hole-transport medium providing the nanostructure instead of the TiO₂. This allows new materials and methods to be used which may better address these issues.

In this project, inverse dye-sensitized solar cells using polyaniline nanofibers as the hole transport medium were prepared and characterized. The devices were prepared on fluorine-doped tin oxide (FTO) coated glass electrodes. The first component was a dense spin-coated polyaniline blocking layer, to help prevent short circuiting of the devices. The second layer was a thin film of drop cast polyaniline nanofibers which acted as the hole transport medium and provided high surface area for the dye attachment. The dye used was 5,10,15,20-tetrakis(4-carboxyphenyl)porphyrin (TCPP), which was covalently attached to the nanofibers using a Friedel-Crafts acylation. Titania gel was then deposited into the pores of the

nanofiber film by controlled hydrolysis of a titanium complex (Tyzor LA). A back electrode of TiO₂ nanoparticles sintered on FTO was pressed on top to complete the devices. A typical device generated an open circuit voltage of 0.17 V and a closed circuit current of 5.7 nA/cm² while the highest open circuit voltage recorded for any variation on a device was 0.31 V and the highest short circuit current was 52 nA/cm² under AM 1.5 simulated solar spectrum at 100 mW/cm².

Initially prepared devices did not generate a measureable photocurrent due to two materials flaws. The first was traced to the poorly developed conduction band of the titania gel, as deposited from Tyzor LA hydrolysis, resulting in poor electron conduction. This prevented the titania gel from efficiently functioning as the electron transport medium. A remedy was found in adding a layer of sintered anatase TiO₂ nanoparticles on the back electrode to serve as the electron transport medium. However, this remedy does not address the issue of the inability of titania gel to efficiently transport electrons photogenerated deep in the nanofiber film to the back electrode. The second flaw was found to originate from fast recombination kinetics between electrons in TiO₂ and holes in polyaniline. However, a positive feature was that the titania gel intended to be used as the electron transport medium was found to sufficiently insulate the interface such that the recombination rate slowed enough to allow generation of a measureable photocurrent. Electronic insulation was further

enhanced by co-attaching decanoic acid onto the polyaniline nanofibers to fill in pinholes between the dye molecules.

While these solutions were not ideal, they were intended to be diagnostic in nature and supplied critical information about the weak links in the device design, thus pointing the way toward improving device performance. Significant enhancements can be expected by addressing these issues in further detail.

ACKNOWLEDGEMENTS

First, I would like to thank my dissertation advisor, Dr. Carl Wamser. I am grateful for his valuable guidance, input and encouragement. His knowledge and direction were critical to the success of my project.

The Wamser research group deserves much thanks as well, especially Keith James for his input, the critical pieces of information which helped bring breakthrough to my project, his friendship and great conversations and laughs. Also, Dr. Michael Walter gave me valuable input, direction, and instrument training. Thanks also to Dr. Brian Kim for providing me with essential background information on polyaniline in DSSCs.

Thanks to my dissertation committee, Dr. Mingdi Yan, Dr. Shankar Rananavare, Dr. Robert Strongin and Dr. Rolf Könenkamp for their valuable guidance. A special thanks to Dr. Rolf Könenkamp for his help in understanding semiconductor physics and troubleshooting my early nonfunctional devices.

Thank you to Aya Takase from Rigaku and Dr. Andrea Goforth for their assistance with powder XRD. Also thanks to Dr. Derek Nowak for his help with thermal evaporation of metal electrodes. Thank you to Jonathan Davies and Neelou Etesami for their valuable contributions, as summer researchers, to my project.

And a very special thanks to my beloved wife Andrea for all her love, support, guidance and patience. I could not have done this without you my love!

TABLE OF CONTENTS

ABSTRACT.....	i
ACKNOWLEDGEMENTS	iv
LIST OF TABLES	vii
LIST OF FIGURES	viii
LIST OF ABBREVIATIONS	xiii
CHAPTER 1. INTRODUCTION	1
1.1 Overview	1
1.2 History and Function of Dye-Sensitized Solar Cells (DSSCs).....	3
1.3 Polyaniline Nanofiber Inverse DSSC.....	8
1.4 Polyaniline Blocking Layer	12
1.5 Polyaniline Nanofibers as the Hole Transport Medium and Nanostructure Agent.....	13
1.6 Porphyrins as the Sensitizing Dye	18
1.7 TiO ₂ as the Electron Transport Medium	20
1.8 PCBM as the Electron Transport Medium	23
1.9 Photoactivity Characterization.....	24
CHAPTER 2. EXPERIMENTAL	28
2.1 Materials and Instruments	28
2.2 Casting the Polyaniline Blocking Layer	33

2.3 Synthesis and Deposition of Polyaniline Nanofibers.....	34
2.4 Porphyrin Attachment to Polyaniline Nanofibers.....	36
2.5 TiO ₂ Deposition and Conversion to Anatase.....	39
2.6 PCBM Casting.....	42
2.7 Back Electrode Preparation.....	42
2.8 Photoactivity Characterization.....	43
CHAPTER 3. RESULTS AND DISCUSSION	45
3.1 Polyaniline Blocking Layer	45
3.2 Polyaniline Nanofiber Layer.....	52
3.3 Porphyrin Attachment to Polyaniline Nanofibers.....	62
3.4 TiO ₂ Deposition and Conversion to Anatase.....	73
3.5 PCBM Casting.....	87
3.6 Back Electrode Preparation.....	90
3.7 Photoactivity Characterization.....	93
CHAPTER 4. CONCLUSIONS.....	115
REFERENCES	118

LIST OF TABLES

Table 1	Table of conditions and results for a series of Friedel-Crafts acylations to coat polyaniline nanofiber films with TCPP.....68
Table 2	Architecture and performance figures for select polyaniline nanofiber inverse DSSC types. The X indicates which components are present in each device type. The double line indicates the division between the front and back electrodes, each of which is prepared on an FTO slide.....108

LIST OF FIGURES

Figure 1	Energy level diagram of a p-n junction photovoltaic cell.....	3
Figure 2	Energy level and structural diagrams of a conventional DSSC (Grätzel cell).....	5
Figure 3	Diagram of the structure and operation of the polyaniline nanofiber inverse DSSC.....	11
Figure 4	Energy level diagrams of polyaniline nanofiber inverse DSSCs using either TiO ₂ as the ETM (left) or PCBM as the ETM (right).....	12
Figure 5	Synthesis of polyaniline and its redox and doping/dedoping chemistry.....	14
Figure 6	Bipolaron conduction mechanism in emeraldine salt polyaniline.....	15
Figure 7	Diagram showing the possible routes for charge conduction between crystalline regions and through the amorphous phase of polyaniline.....	16
Figure 8	5,10,15,20-tetrakis(4-carboxyphenyl)porphyrin (TCPP).....	20
Figure 9	Structure of PCBM ([6,6]-phenyl-C ₆₁ -butyric acid methyl ester).....	23
Figure 10	Measured IV curve of a typical silicon solar cell with key data points labeled.....	25
Figure 11	SEM images of polyaniline films electrochemically grown in an acidic environment, showing (a) the predominant nanospherical morphology, (b) lower coverage due to fewer CV cycles or lower oxidizing voltage, (c) overgrowth from a slower scan rate, (d) and (e) various other morphologies observed when using a faster scan rate.....	46

Figure 12	Cyclic voltammogram of the electropolymerization of aniline under basic conditions.....	48
Figure 13	SEMs of polyaniline nanofiber films before and after flash welding....	49
Figure 14	SEM of a polyaniline film prepared by heterogeneous nucleation on an FTO slide during a chemical polymerization of polyaniline nanofibers in the presence of phenol.....	50
Figure 15	SEMs of polyaniline films spin coated from solutions. (a) Bare FTO electrode, (b) PANi-CSA cast from <i>m</i> -cresol, (c) PANi-CSA cast from formic acid, and (d) PANi-DBSA cast from chloroform.....	51
Figure 16	SEMs of a polyaniline film prepared by cyclic voltammetry. Shown are (a) a nanofibrous region and (b) the particulate morphology.....	53
Figure 17	Photograph of a polyaniline-HCl nanofiber film and SEMs of the same at various magnifications showing the morphology and consistent high quality of the films.....	56
Figure 18	SEMs of polyaniline nanofiber films with (a) HCl, (b) CSA, or (c) MSA as the dopant acid used during polymerization, showing varying levels of nanofiber aggregation and porosity.....	57
Figure 19	Cross-sectional SEMs of a polyaniline nanofiber film deposited on a polyaniline blocking layer.....	59
Figure 20	Structure of emeraldine salt polyaniline dye-doped with TSPP.....	62
Figure 21	Reaction scheme for the attachment of TCPP dye to polyaniline nanofibers.....	64
Figure 22	UV-Vis spectrum of TCPP-coated polyaniline (large spectrum) and insets of TCPP (top left) and both doped and dedoped polyaniline (top right) for comparison. The TCPP-coated polyaniline spectrum shows a	

	combination of the TCPP and the dedoped emeraldine base polyaniline spectra.....	65
Figure 23	Plot of % coverage as a function of reaction time for the Friedel-Crafts acylation to attach TCPP dye to polyaniline nanofiber films.....	72
Figure 24	SEMs of a polyaniline nanofiber film before (left) and after (right) attachment of the TCPP dye by Friedel-Crafts acylation.....	73
Figure 25	SEMs comparing (a) bare polyaniline nanofibers, (b) TiO ₂ -coated HCl-doped polyaniline nanofibers, and (c) TiO ₂ -coated TCPP-coated HCl-doped polyaniline nanofibers.....	76
Figure 26	SEMs comparing a bare polyaniline nanofiber film to a TiO ₂ -coated polyaniline nanofiber film.....	78
Figure 27	SEMs of a polyaniline nanofiber film coated with TiO ₂ by the Tyzor LA method, showing the cracking of the film and exposed FTO resulting from a TiO ₂ coating that was too thick.....	79
Figure 28	SEMs of a film of Nanoxide HT TiO ₂ nanoparticles coating a polyaniline nanofiber film coated with TiO ₂ by the Tyzor LA method.....	81
Figure 29	SEMs of TiO ₂ -coated films of TCPP-coated polyaniline nanofibers before and after undergoing the hydrothermal treatment.....	84
Figure 30	Powder XRD spectra of TiO ₂ prepared by hydrolysis of Tyzor LA, before and after the hydrothermal treatment. All peaks, except those labeled as unidentified, are from anatase TiO ₂	86
Figure 31	SEMs of (a) bare polyaniline nanofiber films, or coated with PCBM from (b) 15 μ L, (c) 25 μ L, (d) 35 μ L, (e) 50 μ L or (f) 75 μ L of a 2 wt% solution of PCBM in chlorobenzene.....	89

Figure 32	SEMs of a (a) thermally evaporated aluminum electrode on top of Tyzor LA TiO ₂ and (b) sintered nanoparticulate TiO ₂ from doctor bladed Nanoxide HT on FTO electrodes.....	93
Figure 33	IV curve of a typical polyaniline nanofiber inverse DSSC with a thermally evaporated aluminum back electrode.....	94
Figure 34	IV curve of a typical polyaniline nanofiber inverse DSSC with a thermally evaporated silver back electrode.....	96
Figure 35	IV curve of a typical polyaniline nanofiber inverse DSSC with a thermally evaporated indium back electrode.....	97
Figure 36	IV curve of a typical polyaniline nanofiber inverse DSSC with a thermally evaporated indium back electrode and PCBM as the electron transport medium.....	98
Figure 37	IV curve of a typical polyaniline nanofiber inverse DSSC with a doctor bladed layer of nanoparticulate TiO ₂ on top of the TiO ₂ deposited from Tyzor LA and a thermally evaporated indium back electrode.....	99
Figure 38	IV curve showing current rectification from a polyaniline nanofiber inverse DSSC with a doctor bladed layer of nanoparticulate TiO ₂ on top of the TiO ₂ deposited from Tyzor LA and a thermally evaporated indium back electrode.....	101
Figure 39	IV curve of a simple standard DSSC made by pressing two FTO electrodes together, one with a polyaniline blocking layer and the other with a TCPP-coated sintered TiO ₂ nanoparticle coating.....	103
Figure 40	IV curves in the dark of standard construction DSSCs showing the effect of coadsorbents for passivating the interface.....	106
Figure 41	IV curve of a typical complete and functional polyaniline nanofiber inverse DSSC.....	107

Figure 42	Plot of a polyaniline nanofiber inverse DSSC's current output with time.....	112
Figure 43	Plot of V_{oc} and I_{sc} vs. light intensity for a complete polyaniline nanofiber inverse DSSC.....	113

LIST OF ABBREVIATIONS

η	Overall efficiency of a photovoltaic device
APS	Ammonium peroxydisulfate
BET	Brunauer, Emmitt, and Teller method for surface area determination
CB	Conduction band
CSA	Camphorsulfonic acid
CV	Cyclic voltammetry or cyclic voltammogram
DBSA	Dodecylbenzenesulfonic acid
DSSC	Dye-sensitized solar cell
ETM	Electron transport medium
EQCM	Electrochemical quartz crystal microbalance
FF	Fill factor
FTO	Fluorine-doped tin oxide coated glass
GPIB	General purpose interface bus
HOMO	Highest occupied molecular orbital
HTM	Hole transport medium
I_{imp}	Current at the point of maximum power output on an IV curve
I_{sc}	Short circuit current
IV curve	Current and voltage plot used for characterization of photovoltaic devices
LUMO	Lowest unoccupied molecular orbital
MSA	Methanesulfonic acid
PAni	Polyaniline
PCBM	[6,6]-phenyl- C_{60} -butyric acid methyl ester
P_{in}	Power input from incident light
P_{max}	Maximum measured power output
$P_{\text{theor.}}$	Power output if the photovoltaic device behaved as an ideal power supply – product of the open circuit voltage and short circuit current
QCM	Quartz crystal microbalance
R_{p}	Parallel resistance
R_{s}	Series resistance
SEM	Scanning electron microscope or scanning electron micrograph
SMU	Source measure unit
TAPP	5,10,15,20-tetrakis(4-aminophenyl)porphyrin

TCCPP	5,10,15,20-tetrakis(4-chlorocarbonylphenyl)porphyrin
TCPP	5,10,15,20-tetrakis(4-carboxyphenyl)porphyrin
TSPP	5,10,15,20-tetrakis(4-sulfonatophenyl)porphyrin
VB	Valence band
V_{mp}	Voltage at the point of maximum power output on an IV curve
V_{oc}	Open circuit voltage
XRD	X-ray diffraction

CHAPTER 1. INTRODUCTION

1.1 Overview

One of the greatest challenges facing our world today is the need for new dominant energy sources which do not have the deleterious health, environmental, and political consequences of our current use of fossil fuels. The most promising energy source, capable of providing for all current and future needs, is the Sun. Solar energy is already the driving force behind the natural, living world. How appropriate that it would also supply the requisite energy for the anthropogenic world. The Sun is certainly capable of providing all the energy we could ever need, as its incident light reaching Earth is 10,000 times our current energy consumption. In fact, our current energy needs would be met by covering only 0.1% of the Earth's surface with 10% efficient solar cells.¹ If we could collect all the solar energy reaching Earth, it would take only an hour to satisfy our energy requirements for an entire year.²

The difficulty in using the Sun as a major energy source lies in efficiently and inexpensively harvesting the Sun's light and converting it into electricity or fuel. Most research has gone into converting the Sun's energy directly into electricity as this is a very practical medium with great flexibility of use. The conversion of sunlight directly into electricity by materials is called the photovoltaic effect. This was first discovered by Becquerel in 1839 when he was studying liquid electrolytes.³

Developments in this area proceeded very slowly until, in 1954, Chapin at Bell Labs reported the first silicon p-n junction solar cell with an efficiency of 6%.⁴ In the 56 years since then, much research has been done but photovoltaics have still not achieved widespread, large-scale use due to high cost. As of 2008, only 0.09% of the energy consumed in the United States came from solar energy.⁵

The most common photovoltaic cells are made from an interface of p-type and n-type silicon, shown in Figure 1. P-type silicon is doped with boron, or another element with three valence electrons, whereas n-type silicon is doped with phosphorous, or another element with five valence electrons. When these materials are brought together to form an interface, some of the electrons from the n-type material migrate to the p-type, and some of the holes migrate from the p-type to the n-type, forming the depletion region. When incident light is absorbed by the silicon, excited states form and are dissociated into electrons and holes. The depletion region gives rise to an electric field which results in directionality of flow of these electrons and holes within the device.

Using this device architecture, commercial silicon photovoltaic modules attain power conversion efficiencies of around 10-15%. However, the material and processing costs are still so high that, even with government subsidies, photovoltaics remain non-competitive with other energy sources.

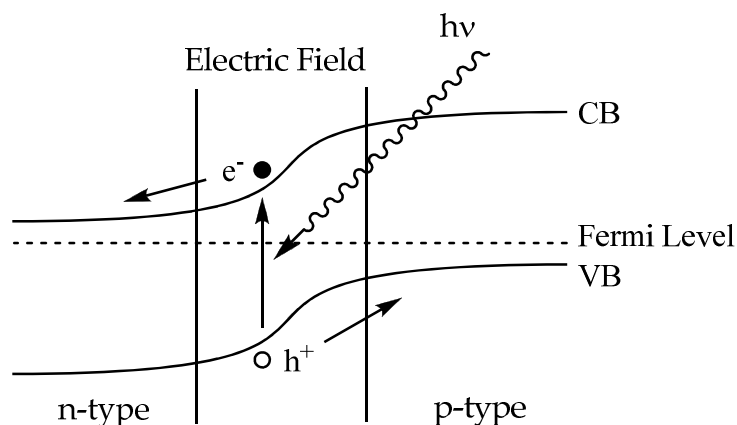


Figure 1. Energy level diagram of a p-n junction photovoltaic cell.

In recent years a number of alternative photovoltaic technologies have been discovered which offer hope of lower costs and therefore more widespread acceptance into everyday life. One of these technologies which has reached a level of efficiency similar to conventional silicon cells is dye-sensitized solar cells (DSSCs), which have exceeded 11% efficiency.⁶ With this level of efficiency reached, DSSCs can begin to compete, in terms of their price/performance ratio, with fossil fuels.⁷ The only factors still hindering their adoption as a commercially viable product are their longevity and tolerance of extreme conditions, both of which are related to their use of a liquid electrolyte.

1.2 History and Function of Dye-Sensitized Solar Cells (DSSCs)

Starting around the 1940s, a number of research groups began exploring photovoltaic devices made from dye-sensitized semiconductors.⁸⁻²⁷ They began by

using semiconductors such as ZnO and no reducing agent. From there, slow improvements were made such as incorporating a reducing agent or redox couple in the system and using ruthenium dyes. The field took off when, in 1991, O'Regan and Grätzel achieved a landmark 7.1% efficiency by introducing the idea of using nanoparticulate TiO₂ as a high surface area electrode onto which the dye was adsorbed.²⁸ The high surface area is essential as it allows for a large amount of dye to adsorb as a monolayer onto the TiO₂. This leads to the best balance of maximum light absorption and optimum electron injection from the dye into the TiO₂.¹⁴ The attained efficiency of over 11% is a significant achievement as it has been determined that DSSCs which are at least 10% efficient can begin to compete with the cost of electricity generated from fossil fuels.⁷

The promise of dye-sensitized solar cells (DSSCs) lies in their high efficiency, low energy and material costs, and the possibility of using less environmentally troublesome chemicals than mainstream technologies.^{7,29} There are also certain DSSC architectures which allow for roll-to-roll processing – a sort of “holy grail” of photovoltaic cell manufacture due to its flexibility, low cost, low complexity and high speed.

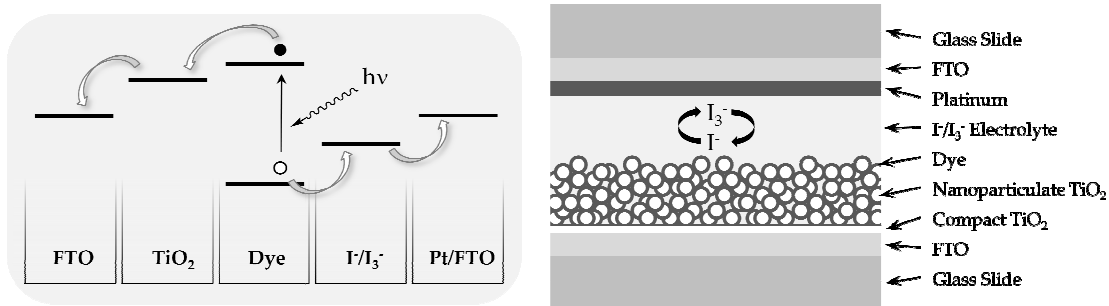


Figure 2. Energy level and structural diagrams of a conventional DSSC (Grätzel cell).

Conventional DSSCs (Figure 2) are typically constructed on FTO (fluorine-doped tin oxide coated glass) electrodes. A layer of compact TiO₂ is first deposited by hydrolysis of a titanium compound, often titanium isopropoxide. The next layer is formed by spreading a slurry containing nanoparticulate TiO₂ using the doctor blading technique. This is then dried and sintered at 450 °C resulting in a high surface area electrode for dye adsorption. In a conventional Grätzel cell, the dye used is a type of ruthenium bipyridyl complex, usually N3 or N719.⁶ It is adsorbed onto the TiO₂ surface from solution in EtOH. After drying, an electrolyte solution containing the I⁻/I₃⁻ redox couple is added to the device to fill the pores in the dye-coated TiO₂ film. The back electrode consists of a second piece of FTO coated with either platinum or graphite, either of which catalyzes the reduction of triiodide.

Upon illumination of the cell (Figure 2), light is absorbed by the dye, exciting an electron to its LUMO. This electron is injected into the conduction band of the TiO₂ and finds its way through the nanoparticulate TiO₂ layer to the front electrode where

it exits the cell and does work in an external circuit. The oxidized dye is reduced by the iodide, forming triiodide which migrates to the back electrode and there is reduced at the platinum or graphite by the electrons coming in from the external circuit.

Despite having high efficiency and great promise as a low-cost photovoltaic technology, conventional DSSCs also carry with them some drawbacks, most of which derive from the use of the liquid electrolyte system. The devices have a limited operable temperature range, due to diffusion limitations with cold temperatures, as well as the possibility of the solvent freezing or boiling. Due to the difficulties of forming complete and robust seals, there can also be slow loss of solvent through evaporation or leakage, as well as burst seals from hydrostatic pressure. The liquid electrolyte also brings with it the possibility of electrolyte degradation, dye desorption, and there are simply the technical difficulties of large scale manufacture.^{1,29-31}

This has led many researchers to explore possible remedies, including using ionic liquids^{1,32,33} or quasi-solid state gel electrolyte systems.^{1,29,34} Ionic liquids have the benefits of very low vapor pressure, wide temperature range for the liquid state, good chemical and thermal stability, high ionic conductivity, and they are nonflammable. Quasi-solid state gel electrolyte systems behave like solids mechanically and therefore could help prevent burst seals due to hydrostatic

pressure. However, since these systems both still use a liquid, they have not completely remedied the aforementioned problems.

The consummate solution lies in completely replacing the electrolyte solution with a solid state hole transport medium (HTM). Two main approaches have been taken to achieve this. One is using organic molecular p-type semiconductors and the other is using conductive polymers. The most widely used p-type semiconductor for this application is spiro-OMeTAD which has been used to achieve efficiencies of up to 4.44% under AM 1.5 conditions.³⁵ Many researchers have also experimented with various conductive polymers due to their low cost and ability to have their electrical properties easily manipulated.³⁶ Some of those used include; polythiophene derivatives,^{7,30,31,37-41} poly(*p*-phenylenevinylene) (PPV) derivatives,^{41,42} polypyrrole,⁴⁰ polyaniline (PAni),^{36,43-49} and various others.⁴² The highest efficiency achieved in a DSSC using a conductive polymer HTM was 2.9% under AM 1.5 simulated solar spectrum at 100 mW/cm² in a device using a polythiophene derivative.⁵⁰

Numerous researchers have noted that two of the main problems with using either organic p-type semiconductors or conductive polymers as the HTM are incomplete pore filling by the HTM in the nanoparticulate TiO₂ film and poor adhesion between the HTM and the dye coated TiO₂.^{29,36-38,51} A novel approach to address these issues, used in this project, is through an inverse architecture which has been termed an inverse DSSC.

1.3 Polyaniline Nanofiber Inverse DSSC

The inverse DSSC is simply constructed in the reverse order of a conventional DSSC. This means that the organic HTM is the first layer deposited and is the nanostructured material giving rise to the high surface area necessary for dye attachment. TiO_2 or another electron transport medium (ETM) is infiltrated into the dye-coated nanostructured HTM layer. This architecture allows different materials and processes to be used which can address the previously mentioned issues with solid state DSSCs.

The first inverse DSSC was constructed by Walter⁵² using electrochemically prepared nanofibrous poly-TAPP [poly-5,10,15,20-tetrakis(4-aminophenyl)porphyrin] as the HTM. This was grown on an FTO electrode using cyclic voltammetry in a solution of 0.15 mM TAPP and 0.01 M tetrabutylammonium perchlorate in 95:5 dichloromethane : pyridine. The CVs were run from -0.300 to +0.700 V vs. Ag/AgNO_3 in acetonitrile with a 30 second vertex delay at +0.700 V. These nanofibrous films were then coated with TCPP [5,10,15,20-tetrakis(4-carboxyphenyl)porphyrin] by soaking in a dichloromethane solution of TCCPP, the acid chloride derivative of TCPP, for 4-6 hours. Next, the TiO_2 was deposited into the pores of the nanofibrous film from a solution of Tyzor LA. Onto the TiO_2 was evaporated an aluminum contact to serve as the back electrode.

A significant hindrance to improved performance identified in Walter's design lies in the conductivity of poly-TAPP. While the conductivity has not yet been experimentally determined, it is expected to be low due to broken conjugation in the polymer backbone. The polymer is formed by linking together the phenylamines on the meso positions of the porphyrin rings. Due to steric hindrance, the phenyl groups are perpendicular to the plane of the porphyrin ring, and are therefore not conjugated with it. Barring the discovery of a method to coplanarize these phenyl groups, the polymer backbone does not have long stretches of conjugated monomers, but rather each porphyrin ring acts as an electronically isolated redox center, requiring a redox hopping conduction mechanism. Poly-TAPP also has the tendency to become less conductive as it grows electrochemically. A certain point can be reached during growth where the poly-TAPP is completely passivated and no further electropolymerization can take place. This loss of conductivity certainly affects the performance of devices made using this material. Poly-TAPP inverse DSSCs have achieved a V_{oc} of 600 mV, an I_{sc} of $10 \mu\text{A}/\text{cm}^2$, and a FF of 0.20.⁵²

Due to the questionable conductivity of poly-TAPP, it is necessary to either find a way to improve its conductivity or switch to using a different material. In this project, polyaniline (PAni) replaced the poly-TAPP as it is known for its high conductivity and does not have the same passivation effect. In addition, the poly-TAPP inverse DSSC does not incorporate a blocking layer to prevent TiO_2 from

contacting the FTO front electrode, thus creating a possible short circuit pathway. The preparation of polyaniline nanofiber films is also much easier and more conducive to large scale production than poly-TAPP nanofiber synthesis.

A polyaniline nanofiber inverse DSSC, shown in Figure 3, is assembled on a slide of conductive FTO-coated glass. The first layer consists of a polyaniline blocking layer. On this is deposited a polyaniline nanofiber layer, which is coated with TCPD dye. The pores are filled with either TiO_2 or PCBM, and either a metal electrode is evaporated on top or an FTO electrode is pressed on. Each of these components will be explained in further detail in the following sections.

As shown in Figure 3, the device functions by the dye absorbing photons, which excite electrons to the dye's LUMO. These excitons are dissociated at the dye/ETM interface by electron injection into the ETM. The electrons then travel to the back electrode, and out of the cell. The oxidized dye is reduced by the polyaniline nanofibers, which then pull electrons in from the external circuit through the FTO electrode.

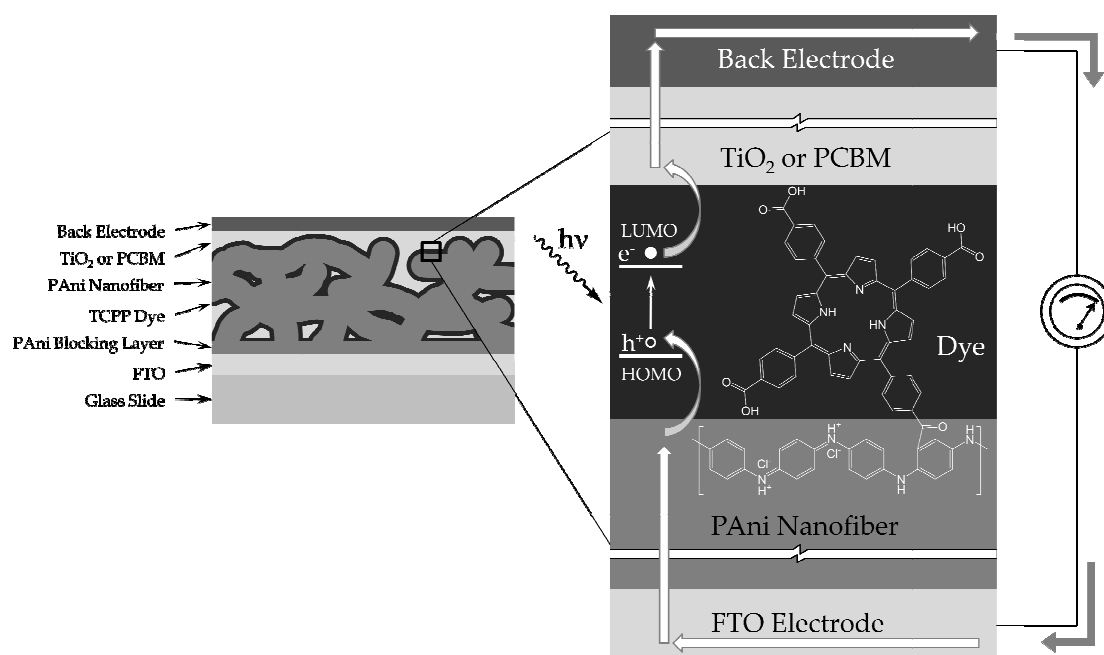


Figure 3. Diagram of the structure and operation of the polyaniline nanofiber inverse DSSC.

The same processes of light absorption and electron flow can also be visualized in the energy level diagrams in Figure 4. In addition, this figure shows the origin of the directionality of the electron flow. Electrons transfer from one material to another based upon the energy levels of the two materials. The driving force is toward the material with the higher work function (lower on the diagram). The figure also notes the maximum theoretical V_{oc} , which is determined by the difference between the Fermi levels of the ETM and HTM, or roughly approximated by the conduction band or LUMO of the ETM and the HOMO of the HTM.

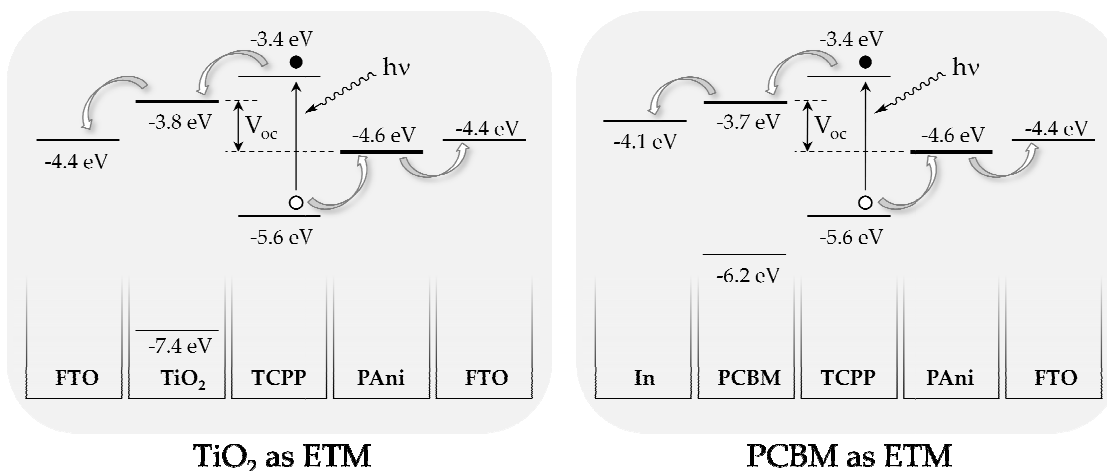


Figure 4. Energy level diagrams of polyaniline nanofiber inverse DSSCs using either TiO₂ as the ETM (left) or PCBM as the ETM (right).

1.4 Polyaniline Blocking Layer

The polyaniline blocking layer in the current inverse DSSC architecture is similar in function to the compact, nonporous TiO₂ layer which separates the FTO from the nanoparticulate TiO₂ in a conventional DSSC. In the case of the conventional DSSC, this layer serves to prevent short circuit of the cell by preventing the I⁻/I₃⁻ from contacting the front electrode. In the polyaniline nanofiber inverse DSSC the blocking layer prevents short circuit by blocking the ETM (TiO₂ or PCBM) from contacting the front electrode. The requirements for the blocking layer are twofold – it must be electrically conductive and physically insulating. To best fulfill these requirements the layer must be of a conductive material and be as thin as possible to prevent unnecessary resistive losses. The layer must also be nonporous and offer complete

surface coverage of the FTO electrode. In order to avoid complications in cell function due to the blocking layer, the same material that is used for the nanostructuring agent will also be used for the blocking layer, just as is done in the standard DSSC. This prevents any problems with adding another material with different energy levels which could either hinder charge transport or result in a decreased V_{oc} .

1.5 Polyaniline Nanofibers as the Hole Transport Medium and Nanostructure Agent

Polyaniline is the oldest known conductive polymer⁵³ and one of the most widely used. It was chosen as the HTM for this device due to its environmental stability, high conductivity, facile synthesis, simple acid/base doping/dedoping, and ease of preparing high quality nanostructures.⁵³⁻⁵⁶ In the polyaniline nanofiber inverse DSSC, the polyaniline nanofibers act as both the HTM and the high surface area agent. They function as the HTM through polyaniline's ability to efficiently conduct holes through its highest occupied molecular orbital (HOMO). Polyaniline nanofibers function as the high surface area agent due to their nanofibrous structure and the inherent high surface area ($54.6 \text{ m}^2/\text{g}$)⁵⁷ of that morphology. Having both high hole conductivity and high surface area in one material is what makes the inverse DSSC design possible.

Polyaniline is prepared by an oxidative polymerization process⁵⁸ in a strong acid (Figure 5). This results in the conductive emeraldine salt form which is half oxidized, meaning there is one quinoid moiety, which contains two nitrogens, for every three benzenoid moieties, which together contain another two nitrogens. From the emeraldine salt form it is simple to convert the polyaniline to its non-conductive forms, emeraldine base, pernigraniline and leucoemeraldine, as well as back to the conductive emeraldine salt form with simple redox and doping/dedoping reactions (Figure 5). The emeraldine base form is in the same oxidation state as emeraldine salt but is deprotonated. The pernigraniline form is fully oxidized with equal numbers of benzenoid and quinoid moieties, and the leucoemeraldine form is fully reduced with only benzenoid moieties.

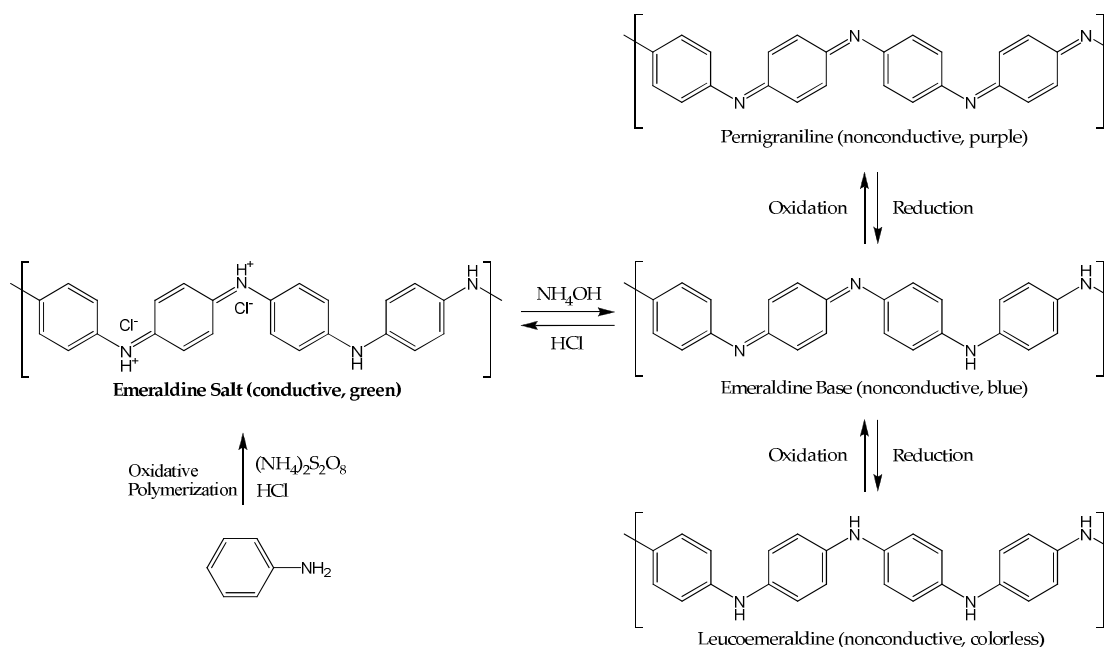


Figure 5. Synthesis of polyaniline and its redox and doping/dedoping chemistry.

Polyaniline needs to be in both the proper oxidation state and protonation state in order to be conductive (emeraldine salt form), because only when both conditions are met does the polyaniline have bipolarons present. Bipolarons are essential because within a polyaniline polymer chain, holes are conducted through a bipolaron conduction mechanism⁵⁹ (Figure 6). This is where charge transfer occurs from the lone pair on a nitrogen, adjacent to a quinoid moiety, to the nitrogen on the opposite side of the quinoid. Any defect in the chain, such as a bend or loss of the proper protonation or redox state, will hinder this conduction mechanism.

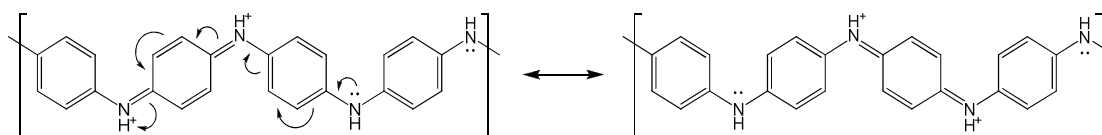


Figure 6. Bipolaron conduction mechanism in emeraldine salt polyaniline.

Conduction between polyaniline chains and within the material as a whole is not as well understood and there is still significant debate over it. What is well known is that polyaniline is partially crystalline, with anywhere from near 0% to over 50% crystallinity, depending on the synthetic route.⁶⁰⁻⁶⁵ It is also well known that these crystalline, or metallic, regions are dispersed within an amorphous phase made of poorly conducting, electronically isolated polymer chains. In addition, it is agreed

upon that the crystalline regions exhibit metallic conduction due to enough wavefunction overlap that the charges are delocalized within these regions.^{63,64,66,67}

The disagreement arises when discussing the conduction from one crystalline region to another, through the amorphous phase (Figure 7). There are many theories and variations on those theories, but they all seem to fall into two categories. The first is some type of variable range hopping mechanism either between metallic regions or between metallic regions and individual polymer chains in the amorphous region – the bottom and top routes in Figure 7, respectively.^{63,65,66,68-70} The second is a resonance quantum tunneling mechanism through localized states in the amorphous region – the top route in Figure 7, though it is a one step process, not two as the figure may be interpreted.^{64,67} On a slightly larger scale, between nanofibers or particles of polyaniline, there does not seem to be the same debate, but conduction is thought to follow a 3-D variable range hopping mechanism.⁶⁹

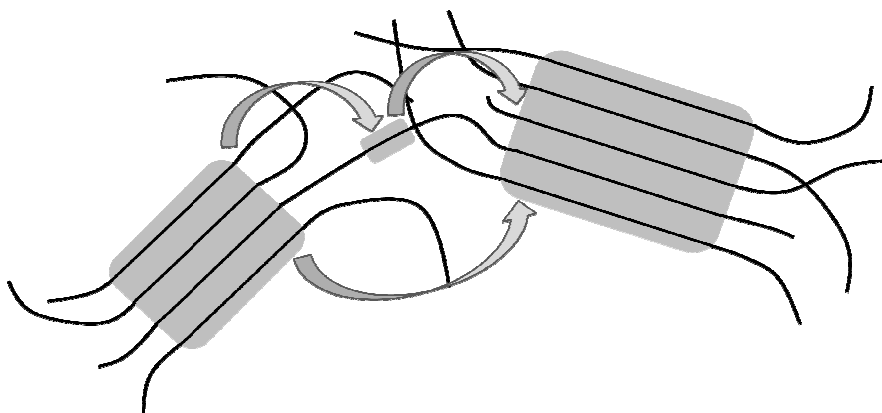


Figure 7. Diagram showing the possible routes for charge conduction between crystalline regions and through the amorphous phase of polyaniline.

When polyaniline is synthesized by the conventional method⁵⁴ it results in a particulate morphology. While useful as a bulk conductor in that form, polyaniline needs to have a high surface area for dye adsorption in order to be useful in an inverse DSSC. This is accomplished using a nanostructured form of polyaniline, such as the nanofibers easily formed by a process developed by Kaner et al.^{33,53,57,71-73} The simplicity and high quality results of this process rely on the nanofibrous morphology being intrinsic to polyaniline, so the synthetic conditions must simply be adjusted to bring out this inherent morphology. Why polyaniline naturally forms nanofibers is not completely understood, but it has been suggested that an anisotropic growth mechanism and formation of a depletion region around the forming nanofibers directs this elongated growth.⁷⁴ It has also been suggested that polyaniline's hydrophilic nature promotes the elongated form to enhance interaction between the polyaniline and the aqueous reaction medium. This concept is supported by an experiment showing that switching to a less polar reaction solvent results in a less fibrous morphology.⁷¹

Since polyaniline is insoluble in the aqueous reaction solvent, its precipitation and growth are governed by classic precipitation theory. Kaner's group found that the morphology of synthesized polyaniline was determined by the dominant nucleation mode. They observed that when heterogeneous nucleation dominated, it

gave rise to the particulate morphology and when homogeneous nucleation dominated, it gave rise to the nanofibrous morphology.⁵³

Kaner's process for synthesizing high quality polyaniline nanofibers relies on controlling three aspects of the reaction: rapid mixing of reagents, high reaction temperature, and no mechanical agitation (stirring or shaking).⁵³ The rapid mixing of reagents and the high reaction temperature both serve to increase the rate of polyaniline formation. This means that nuclei form and homogeneously precipitate as nanofibers before they have an opportunity to diffuse to an already formed nanofiber and precipitate as overgrowth on it. Avoiding mechanical agitation during the reaction also promotes homogeneous nucleation. The reason for this is twofold. Mechanical agitation moves embryonic nuclei to heterosites, therefore promoting heterogeneous nucleation. It can also dilute or destroy those embryonic nuclei, reducing the rate of homogeneous nucleation.⁷⁵ When these experimental factors are controlled, it allows for the desired nanostructure to be reliably created.

1.6 Porphyrins as the Sensitizing Dye

The sensitizing dye is the heart of the DSSC – it absorbs incident photons and uses those excitations to inject electrons into the conduction band of the TiO₂. It is then reduced by the HTM and absorbs more light to continue the process. Many dyes have been used over the years, some of the most notable being ruthenium

complexes,^{6,76} triarylamine derivatives,^{35,77,78} and porphyrins.⁷⁹⁻⁸³ Porphyrins are of particular interest because of their low cost, ease of synthesis and high molar absorptivity. They have been studied as sensitizing dyes in DSSCs since before Grätzel's groundbreaking 1991 paper⁸⁴ and continue to be of great interest. Recently, a new donor-acceptor zinc porphyrin was used to achieve an overall energy conversion efficiency of 11% in a conventional DSSC.⁸⁵

In this project, 5,10,15,20-tetrakis(4-carboxyphenyl)porphyrin (TCPP) was employed as the dye (Figure 8). Carboxylic acid groups are used on the dye due to their strong binding to TiO₂ which strengthens electronic coupling and therefore aids in charge transfer. They are also conducive to simple modification to acid chloride groups for use in a Friedel-Crafts acylation reaction – the method used to attach the dye to polyaniline nanofibers (see Section 2.4). TCPP is not a great performer in DSSCs due to its LUMO concentrating on the core of the molecule rather than out near the carboxylic acid groups, thereby weakening the coupling to TiO₂. However, it is used here for proof of concept because our lab has extensive experience with it and it is readily available. It could easily be switched at a later date for a better performing porphyrin dye. There is currently work in our lab aimed at synthesizing a porphyrin which absorbs at longer wavelengths to capture more of the Sun's light, and that has an excited state which couples to TiO₂ better than TCPP's.

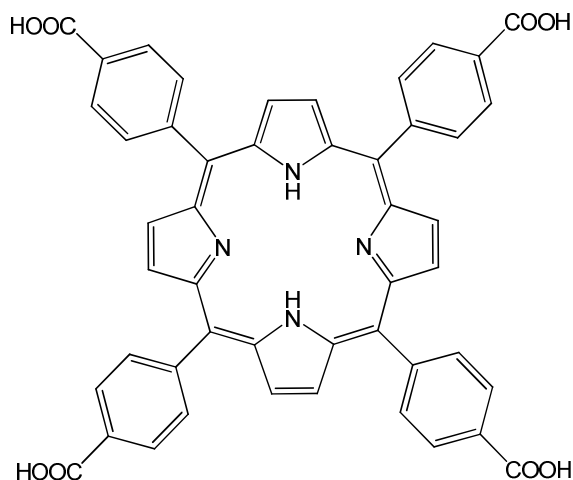


Figure 8. 5,10,15,20-tetrakis(4-carboxyphenyl)porphyrin (TCPP).

1.7 TiO₂ as the Electron Transport Medium

TiO₂ forms the interface with the dye where exciton dissociation occurs and subsequently acts as the electron transport medium (ETM) to move the photogenerated electrons through its conduction band to the back electrode so they can be transported out of the cell. TiO₂ is ideally suited to this application due to its favorably positioned energy levels (see Figure 4), its low cost, and its resistance to photocorrosion.

In a conventional DSSC the TiO₂ layer is formed from a paste of TiO₂ nanoparticles, often around 21 nm in diameter. The paste is spread onto the electrode by doctor blading, it is dried and then fired at 450 °C to burn out the organics and sinter the TiO₂. This method, of course, will not work with the inverse DSSC architecture due to the necessity of keeping the organics intact. The ~21 nm TiO₂

particles also would not penetrate the polyaniline nanofiber film and even if they could, packing roughly spherical particles onto roughly cylindrical nanofibers would result in a non-conformal coating, resulting in poor contact between the dye and TiO_2 .

The inverse DSSC design therefore needs a method of producing a conformal coating of TiO_2 that will penetrate the pores in the polyaniline nanofiber film completely and requires only mild conditions. A number of researchers have experimented with various types of liquid phase deposition methods which could possibly meet these requirements.⁸⁶⁻⁹³ Three of the more promising options include those developed by Li, a collaborator at Pacific Northwest National Labs, Deki and Imai.

Li's method is a controlled hydrolysis of Tyzor LA (an ammonium salt and lactic acid chelate of titanium) in a heated acidic aqueous solution to deposit a highly conformal layer of amorphous TiO_2 onto the substrate.^{94,95} Deki's procedure involves a controlled hydrolysis of ammonium hexafluorotitanate in an aqueous boric acid solution resulting in a partially anatase crystalline particulate film of TiO_2 .⁹⁶⁻⁹⁸ Imai's process, another controlled hydrolysis, uses either titanium oxysulfate or titanium tetrafluoride in aqueous acid in the presence of urea and results in a partially anatase crystalline layer of TiO_2 in an oriented needle-like morphology.⁹⁹⁻¹⁰¹

The enhanced conformal growth of the first method is its strong point, while the crystallinities of the latter two methods are theirs. Conformal growth is a necessity as the interface formed between the dye and TiO_2 is the only location where exciton dissociation can occur. Minimizing this contact area would dramatically reduce the performance of the photovoltaic device. Crystallinity, specifically the anatase polymorph, is also desirable due to enhanced electron injection kinetics, a higher electron diffusion coefficient, and higher overall efficiencies in DSSCs.^{89,102-104}

Weighing the benefits and shortcomings of the various possibilities, Li's method using Tyzor LA was chosen due to its superior conformal growth which is unhindered by complex morphologies. Also, this ideal conformal coating can be post-processed to convert the amorphous TiO_2 to anatase, resulting in both ideals. Most methods of converting amorphous TiO_2 to the anatase polymorph involve high heat, or other harsh conditions,^{88,90,91,105-112} which could damage the organic materials in the inverse DSSCs. However, there are some methods which claim to be able to convert amorphous TiO_2 to anatase under relatively mild conditions. The most promising was developed by Imai's group and involves heating the TiO_2 sample in an autoclave or bomb to 100 °C for 12 hours in the presence of water vapor.^{102,113,114} Imai explains that the Ti–O–Ti bonds undergo a series of hydrolysis and condensation reactions which break the strained bonds and replace them with more stable bonds during which the atoms slowly repack into the anatase crystal form.¹¹⁵

1.8 PCBM as the Electron Transport Medium

Instead of using TiO_2 as the ETM in an inverse DSSC, another promising material with correctly positioned energy levels for the task (see Figure 4) is PCBM (Figure 9). With PCBM's LUMO positioned at -3.7 eV and TCPP's at -3.4 eV, this provides the 0.3 eV difference necessary for exciton dissociation.^{116,117} PCBM is commonly used in bulk heterojunction solar cells due to its powerful electron acceptor characteristics and favorable photophysical properties.¹¹⁸⁻¹²¹ PCBM has a number of benefits over TiO_2 , such as not needing to be in a specific polymorph, therefore reducing the number of treatments required and also the production time and cost. Due to its simple solution processability, resulting from the solubilizing groups attached to the fullerene, using PCBM would allow for roll-to-roll processing of inverse DSSCs which can greatly improve the production economy. Employing PCBM in place of TiO_2 could also aid in creating flexible solar cells. Unfortunately, PCBM has the drawback of an electron mobility at least 10 times lower than TiO_2 .^{122,123}

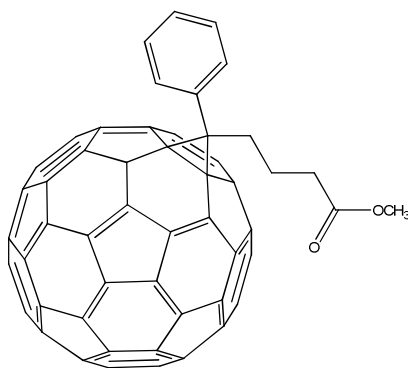


Figure 9. Structure of PCBM ([6,6]-phenyl- C_{61} -butyric acid methyl ester).

1.9 Photoactivity Characterization

There are a number of methods to determine the performance of solar cells and elucidate the inner workings of their operation. The most common method, which gives a wide variety of information about the solar cell, is using IV curves. These are measured both while the cell is exposed to light (simulated solar spectrum at 100 mW/cm², AM 1.5) and while in the dark. A linearly increasing potential is applied to the cell starting just below zero Volts to a little higher than the V_{oc} of the device and the resulting current is measured. From the resultant IV curve (Figure 10), a number of data are obtained. The most basic of these are the V_{oc} and I_{sc} which are the highest voltage and current, respectively, that the cell can produce. They are idealized values since the V_{oc} is measured at open circuit conditions and the I_{sc} is measured at short circuit conditions, meaning that the cell cannot actually operate at these values under load.

If the voltage and current values for each point along the IV curve are multiplied together, resulting in the power at that point, the maximum of these values obtained is P_{max} , or the maximum power point. This represents the maximum power that the cell is capable of producing. The voltage and current values for this data point are the V_{mp} and I_{mp} , respectively.

The fill factor, FF, is a measure of how close to ideal power supply behavior the device exhibits. Ideal power supply behavior would be the ability to deliver both

V_{oc} and I_{sc} at the same time. FF is calculated by comparing the maximum real power (from V_{mp} and I_{mp}) to the maximum theoretical power (from V_{oc} and I_{sc}) according the Equation 1. The values for FF range from zero to one, with one being ideal.

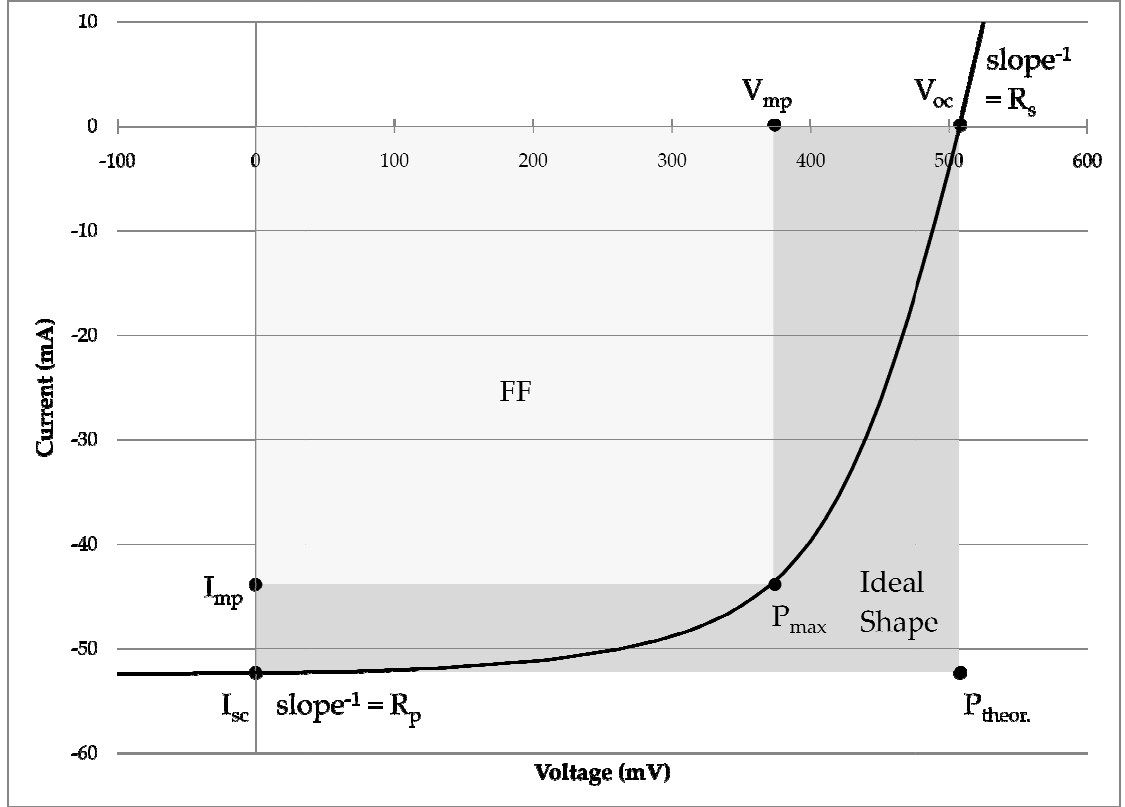


Figure 10. Measured IV curve of a typical silicon solar cell with key data points labeled.

$$FF = \frac{P_{max}}{P_{theor.}} = \frac{V_{mp} \times I_{mp}}{V_{oc} \times I_{sc}} \quad \text{Equation 1}$$

Overall power conversion efficiency, η , is one of the most closely watched values as it indicates the percentage of incoming light energy which can be converted into useable electrical energy. It is determined by comparing the power input, from incident light (P_{in}), to the maximum electrical power output, according to Equation 2.

$$\eta = \frac{V_{mp} \times I_{mp}}{P_{in}} \times 100 \quad \text{Equation 2}$$

There are also several internal resistance values which can be determined from the IV curve. The first of these is series resistance, R_s . This is a measure of the internal resistance of the device in series with the desired current flow. It is therefore an impediment to device efficiency, meaning that a lower R_s results in better cell performance. The series resistance is given by the inverse of the IV curve slope where it crosses the x-axis. The other resistance is the parallel resistance, R_p , which is associated with the shunt, or leakage, current within the device. This current represents back reactions, so a high R_p is desirable. R_p is determined by the inverse of the IV curve slope where it crosses the y-axis.

The dark current of a device is that resulting from an IV curve taken in the absence of light and it gives a measure of internal leakage current. It can also be used to indicate the presence of unwanted electrochemical reactions taking place in the device.

Together, all these data obtained from the IV curve give an understanding beyond simply how well the device performs. They also give information about what is taking place within the device and give direction for how the device can be improved.

CHAPTER 2. EXPERIMENTAL

2.1 Materials and Instruments

Aniline, *m*-cresol, camphorsulfonic acid (CSA), thionyl chloride, pyridine, and methanesulfonic acid were all obtained from Sigma-Alrich. Concentrated hydrochloric acid and sulfuric acid as well as 12-14 kD regenerated cellulose dialysis tubing were obtained from Fisher. Ammonium peroxydisulfate and chlorobenzene were obtained from Mallinckrodt. Nitrobenzene and chloroform were obtained from Acros. Phenyl C₆₁ Butyric Acid Methyl Ester (PCBM) was obtained from Solenne. Tyzor LA was obtained from DuPont. Nanoxide HT paste was obtained from Solaronix. P25 was obtained from Degussa. Triton X-100 was obtained from Dow Chemical Company. Concentrated ammonium hydroxide was obtained from J.T. Baker. Compressed nitrogen gas was obtained from Polar Cryogenics. Dodecylbenzenesulfonic acid (DBSA), 5,10,15,20-tetrakis(4-aminophenyl)porphyrin (TAPP), 5,10,15,20-tetrakis(4-sulfonatophenyl)porphyrin (TSPP), and 5,10,15,20-tetrakis(4-carboxyphenyl)porphyrin (TCPP) were obtained from TCI. Aluminum, silver, and indium evaporation slugs were 99.99% pure, 1/8 inch by 1/8 inch and obtained from Kurt J. Lesker Company. Triethylamine and formic acid were obtained from the PSU Chemistry Department stockroom. All were used as received except for the aniline and nitrobenzene which were vacuum distilled prior to use. The

nitrobenzene, triethylamine, and pyridine were stored over molecular sieves. The aniline and thionyl chloride were stored in a freezer. 5,10,15,20-tetrakis(4-chlorocarbonylphenyl)porphyrin (TCCPP) was prepared from TCPP by reaction with thionyl chloride.

Polyaniline nanofiber inverse DSSCs were made on electrodes prepared from Pilkington TEC 15 FTO glass. Sheets of FTO glass were scored and broken into 25 x 12 mm slides. The FTO slides were cleaned by sonication using a Branson 1510 sonicator with a solution of Sparkleen 1 in distilled water, followed by rinsing and then sonicating in distilled water. The cleaned slides were stored under distilled water in 15 mL polypropylene centrifuge tubes to prevent fouling.

Thin films of organic components (polyaniline, PCBM) were prepared by either drop casting or spin coating. Drop casting was done with a specific volume of a solution or colloid of the component in a Rainin pipette which was spread on a substrate placed on a level surface. The film was dried under a flow of dry nitrogen. Spin coating was done by spreading a small amount of solution across the entire surface of an FTO slide in a homemade spin coater and spun until dry.

Wet electrochemistry was done in a small glass vial with a Princeton Applied Research 263 potentiostat controlled through a GPIB by a computer running Win E-Chem. The working electrode was commonly the substance of interest on an FTO electrode, the counter electrode was platinum foil, and the reference was an Ag/AgCl

electrode. The platinum foil was cleaned before runs by heating to red hot in a flame. Scan parameters for cyclic voltammetry were commonly -0.2 to +0.8 V vs. Ag/AgCl at 50 mV/s.

Determination of mass and growth rate of thin films of electropolymerized polyaniline were made using a Princeton Applied Research model QCA922 electrochemical quartz crystal microbalance (EQCM). The same conditions were used as those in the wet electrochemistry experiments above.

Energy level determinations of polyaniline nanofibers were done following a procedure from Micaroni.¹²⁴ Cyclic voltammograms were recorded with the sample suspended in a 1 M solution of the same acid the polyaniline was doped with, using the same instrument and electrode setup as for wet electrochemistry above. The CVs were recorded at 50 mV/s from -0.2 to +0.8 V vs. Ag/AgCl.

Reactions done at elevated temperatures (polyaniline nanofiber synthesis and TiO₂ deposition) were usually done in polypropylene centrifuge tubes submerged in a homemade temperature regulated hot water bath. The hydrothermal treatment of TiO₂ was done in a modified Presto 409A pressure cooker containing 300 mL of distilled water in a 100 °C oven.

Conductivity measurements were done on pellets of polyaniline nanofibers, pressed to 70 MPa for 3 minutes and tested 48 hours later, as described by Zhang.¹²⁵ The four-probe Van der Pauw technique was used to measure the conductivity of the

pellets.¹²⁶ The pellets were pressed in a KBr pellet die with a hydraulic press and electrical contact was made to the pellets with copper wire point contacts in a homemade setup. A Keithley 236 SMU was used to supply a constant current and the resultant voltage was measured with a digital multimeter. For each type of pellet tested, four pellets were prepared and each was tested 4 times in different orientations for a total of 16 measurements per type of pellet.

UV-Vis spectra were recorded with a dual-beam Shimadzu UV-260 UV-Vis spectrophotometer using quartz cuvettes and usually either a 0.8 or 5 mm slit width. The 0.8 mm slit width was used with solution samples and the 5 mm slit width was used with TCPP-coated polyaniline nanofiber films to average out variations in film thickness. The spectrophotometer was controlled through a GPIB by a computer running Shimadzu's UV-265 software.

For scanning electron microscopy an FEI Sirion XL30 was used with an acceleration potential of usually either 2 or 5 kV and a spot size between 1 and 3. Samples were used without gold sputtering, as the samples were already conductive. For cross-sectional views, slides were scored with a tungsten carbide scribe and snapped to reveal the cross section.

Powder XRD was done with a Rigaku Smartlab 9 kW powder X-ray diffractometer in parallel beam geometry using graphite monochromated Cu K α radiation. Data were collected in 0.08° steps with a rate of 1.0°/min over the 10-90°

range. After background subtraction, the crystalline phase was qualitatively identified by comparing the experimental diffraction pattern against those of known phases using the Inorganic Crystal Structure Database.¹²⁷ Percent crystallinity was determined by comparing the integrated peak intensity from the crystalline phase to the integrated halo intensity from the amorphous phase. Crystallite size and strain were determined by an analog to the Williamson-Hall method.¹²⁸ TiO₂ samples were prepared for powder XRD by collecting the product of Tyzor LA hydrolysis, rinsing it repeatedly with distilled water, drying, and grinding to a fine powder. Some of the TiO₂ sample was tested as prepared and another portion was hydrothermally treated before testing.

Thermal evaporation of metal electrodes was done with a homemade evaporator using tungsten evaporating baskets and metal slugs. The vacuum level was around 3×10^{-5} mBar and the deposition rate around 20 Å/s. The electrodes were laid down in a pattern of four tracks per solar cell using a homemade machined steel mask. The track layout allowed for three separate measurements per cell.

Photoactivity characterization was done with a Keithley 236 SMU and a homemade stable light source consisting of a charger, car battery, 50 W quartz halogen lamp, neutral density filter and sample mounting setup. The light source was calibrated to an intensity of 1 Sun (AM 1.5, 100 mW/cm²) and adjusted with a slightly

colored filter to simulate the solar spectrum. The Keithley was controlled through a GPIB by a computer running LabView software.

2.2 Casting the Polyaniline Blocking Layer

Blocking layers were typically cast, using a homemade spin coater, from a filtered, saturated solution of conventionally prepared polyaniline^{125,129} doped with camphorsulfonic acid (PAni-CSA) in *m*-cresol. The solution was used to wet an FTO slide and the excess solution was removed with a pipette. Due to the low volatility of *m*-cresol, after 45 minutes of spinning, excess solution was dabbed off the sides and bottom of the FTO slide, followed by spinning for another 45 minutes until it was fully dry. Blocking layers were characterized by SEM.

A number of variations and other methods were also tested for making a blocking layer. Electropolymerization was attempted both as is typically done in 1 M acid and also at pH 9 to give a nonconductive film of emeraldine base polyaniline. Cyclic voltammetry scan rates ranged from 20 to 200 mV/s and the number of CV cycles ranged from 20 to 200. The potential window used was typically -0.2 to +0.8 V vs. Ag/AgCl with variations within that window as well as going as high as +1.145 V.

Attempts were also made to grow blocking layers by heterogeneous nucleation on an FTO electrode in a chemical polymerization reaction solution. Varying concentrations of phenol were used to give a more even film,¹³⁰ ranging from

7.9 μM to 63.2 μM . Apart from the addition of phenol, the reaction solutions were identical to those used in synthesizing polyaniline nanofibers, though the reactions were allowed to proceed for only 15 minutes.

Variations in forming blocking layers by casting from solvents included using drop casting in addition to the typical spin coating. Other solvents were also used, such as chloroform, dichloromethane, and formic acid. Polyaniline doped with DBSA (dodecylbenzenesulfonic acid) or in the undoped emeraldine base form were also used.

2.3 Synthesis and Deposition of Polyaniline Nanofibers

Colloids of polyaniline nanofibers were prepared by reaction of a solution of 0.146 mL aniline in 5 mL 1 M HCl and a solution of 0.091 g ammonium persulfate (APS) in 5 mL 1 M HCl. These solutions were mixed together, shaken for 15 seconds, and placed in a 60 °C water bath for 2 hours, undisturbed and with no stirring. The reaction solution consisted of aqueous 1 M HCl, 160 mM aniline and 40 mM APS. Hydrochloric acid was used over other possible acids because it gave the best fiber morphology and eliminated the need for several rinsing steps which could dedope the polyaniline. The resulting colloid was purified by dialyzing in 12-14 kD regenerated cellulose dialysis tubing against 5 mM HCl (or the same acid used to dope the polyaniline), as this gives a pH around 2.6 which stabilizes the colloid. Of

this colloid, 100 μ L were spread onto an FTO slide (already coated with the blocking layer, if used) such that the entire width (12 mm) and 16 mm of the length were covered. The remainder of the length was masked off with a piece of Scotch tape beforehand. The polyaniline nanofiber films were dried under a gentle stream of N_2 and characterized by SEM, cyclic voltammetry, UV-Vis and conductivity measurements.

A number of variations on the typical chemical synthesis procedure were also explored. Reaction times were varied from 1 to 24 hours and the reaction temperatures were varied between room temperature and 60 $^{\circ}$ C. Purification was also attempted by centrifugation and washing with distilled water. Lower concentrations of reagents, down to 8 mM aniline and 4 mM APS were used and the aniline/APS ratio was varied between 2 and 4. Several other dopant acids were used, including methanesulfonic acid and camphorsulfonic acid. For casting the films, lower and higher volumes of colloid were tested, as well as multilayered films. An attempt was also made to grow polyaniline nanofibers on FTO *in situ* during a typical chemical synthesis.

Electrochemical methods of polyaniline nanofiber synthesis were also explored. Films were prepared by cyclic voltammetry using 0.14 g or 0.23 g aniline in 5 mL 1 M aqueous sulfuric acid or camphorsulfonic acid. The potential window used was -0.2 to +0.8 V vs. Ag/AgCl with a platinum counter electrode. The scan rate was

varied from 20 to 50 mV/s and the number of cycles was varied from 10 to 100. In some experiments a 30 second vertex delay was employed, either at -0.2 or at +0.8 V. Additives were sometimes used, including aniline dimer (*N*-phenylbenzene-1,4-diamine) and lithium perchlorate. Some experiments did not use water as the solvent, but only aniline. Normal pulse voltammetry was also tested, with 0.15 M aniline in 5 mL of 1 M aqueous CSA. The experiment was run with a 0.1 s pulse duration, 1 s delay and 6 mV potential increments for 8 pulses and a -0.2 to +0.85 V vs. Ag/AgCl potential window. Characterization of the electropolymerized films was done with SEM, cyclic voltammetry, UV-Vis and EQCM.

2.4 Porphyrin Attachment to Polyaniline Nanofibers

TCCPP was prepared from TCPP by refluxing a solution of 100 mg TCPP and 10 mL thionyl chloride for 12 hours. The setup used was a simple reflux apparatus topped with a drying tube filled with Drierite. The excess thionyl chloride was then removed by vacuum distillation and the TCCPP was dried in a vacuum oven at 50 °C overnight or until the crystals turned from green to purple. The polyaniline nanofiber film, to which the TCCPP would be attached, was dedoped by soaking in 0.1 M ammonium hydroxide for 45 minutes followed by soaking in distilled water for 15 minutes and then drying under a nitrogen stream. The reaction solution was prepared from 3.75 mL saturated TCCPP in nitrobenzene, 250 μ L pyridine and 333 μ L

triethylamine. The dedoped polyaniline nanofiber film on FTO was submerged in this solution and allowed to react at room temperature overnight, usually 16 hours. The following morning the slide was rinsed by soaking in a series of two aliquots of 5 mL of a solution prepared from 110 mL chloroform and 7 mL triethylamine for 20 minutes followed by drying. The polyaniline nanofibers in the film were then redoped by soaking in 1 M HCl for 3 hours followed by drying under a stream of nitrogen.

Some variations to this method included using HCl or CSA as polyaniline's dopant acid and also using dedoped polyaniline. Instead of nitrobenzene, chloroform was also used as the reaction solvent. The reaction length was varied between a half hour and 24 hours. The temperature was varied between room temperature and 150 °C. Different concentrations of AlCl_3 or pyridine were used as the catalyst, as well as using no catalyst. The acid scavengers tested were pyridine, triethylamine or none, and in varying concentrations. The reaction was done in the light or dark and varying concentrations of TCCPP were used.

For devices which also had decanoic acid attached to the polyaniline nanofibers, this was accomplished by converting decanoic acid to decanoyl chloride by reaction of 1 g decanoic acid with 10 mL thionyl chloride at reflux for 8 hours, in the same setup as used for formation of TCCPP. The excess thionyl chloride was removed and the decanoyl chloride dried in the same manner as well. The decanoyl

chloride was attached to the polyaniline nanofibers just after the addition of TCCPP. The TCCPP reaction solution was poured off and replaced with a solution containing 3.75 mL nitrobenzene, 100 μ L decanoyl chloride, 250 μ L pyridine, and 800 μ L triethylamine. The reaction was allowed to proceed for 6 hours at room temperature after which it was rinsed in the same manner as done after a typical TCCPP addition. The higher concentration of triethylamine was used due to residual acid in the decanoyl chloride product.

Some alternate methods were also attempted for attaching the porphyrin dye to the polyaniline nanofibers. One of these was electropolymerization of TAPP onto the nanofibers using cyclic voltammetry in 1 M HCl and saturated TAPP. The scan window was from 0 to 1 V vs. Ag/AgCl. The scan rate was 50 mV/s and between one and 120 cycles were performed. A 30 second vertex delay at the most oxidizing potential was sometimes used.

Several other methods used are classified as “dye doping” which is a novel concept involving replacing polyaniline’s dopant acid with an acidic porphyrin dye. One such method used cyclic voltammetry of a solution of 1 mM TSPP (the sulfonic acid equivalent of TCPP) in 1 M HCl at a scan rate of 200 mV/s for 5 to 10 cycles from -0.2 to +0.8 V vs. Ag/AgCl. Chronoamperometry was also used for a solution of 1 mM TSPP in 1 M HCl with -0.2 V vs. Ag/AgCl applied for 5 seconds, followed by +0.7 V for 15 seconds. This was done on both doped and dedoped polyaniline nanofiber

films. An attempt was also made to chemically synthesize polyaniline nanofibers with TSPP as the acid dopant. A simple chemical dedoping/redoping process was also attempted. This is where the polyaniline nanofiber films were prepared normally with HCl as the dopant, followed by dedoping with 0.1 M NH_4OH . The films were then redoped using either TSPP or TCPP in ethanol or water at a concentration of either 0.3 mM or 1 mM. The doping time varied between 5 minutes and overnight. Characterization of porphyrin attachment on polyaniline nanofiber films was done with SEM for morphology, and UV-Vis for percent coverage determination.

For conventional architecture DSSCs, the dye attachment was carried out on a freshly sintered TiO_2 nanoparticle film on FTO. While still warm (around 120 °C) the slide was placed in 5 mL of a solution of 100 μM TCPP in ethanol. For those with decanoic acid also attached, this soaking solution also contained 5 mM decanoic acid. The slides were soaked overnight and air dried.

2.5 TiO_2 Deposition and Conversion to Anatase

TiO_2 deposition was performed on TCPP-coated polyaniline nanofiber films by hydrolysis of Tyzor LA in an acidic aqueous environment. Before coating, the slides were masked with Scotch tape such that the bare FTO was covered and the TCPP-coated polyaniline nanofiber film was exposed. The slides were oriented vertically to prevent homogeneously nucleated TiO_2 from settling out onto them. The

reactions were typically run at 50 °C in 15 mL polypropylene centrifuge tubes immersed vertically in a homemade temperature controlled water bath. The reaction solution was typically prepared from 5 mL 0.05 M aqueous Tyzor LA and 200 μ L 2.43 M HCl. The 0.05 M Tyzor LA stock solution was prepared from 24.52 mL commercial Tyzor LA solution (2.04 M) diluted to 1 L with distilled water. The stock 2.43 M HCl solution was prepared from 202.5 mL concentrated HCl and 797.5 mL distilled water. The reaction solutions used were on the order of pH 1.3-1.7, depending on the speed of reaction desired and the other reaction conditions (e.g., concentrations of Tyzor LA and acid, temperature). Due to the high level of pH sensitivity for this reaction, it was necessary to “calibrate” each batch of stock solutions by adjusting the temperature and/or acid concentration of the reaction to ensure that the time to cloudiness was between three and four minutes. This removed the need to measure the pH of every reaction solution and instead a standard amount of the stock reagent solutions could be measured into the reaction vessel by volume. The reactions were typically allowed to proceed for 1 hour after the onset of cloudiness, after which the slides were removed, rinsed with 5 mM HCl and dried.

Some alternatives to this procedure included varying the temperature from room temperature to 70 °C, varying the reaction time from the onset of cloudiness to overnight, varying the Tyzor LA concentration from 0.025 M to 0.150 M and preheating the Tyzor LA solution before adding acid or not preheating. Distilled

water and 1 M HCl were also used for rinses, but found to dedope the polyaniline and dissolve the deposited TiO₂, respectively.

Imai's method of hydrolyzing titanium oxysulfate in the presence of urea⁹⁹⁻¹⁰¹ was also tested. A solution of 0.01 M TiOSO₄ in water was prepared and to it was added urea to make a urea : titanium oxysulfate ratio ranging from 150 to 300 in increments of 50. Aliquots of 10 mL were adjusted to pH 1.5 with concentrated and 1 M HCl, the substrate was added, and the hydrolysis was allowed to proceed for a time ranging from 24 hours to 5 days at 60 °C.

The hydrothermal treatment to convert deposited amorphous TiO₂ to anatase was performed in a modified Presto 409A pressure cooker. To the pressure cooker were added 300 mL distilled water and the samples to be treated. The pressure cooker was sealed and placed in a 100 °C oven overnight.

For powder XRD analysis a large batch of 1 L of the stock Tyzor LA solution and 40 mL of the stock HCl solution were reacted at 70 °C. The TiO₂ was isolated by centrifugation, washed with distilled water and dried. Some yellow crystals which formed around the edge of the drying TiO₂ were discarded. A third of the TiO₂ product underwent the hydrothermal treatment, the rest was tested as prepared. Characterization was done by powder XRD.

For conventional architecture DSSCs, the nanoparticulate TiO₂ on FTO electrodes were prepared by doctor blading a layer of Solaronix Nanoxide HT paste

onto the FTO slide. The films were then sintered at 500 °C for 30 minutes and slowly cooled.

Some inverse DSSCs also had a layer of Solaronix Nanoxide HT paste doctor bladed on top of them in an attempt to help prevent short circuiting by the metal contact evaporation. After doctor blading, the film was rinsed with 5 mM HCl and dried.

2.6 PCBM Casting

PCBM films were cast on some TCPP-coated polyaniline nanofiber films as the ETM in place of TiO₂. These films were drop cast from 25 µL of a 2 wt% solution of PCBM in chlorobenzene and dried under nitrogen. The films were characterized by SEM. Some variations to the method included using a mask or not, and volumes of solution from 15 to 100 µL.

2.7 Back Electrode Preparation

Back electrodes were typically thermally evaporated from aluminum, silver, or indium slugs using a homemade thermal evaporator. The metals were typically deposited to 200 nm thick at a rate of 20 Å/s. The electrodes were laid down in a pattern of four tracks per solar cell. One track (2 x 9 mm) was deposited on the bare FTO of the front electrode. The other three tracks (2 x 12 mm) were deposited on the

TiO₂ or PCBM as the back electrode. This allowed for three measurements per cell. The layout of the electrode tracks was formed using a homemade machined steel mask. The electrodes were characterized by quartz crystal microbalance (QCM), SEM, and visually.

Other devices had back electrodes of nanoparticulate TiO₂ sintered on FTO pressed on top of them. The nanoparticulate TiO₂ used was Solaronix Nanoxide HT and it was doctor bladed onto the FTO slide. The electrodes were sintered at 500 °C for 30 minutes followed by slow cooling.

Some alternative methods tested were to use homemade indium-containing conductive epoxy, conductive grease, and copper tape as electrodes.

2.8 Photoactivity Characterization

Completed photovoltaic cells were characterized by recording IV curves in the light and dark. A typical run was from -0.1 to 0.8 V with data points recorded every 0.01 V. For each data point, 8 readings were averaged that came within a tolerance of 5% up to a maximum of 20 readings. V_{oc} , V_{mp} , I_{sc} , I_{mp} , P_{max} , R_s , R_p , FF, and η were calculated as described in Section 1.9.

For devices made with evaporated metal electrodes, contact was made to the electrodes with a homemade setup using thin copper wires in an arc shape in order to act as a spring and gently press onto the metal pads. For devices made with sintered

TiO₂ nanoparticles on FTO as the back electrodes, these were pressed on top of the front electrodes using a 1 kg weight. Pieces of copper tape were used to make contact between the FTO electrodes and the alligator clips on the potentiostat due to space limitations under the 1 kg weight.

Light intensity responsiveness was determined using a series of neutral density filters to adjust the light intensity to 0.33, 0.55, 1.00, and 1.70 standard Suns and recording IV curves at each point.

Aging with exposure to light was tested by exposing the solar cells to simulated solar spectrum at AM 1.5 continuously over the period of five hours, with 0 V applied, and every 15 minutes recording the average of five I_{sc} readings.

CHAPTER 3. RESULTS AND DISCUSSION

3.1 Polyaniline Blocking Layer

Polyaniline blocking layers were prepared by a number of methods and each was characterized in order to find the best option for the polyaniline nanofiber inverse DSSC application. The first method involved electropolymerization by cyclic voltammetry in either acidic or basic conditions. In the acidic conditions tested, polyaniline was found to adopt a nanospherical morphology (Figure 11-a) with the nanospheres on the order of 100-200 nm in diameter. This indicates a low affinity between the polyaniline and the FTO electrode as well as between the polyaniline and the electropolymerization solution. The polyaniline therefore adopts the spherical morphology which minimizes its interaction with both, and maximizes its interaction with itself.

A lower oxidation peak voltage and fewer CV cycles were found to result in decreased surface coverage (Figure 11-b). This is as expected due to a lower oxidative peak potential providing less driving force for the oxidative polymerization as well as less time at a voltage sufficient to cause polymerization. A slower scan rate was found to give more overgrowth, seen in Figure 11-c as protrusions on the nanospheres, making them appear similar to pollen grains. Due to the longer times at oxidizing potentials sufficient for polymerization, depletion regions could have

formed around the growing nanospheres and given rise to the anisotropic growth observed. It is also possible that the extended time at oxidizing potentials caused formation of embryonic nuclei in solution which collided with, and precipitated on, the nanospheres. A faster scan rate resulted in a wider variety of morphologies observed (Figure 11-d and e) due to arriving at highly oxidizing potentials quickly, thus causing a large amount of polyaniline to form in a short time and precipitate out of solution into a variety of morphologies. Due to their porosity and undesirable morphology, none of the films prepared by electropolymerization in acidic conditions were conducive to being used as a blocking layer.

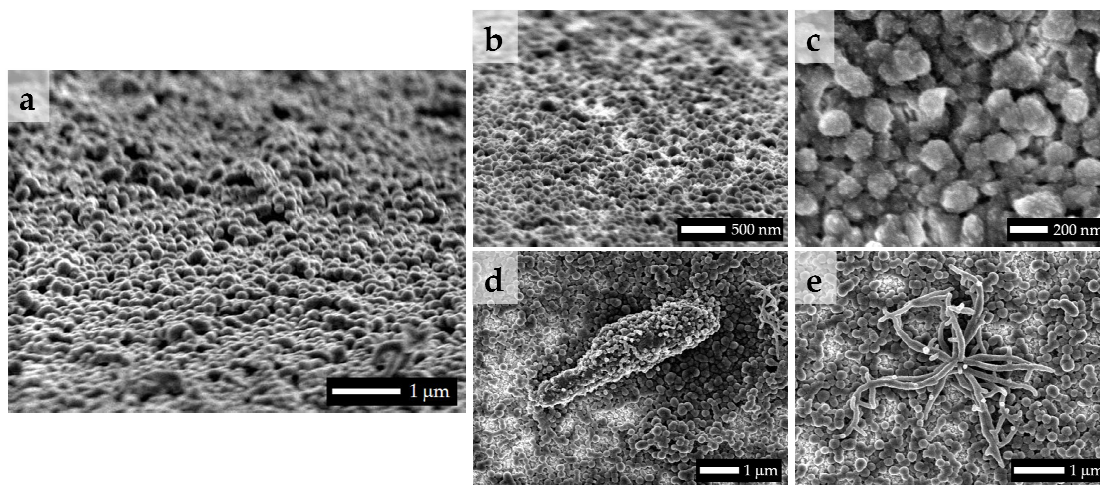


Figure 11. SEM images of polyaniline films electrochemically grown in an acidic environment, showing (a) the predominant nanospherical morphology, (b) lower coverage due to fewer CV cycles or lower oxidizing voltage, (c) overgrowth from a

slower scan rate, (d) and (e) various other morphologies observed when using a faster scan rate.

In addition to the typical acidic environment for electropolymerization of aniline, it has been demonstrated by Duić that aniline can also be electropolymerized in basic environments, up to pH 11.¹³¹ Using a basic pH can be beneficial for forming a blocking layer because the polyaniline deposited would be in its nonconductive emeraldine base form, causing further growth to deposit on the bare electrode rather than on already deposited polyaniline. To enhance the resistivity of the emeraldine base polyaniline toward further electropolymerization, sulfate was used as the counter ion, per Duić.¹³¹ As shown in Figure 12, there is an induction period at the beginning of the electropolymerization, but once this passes, the oxidation peak of aniline can be seen. As the electropolymerization continues, the oxidation peak fades away until the CV no longer shows any peaks. This indicates initial growth of the polyaniline followed by passivation of the electrode. Once the electrode is completely covered, the polyaniline could be doped with acid to its conductive form and used as the blocking layer. The films prepared in this manner unfortunately have very poor adhesion to the FTO substrate and peeled off easily, making them of little use as a blocking layer.

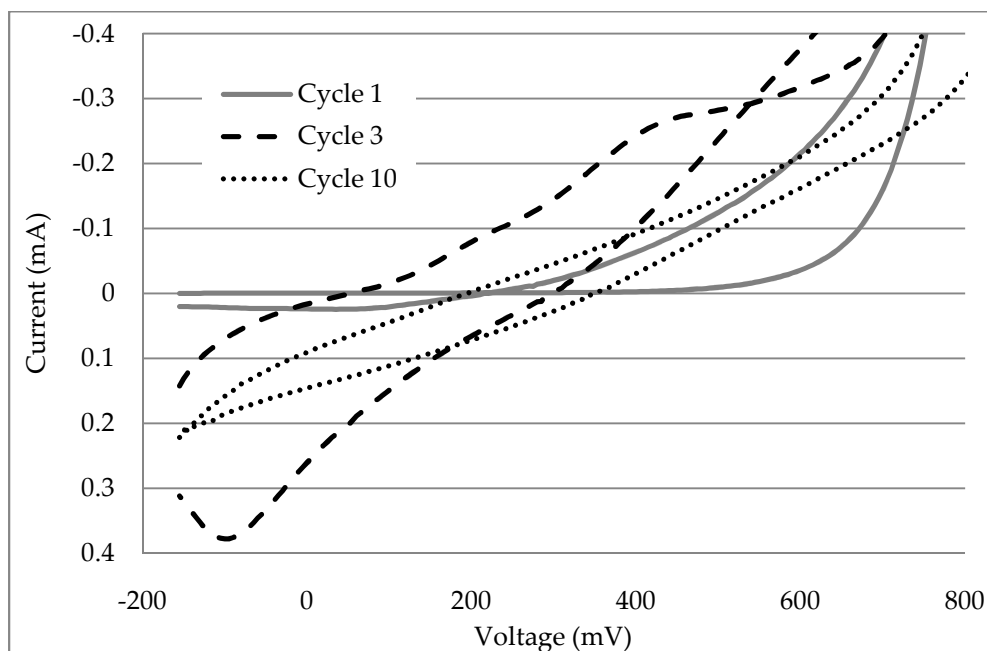


Figure 12. Cyclic voltammogram of the electropolymerization of aniline under basic conditions.

Another possibility for forming the blocking layer is by flash welding. Discovered by Huang and Kaner, this is a method in which a film of polyaniline nanofibers is cast onto a substrate and then exposed to a camera flash which melts and chemically crosslinks the polyaniline, resulting in a smoother film.^{132,133} Figure 13 shows that only a very thin portion on the exposed side of the film has an altered morphology, the rest of the film remains unchanged. Also, the portion of the film which is altered is still significantly porous and would therefore not function as a blocking layer. Additionally, this method would add undesirable electrical resistance

to the finished solar cell due to the film thickness required for flash welding to function.

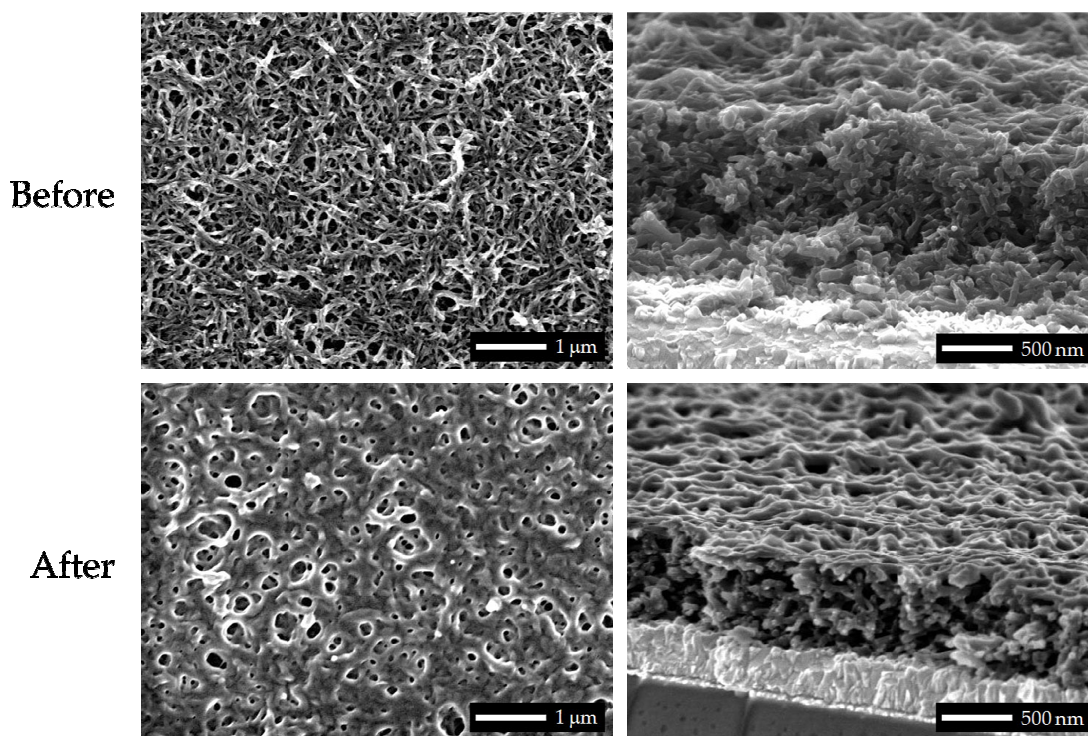


Figure 13. SEMs of polyaniline nanofiber films before and after flash welding.

During chemical polymerization of polyaniline nanofibers, reported in the next section, it was noticed that the reaction vessel is coated with a thin film of polyaniline. By submerging an FTO slide in the reaction solution, it was possible to grow, by heterogeneous nucleation, a film of polyaniline on the FTO. Adding phenol to the reaction solution, which was found to minimize the formation of a nanostructure,¹³⁰ resulted in the film shown in Figure 14. While this method offers

better coverage than all the previously mentioned methods, the films are still somewhat porous, and therefore undesirable.

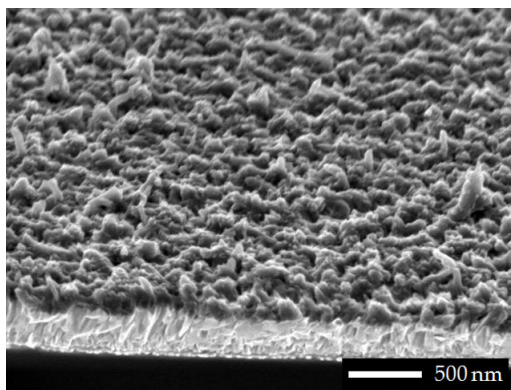


Figure 14. SEM of a polyaniline film prepared by heterogeneous nucleation on an FTO slide during a chemical polymerization of polyaniline nanofibers in the presence of phenol.

The most successful method attempted for preparing a polyaniline blocking layer was casting from a solution. This required matching the solvent and the counter ion used to dope the polyaniline, such that there was a high affinity between them. When this affinity is great enough, the solvent will deaggregate the doped polyaniline chains in order to maximize its interaction with them and therefore eliminate any nanostructure from the polyaniline. This is ideal as it allows for a continuous, thin film which fulfills the criteria necessary for the blocking layer. Camphorsulfonic acid (CSA) was found to promote dissolution the most out of all

dopant acids tested. Several solvents were also used, including *m*-cresol (Figure 15-b), formic acid (Figure 15-c), and chloroform (Figure 15-d). The polyaniline film in Figure 15-b is very thin and can be difficult to see, but its edge runs horizontally just below the middle of the image. Also, Figure 15-a is an SEM of bare FTO as a comparison to show that there is a film covering the jagged structure of FTO. Of these solvents, the only one which deaggregated the polyaniline chains sufficiently to remove the nanostructure was *m*-cresol.

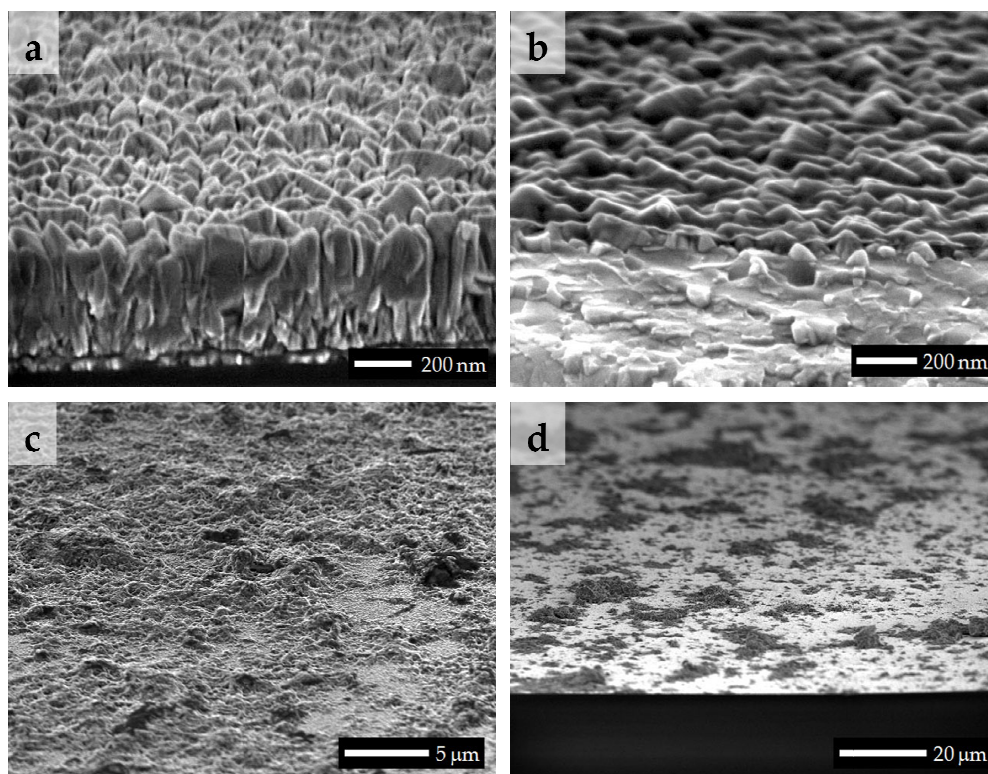


Figure 15. SEMs of polyaniline films spin coated from solutions. (a) bare FTO electrode, (b) PANi-CSA cast from *m*-cresol, (c) PANi-CSA cast from formic acid, and (d) PANi-DBSA cast from chloroform.

Both drop casting and spin coating were tested as the means to deposit the polyaniline from the *m*-cresol solution. Drop casting resulted in uneven films which did not coat out to the very edges of the FTO slide. Spin coating did not have these problems but provided even films which completely coated the surface of the slide. Therefore, spin coating from a solution of PAni-CSA in *m*-cresol was used to make all future blocking layers.

3.2 Polyaniline Nanofiber Layer

Polyaniline nanofibers were prepared by electrochemical and chemical means. The electrochemical methods included both cyclic voltammetry and normal pulse voltammetry with a variety of conditions. All electrochemical methods tested resulted in a mixture of nanofibrous (Figure 16-a) and particulate (Figure 16-b) morphologies. The nanofibrous portions were organized into highly porous, and therefore highly desirable, networks with individual fibers on the order of 100 nm diameter. However, it proved difficult to control the morphology and nanofibers accounted for only a small portion of the films formed under all conditions tested.

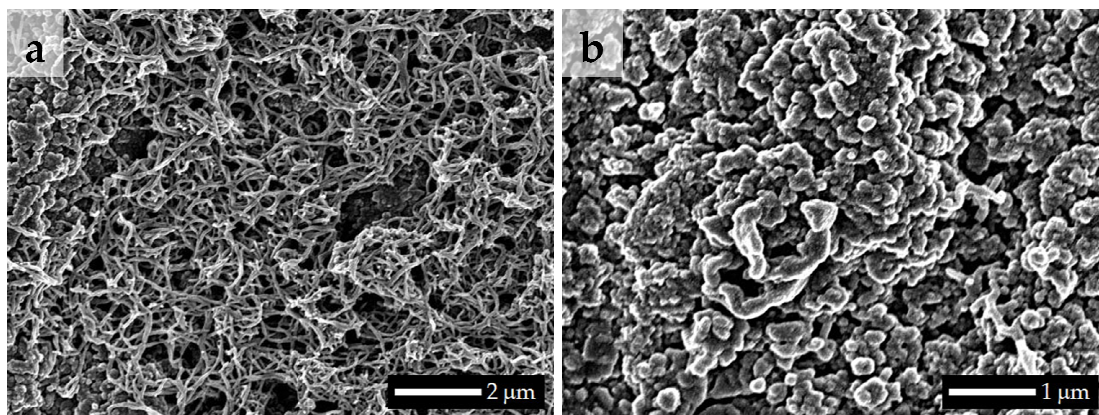


Figure 16. SEMs of a polyaniline film prepared by cyclic voltammetry. Shown are (a) a nanofibrous region and (b) the particulate morphology.

The chemical synthesis method gave very high quality, reproducible and porous nanofiber films with almost nonexistent contamination by nonfibrous particles. The polyaniline nanofibers were prepared by a chemical oxidative polymerization and purified by either suction filtration or dialysis. Suction filtration and washing was found to cause a higher level of aggregation between nanofibers, which resulted in less even and less porous films. Dialysis, because it does not force the nanofibers into a filter cake, was found to generate much less aggregation of nanofibers and gave more porous and even films.

The most critical part of reproducibly forming high quality films was in the process of depositing the film from the polyaniline nanofiber colloid which resulted from the chemical synthesis and purification by dialysis. It was found that drop casting the colloid gave much more control over film thickness than spin coating,

with no loss in film evenness. During drying, it was necessary to keep a slow nitrogen flow over the samples as any gas turbulence was found to translate into currents in the drying colloid, thus resulting in uneven films. It was also found that using Scotch tape masks to define the deposition area did not in any noticeable way affect the film quality, as it can with certain other solvent systems.

Film thickness was controlled by simply changing the volume of colloid applied to the substrate. Even films could be prepared from both large and small volumes, though the smaller volumes tended to have a higher consistency of film thickness. Films have been prepared anywhere from essentially a monolayer of nanofibers to several microns thick. The 700 nm thickness chosen for use in the inverse DSSCs was selected to simplify efficacy testing of the design. A thicker film would have allowed the dye to absorb more of the incident light and could therefore lead to higher efficiencies, but in absorbing more light it would remove the spectroscopic means of determining percent dye coverage (see Section 3.3). Using a thicker film would also increase the amount of back reaction and the internal series resistances. On the other hand, a significantly thinner film would not allow sufficient testing of the TiO₂ and PCBM infiltration methods.

Figure 17 shows a photograph of a polyaniline nanofiber film on an FTO slide along with SEMs at various magnifications to show the morphology and consistent quality of the film. The nanofibers are on the order of 50 nm in diameter and the films

have a wide range of pore sizes up to several hundred nanometers across. The porosity of these films allows for infiltration of the electron transport medium and gives rise to a high surface area, measured by the BET method to be $54.6 \text{ m}^2/\text{g}$,⁵⁷ making them well suited for dye attachment.

It is well documented that the nanofiber diameter, and therefore packing and overall film morphology, is directly dependent on the dopant acid used during polymerization. Based on results from several researchers showing possibly higher porosity nanofiber films,^{74,134} MSA (methanesulfonic acid) and CSA (camphorsulfonic acid) were used as dopant acids in addition to the typical HCl. The films prepared from CSA (Figure 18-b) showed lower porosity than HCl (Figure 18-a) due to higher aggregation of nanofibers. The films prepared from MSA (Figure 18-c) were even more aggregated and less porous. The aggregation is likely due to hydrogen bonding between the protonated polyaniline of one polymer chain and the oxygen atoms on the sulfonic acids of another polymer chain. Many other acids have been tested by various researchers which have been shown to give either less porous films or very large pores which result in lower surface area films. The polyaniline nanofiber films prepared with HCl as the dopant acid have the best balance of porosity and surface area and were therefore used in making the inverse DSSCs.

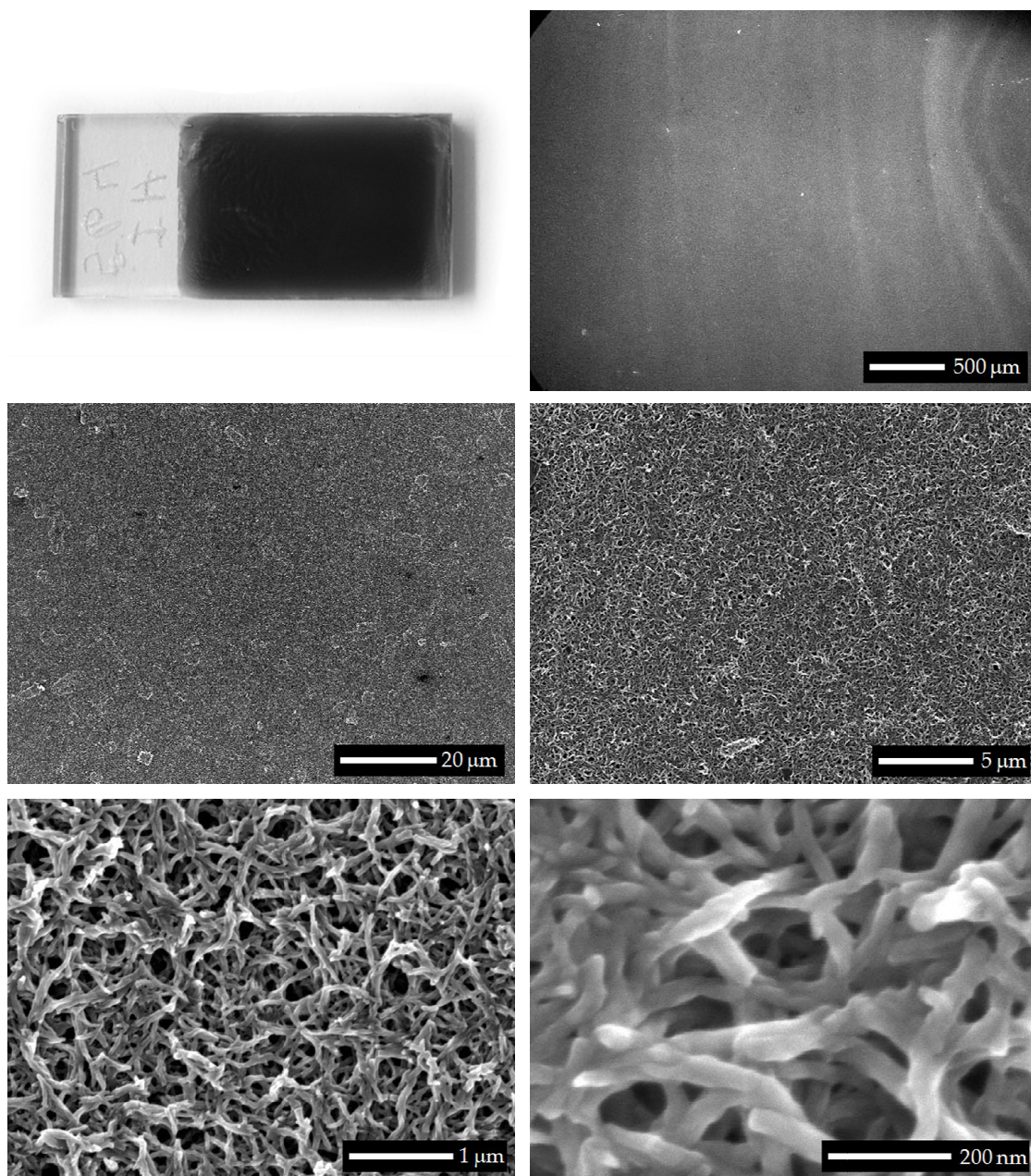


Figure 17. Photograph of a polyaniline-HCl nanofiber film and SEMs of the same at various magnifications showing the morphology and consistent high quality of the films.

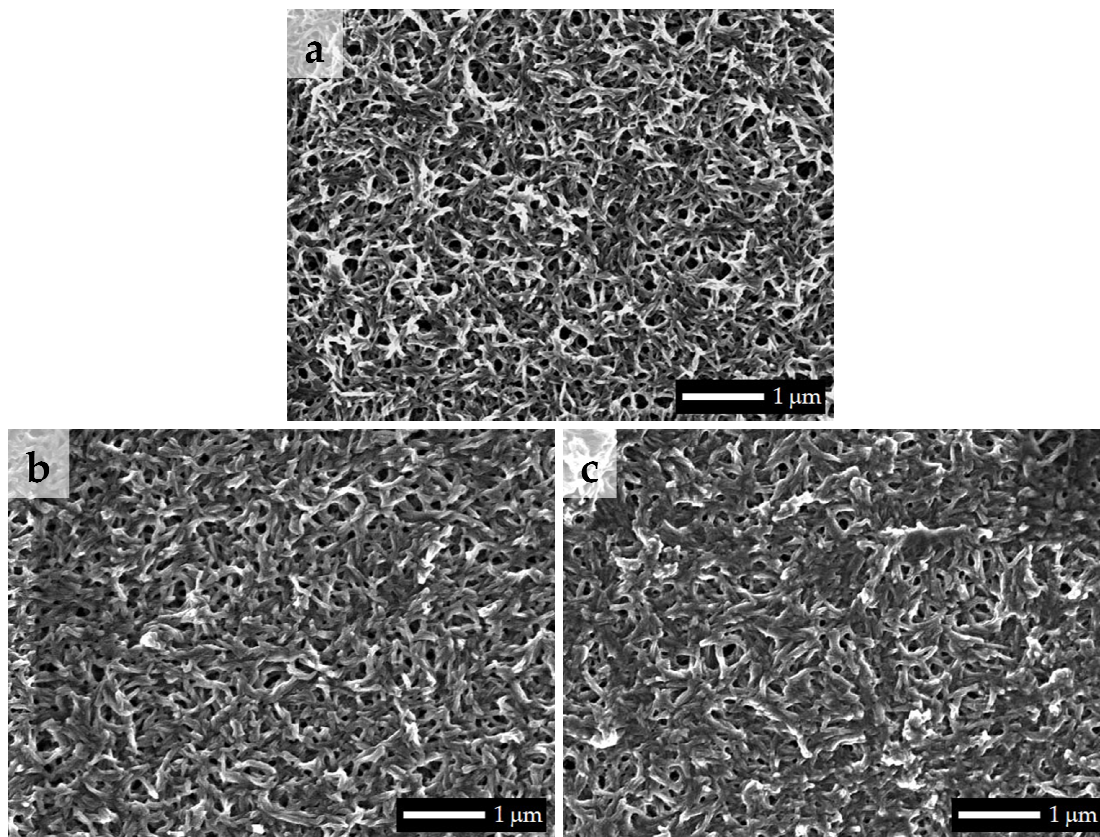


Figure 18. SEMs of polyaniline nanofiber films with (a) HCl, (b) CSA, or (c) MSA as the dopant acid used during polymerization, showing varying levels of nanofiber aggregation and porosity.

In another attempt to improve the porosity of PANi-HCl nanofiber films, varying concentrations of aniline and ammonium persulfate were used in the reaction solution. The idea being that a lower concentration could minimize the nanofiber aggregation. However, no visible difference was observed by SEM between the resulting films.

As a side note, it has been found that PANi-HCl nanofiber films appear to undergo an irreversible oxidative degradation after prolonged exposure to the atmosphere. The degradation can be observed in both reduced electroactivity, determined by cyclic voltammetry, and in the color of the films. The degradation is not observed when the films are stored under nitrogen, so this practice was adopted for all polyaniline nanofiber films and devices containing them.

In order for polyaniline nanofiber inverse DSSCs to function with their sandwich-cell construction, each layer must be compatible with the others and not interfere with the deposition of the other layers. The first meeting of layers in the device is between the polyaniline blocking layer and the polyaniline nanofibers. Figure 19 shows cross-sectional SEMs of a polyaniline nanofiber film deposited on a polyaniline blocking layer on an FTO slide. The nanofiber layer deposited on the blocking layer just as it would have on clean FTO, with identical morphology. There is good adhesion between the blocking layer and nanofibers, as they held together well through the process of snapping the slide in half for SEM viewing.

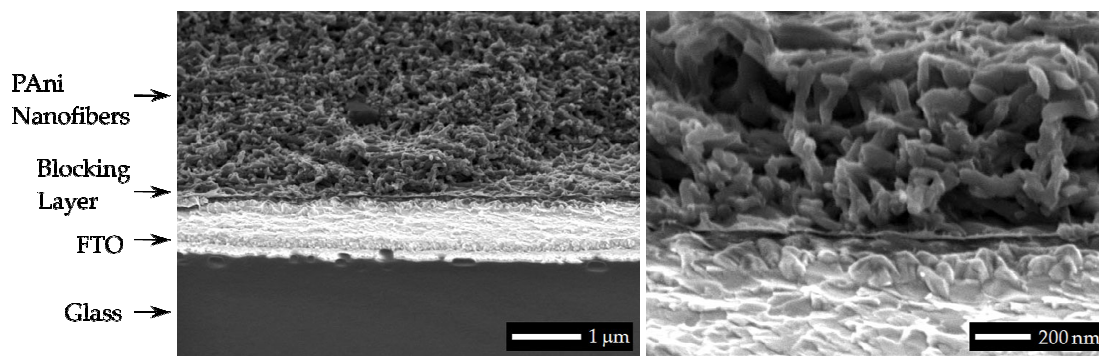


Figure 19. Cross-sectional SEMs of a polyaniline nanofiber film deposited on a polyaniline blocking layer.

In addition to having an appropriate morphology, the polyaniline nanofibers also have to have other physical properties within desirable limits, specifically their HOMO energy level and conductivity. Since polyaniline is a hole conductor, it transports charge via holes through its HOMO. In order to have proper directionality of charge flow within the device and maximize V_{oc} , the HOMO energy level of polyaniline must fall between the HOMO of TCPP and the conduction band of FTO (see Figure 4). The HOMO energy level of polyaniline nanofibers was determined using a method by Micaroni.¹²⁴ It involves measuring the oxidation onset potential for polyaniline using cyclic voltammetry against an Ag/AgCl reference electrode and converting that to a value with respect to the vacuum energy level. This is done using Equation 3, where E_{ion} is the ionization potential (HOMO energy level), E'_{ox} is the oxidation onset potential, and E_{vac} is the vacuum energy level defined as zero. This

method resulted in a HOMO energy level of -4.6 eV for polyaniline nanofibers doped with both HCl and CSA. This value is in very good agreement with the HOMO energy level found by other researchers for particulate polyaniline.¹³⁵ It is also positioned well with respect to the other materials in the polyaniline nanofiber inverse DSSC such that it will promote current directionality, give a high V_{oc} of around 0.8 V and give a substantial driving force for reduction of the oxidized dye.

$$E_{ion} \cong E'_{ox} + E_{vac} + 4.4 \quad \text{Equation 3}$$

Conductivity measurements were made of the polyaniline nanofibers to ensure that their conductivity was sufficient and that the processing steps later in construction of the devices would not destroy polyaniline's ability to transfer charge. The measurements were done on pressed pellets of polyaniline nanofibers using the van der Pauw technique.¹³⁶ The conductivity of pellets of as-prepared nanofibers was found to be 0.8 S/cm, which is in good agreement with results from other researchers.^{53,57,60,69,137-139} When the nanofibers were coated with TCPP by Friedel-Crafts acylation, the conductivity was found to decrease to 0.4 S/cm. It is likely that a significant portion of this reduction is caused by the method of preparing the TCPP-coated polyaniline nanofiber samples for this test. These nanofibers were coated with TCPP while suspended in a colloid, allowing the entire outside of the fibers to be

coated. This method was necessary due to the large amount of sample needed for making pressed pellets. It is expected that in the pressed pellet samples used for these conductivity measurements, the TCPP is acting as an insulator between nanofibers and preventing charge flow, thereby decreasing the conductivity. In an actual inverse DSSC, the TCPP is coated onto an already prepared film of polyaniline nanofibers, preventing the TCPP from forming an insulating barrier between fibers. However, whether the decrease in conductivity is real for the actual devices, or an artifact of the preparation method for conductivity measurement, the conductivity is still within the range of ideal for an organic solid-state HTM in a DSSC, as determined by Tan.³⁶

A sample of polyaniline nanofibers which underwent the hydrothermal treatment used in the preparation of the TiO₂ layer, was pressed into a pellet and found to have a conductivity of 6 S/cm, or 7.5 times that of as-prepared polyaniline. This is likely due to the heat causing a sintering type of process which enhances contact between nanofibers and/or causes a change of conformation of the polymer chains, or packing between them, within the nanofibers. Because of this result, the previously tested TCPP-coated polyaniline nanofiber pellets were subsequently hydrothermally treated and found to have their conductivity increase by 2.5 times to 1 S/cm, which is higher than as-prepared polyaniline nanofiber pellets (0.8 S/cm). Overall, the processes used in the manufacture of polyaniline nanofiber inverse DSSCs lead to a 25% increase in polyaniline's conductivity.

3.3 Porphyrin Attachment to Polyaniline Nanofibers

Since porphyrin dyes will not strongly adsorb onto polyaniline nanofiber surfaces like they can on TiO_2 , another method had to be employed. The first of these took advantage of the doping/dedoping chemistry of polyaniline. The idea being that since polyaniline needs to be doped (protonated) in order to be conductive, the normal dopant acid could be replaced with a strong acid form of a porphyrin dye. This was accomplished by a process of dedoping with ammonium hydroxide and redoping with the porphyrin acid. The porphyrin chosen for this application was TSPP (the sulfonic acid version of TCPP) due to its strong acid character. Figure 20 shows the structure of TSPP-doped polyaniline.

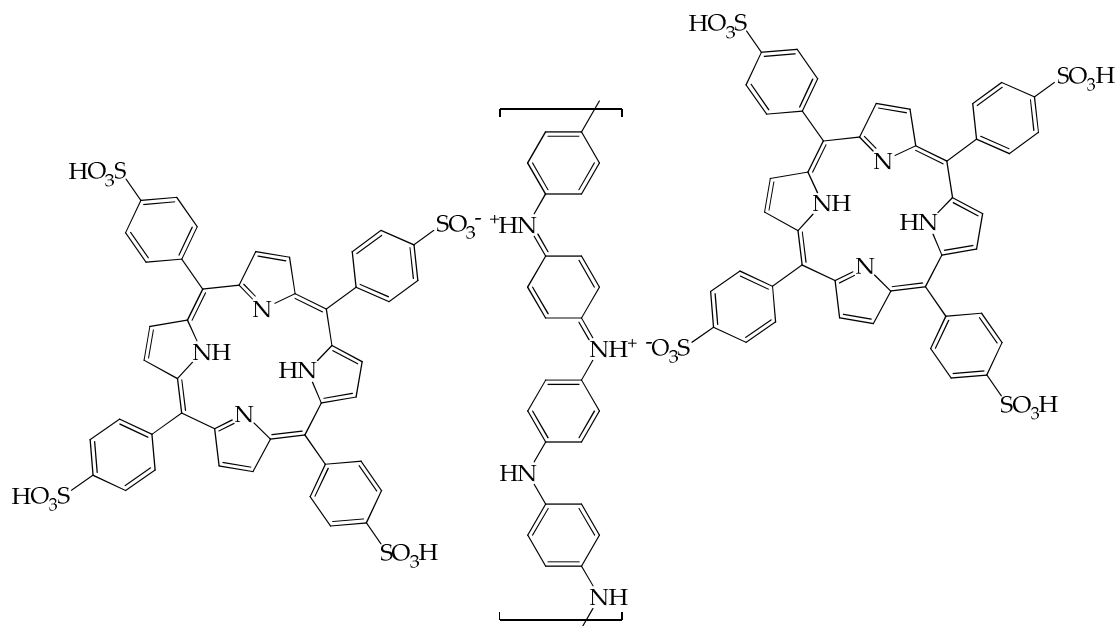


Figure 20. Structure of emeraldine salt polyaniline dye-doped with TSPP.

The dye-doping process was originally thought to degrade the polyaniline due to a loss of polyaniline's peaks in the UV-Vis spectrum. This was later realized to have been caused by using steel forceps to remove the slides from the dedoping and redoping solutions. The iron in the forceps reduced the polyaniline film to its leucoemeraldine form, leaving only the TSPP's contribution to the UV-Vis spectrum. After correcting the problem, this method resulted in very good coverage of the polyaniline nanofibers but the TSPP also penetrated into the fibers, as evidenced by the 170% coverage determined for one of the films. This method also presented the difficulty of avoiding loss of TSPP through dedoping or counter ion exchange during the subsequent processing steps.

Due to these difficulties, a method to covalently attach the porphyrin dye to the polyaniline nanofibers was sought and found in a Friedel-Crafts acylation process, shown in Figure 21. It begins by converting TCPP to TCCPP (the acid chloride form) by reaction with thionyl chloride. The TCCPP is subsequently attached to the polyaniline nanofiber film by reaction in nitrobenzene with a catalyst and base present.

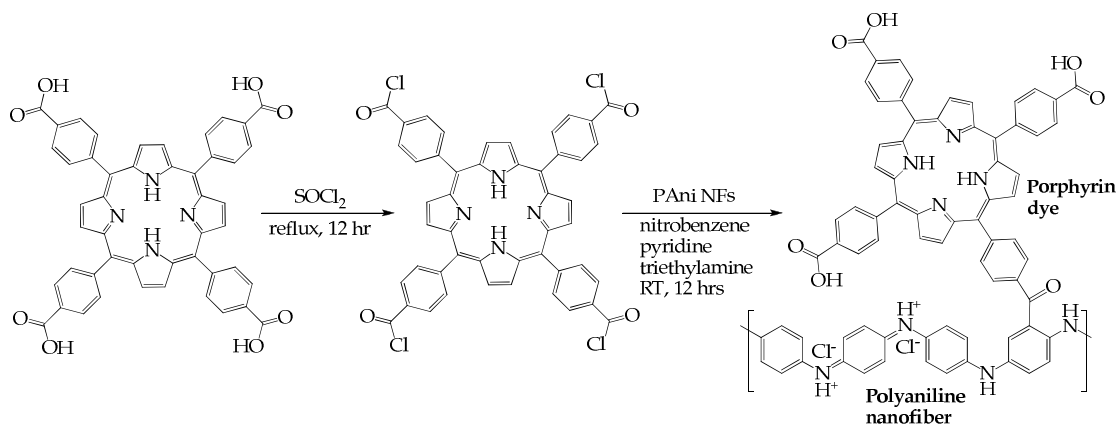


Figure 21. Reaction scheme for the attachment of TCPP dye to polyaniline nanofibers.

The attachment of TCPP onto the polyaniline nanofiber film is characterized by UV-Vis spectroscopy. Figure 22 shows a typical UV-Vis spectrum of a TCPP-coated polyaniline nanofiber film. The insert in the upper left shows the spectrum of only TCPP and the insert in the upper right shows the spectra of both the doped and dedoped forms of polyaniline. The spectrum used for the TCPP-coated polyaniline nanofiber film is a combination of the TCPP and the dedoped polyaniline as the doped polyaniline spectrum would interfere with the Soret band of the TCPP and hinder characterization of the film.

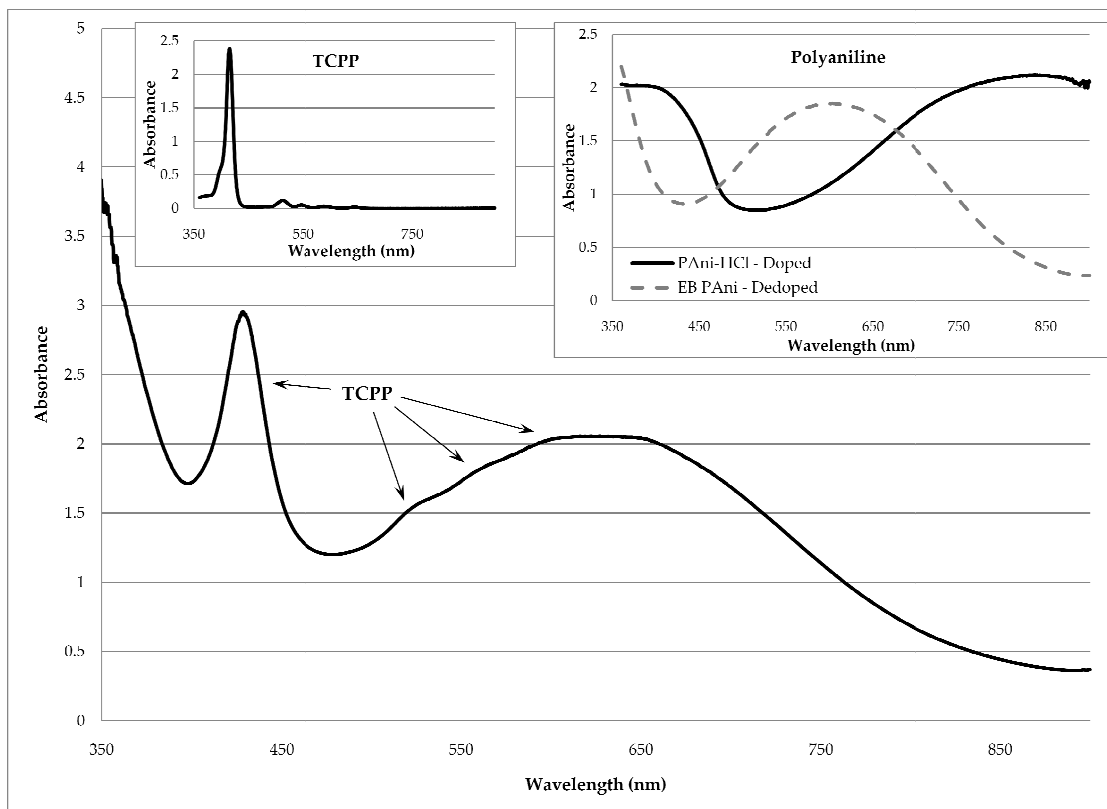


Figure 22. UV-Vis spectrum of TCP-coated polyaniline (large spectrum) and insets of TCP (top left) and both doped and dedoped polyaniline (top right) for comparison. The TCP-coated polyaniline spectrum shows a combination of the TCP and the dedoped emeraldine base polyaniline spectra.

Determination of the percent coverage of TCP on the coated polyaniline nanofiber films was done using UV-Vis spectra and Equation 4.

$$\% \text{ Coverage} = \frac{A_{\text{Soret}}}{A_{\text{max}}} \times 100 \quad \text{Equation 4}$$

Where A_{Soret} is the measured absorbance from TCPP, subtracting out the contribution from the polyaniline, at λ_{max} for the TCPP, and A_{max} is the theoretical maximum absorbance for TCPP in the film, given by Equation 5.

$$A_{max} = 6.784 \times 10^{-9} f_{nm} \Gamma A_{EB} \times 5.5 \times 10^{-5} cm \times 0.060 M \quad \text{Equation 5}$$

Where the portion $6.784 \times 10^{-9} f_{nm} \Gamma$ is derived from a method by Gilbert and Baggott for determining molar absorptivity using oscillator strength,¹⁴⁰ with f_{nm} being the oscillator strength, determined by Li¹⁴¹ to be 1.6 for TCPP, and Γ is the full width of the absorption band at half height. $A_{EB} \times 5.5 \times 10^{-5} cm$ is the path length portion of the equation, where A_{EB} is the absorbance at λ_{max} of the longer wavelength absorption (~650 nm) from the emeraldine base form of the polyaniline nanofiber film and $5.5 \times 10^{-5} cm$ is a conversion determined experimentally to relate polyaniline nanofiber film thickness to its absorbance. Lastly, 0.060 M is the theoretical maximum concentration of TCPP in the polyaniline nanofiber film calculated from the size of the TCPP molecule⁸⁰ and the surface area of a PAni-HCl nanofiber film.⁵⁷ Simplifying the combination of Equations c and d results in Equation 6 for calculating % coverage of TCPP dye on polyaniline nanofiber films.

$$\% \text{ Coverage} = \frac{A_{Soret}}{A_{EB}} \times 202 \quad \text{Equation 6}$$

Initial experimentation for the dye coating Friedel-Crafts acylation reaction indicated that the polyaniline must be in its dedoped (emeraldine base) form for the reaction to proceed, due to the positive charges on emeraldine salt deactivating the polyaniline toward electrophilic substitution. To prevent the polyaniline from being redoped by acid present in the solvents, or that generated during the acylation, a base was needed which is strong enough to deprotonate polyaniline yet nonreactive toward any of the other components in the acylation reaction mixture. The solvent must also not undergo a reaction with the acid chloride, by either not having the functionality necessary, or by being too deactivated. The catalyst must be capable of converting TCCPP into a better acylating agent than it is on its own, thereby reducing the activation energy. Knowing these requirements and having the results from some preliminary experiments allowed for determination of a starting point with materials and concentrations.

In order to optimize the reaction conditions, the effects of various changes to the system are recorded in Table 1. The solvent initially used for this reaction was chloroform, but as can be seen by comparing variations 0 and 1, chloroform results in very low coverage while nitrobenzene promotes the acylation reaction. This may be due to the polarity of nitrobenzene allowing it to better stabilize the charge on the reactive acyl ion therefore promoting its generation. It is also possible that the nitrobenzene, through one of its oxygen atoms carrying a negative charge, could act

similarly to pyridine by reacting with the acyl chloride, making it an even stronger acylating agent and thereby catalyzing the reaction.

Variation #	Solvent	TCCPP Conc.	Catalyst	Base	Rxn Temp	Sample Variation	TCCP Coverage
0	3.75 mL NB	sat.	0.745 M PYR	0.288 M TEA	RT	reference	84%
1	CHCl ₃	sat.	PYR	TEA	RT	rxn solvent	15%
2	NB	1/2 sat.	PYR	TEA	RT	1/2 TCCPP conc.	50%
3	NB	sat.	none	TEA	RT	no catalyst	74%
4	NB	sat.	AlCl ₃	TEA	RT	AlCl ₃ as catalyst	51%
5	NB	sat.	98.5 mM PYR	TEA	RT	less catalyst	82%
6	NB	sat.	1.49 M PYR	TEA	RT	more catalyst	91%
7	NB	sat.	PYR	0.146 M TEA	RT	less base	53%
8	NB	sat.	PYR	0.551 M TEA	RT	more base	106%
9	NB	sat.	PYR	TEA	100 °C	higher temp.	83%
10	NB	sat.	PYR	TEA	150 °C	higher temp.	destroyed

NB: nitrobenzene, PYR: pyridine, TEA: triethylamine, RT: room temp, sat.: saturated in rxn solvent

Table 1. Table of conditions and results for a series of Friedel-Crafts acylations to coat polyaniline nanofiber films with TCCP.

The concentration of TCCPP was found to affect the reaction yield just as one would expect. By comparing Variations 0 and 2, it can be seen that a higher concentration of TCCPP in the reaction solution significantly increases the reaction yield.

While no catalyst was found to be necessary to drive the reaction (Variation 3), addition of pyridine certainly improved the yield (Variation 0). Pyridine is a well known catalyst for the Friedel-Crafts acylation due to its formation of the acyl pyridinium ion which enhances the acyl group's reactivity for electrophilic substitution. Within the range tested, the concentration of the pyridine catalyst did not have a significant effect on the reaction yield, though there was a small enhancement in yield with the higher concentration of pyridine. Using AlCl_3 as the catalyst actually decreased the reaction yield as compared to having no catalyst present (compare Variations 3 and 4). It is likely that this is due to known reactions between AlCl_3 and basic aryl amines. The AlCl_3 could react with the amines in the polyaniline chain, thus deactivating the polyaniline toward acylation.

Pyridine was initially used as the base for scavenging acid but was quickly found to be too weak of a base to keep the polyaniline deprotonated, so triethylamine was used instead. A strong relationship was found between the amount of base used and the yield of the acylation reaction, with more base giving better yield (compare Variations 0, 7 and 8). Since the protonated form of polyaniline has positive charges

on the nitrogen atoms, the benzenoid and quinoid rings are deactivated toward electrophilic substitution. The polyaniline must therefore be deprotonated beforehand and the base in the reaction solution serves to capture all protons present in the solvents, as well as to capture all protons generated during the reaction. This keeps the polyaniline deprotonated, thereby helping drive the reaction.

The acylation reaction was found to proceed very well at room temperature. Increasing the temperature to 100 °C had essentially no effect on the reaction yield and heating the reaction to 150 °C destroyed the film.

Based on the above experiment, the reaction conditions employed for all future dye attachments were modified to use a triethylamine concentration of 0.551 M in order to maximize the yield. It was also discovered, after this experiment, that the TCCPP had not been given quite enough dissolution time to become fully saturated in the nitrobenzene reaction solvent. This was corrected for future experiments and led to a further increase in dye coverage, as will be seen shortly.

In order to ensure that the calculated percent coverages did not include any adsorbed dye, but only that which was covalently attached to the polyaniline nanofibers, a series of washes with various solvents was employed. The only treatment which removed more dye than the initial chloroform washing after the acylation reaction was 1 M HCl. This is convenient as an HCl soak is already used after dye attachment in order to make the polyaniline nanofibers conductive again. It

was found that a 3 hour soak in 1 M HCl would remove an additional 16% of the TCPP but no further TCPP could be removed after that. Therefore it is concluded that the remaining dye is covalently attached and this method of washing was employed for all subsequent experiments.

Using the improved reaction conditions determined for the Friedel-Crafts acylation, a series of ten identical samples was made in order to determine the reproducibility of the process. The samples were found to have an average coverage of 120% with a standard deviation of 9.6. Excluding the single outlier from this data series results in a standard deviation of 7.6. The greater than 100% coverage values obtained can be attributed to the assumptions made in determining percent coverage. These include assuming TCPP's absorption band follows a Lorentzian band profile and that the polyaniline nanofibers have an impenetrable surface. The main contributor is thought to be penetration of the nanofibers with dye, as a porphyrin's Soret band does closely resemble a Lorentzian band profile.

To better characterize the Friedel-Crafts acylation reaction, the percent coverage vs. time was measured. Figure 23 shows that the reaction proceeds quickly, with 80% coverage achieved in about 1 hour 20 minutes, and 100% coverage in four and a half hours. The films are typically allowed to react overnight, usually for 16 hours, which shows a coverage level of 120% in this graph, perfectly agreeing with the reproducibility experiment.

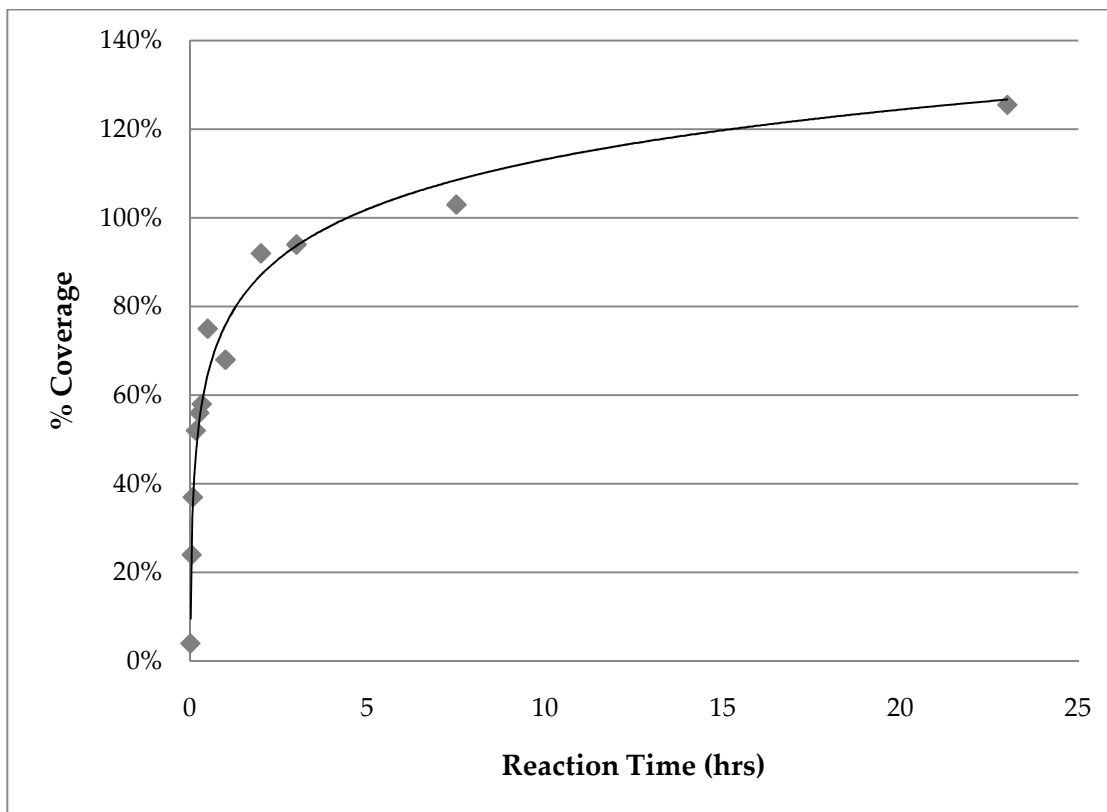


Figure 23. Plot of % coverage as a function of reaction time for the Friedel-Crafts acylation to attach TCPP dye to polyaniline nanofiber films.

The morphology of the polyaniline nanofiber films was compared before and after dye coating by the Friedel-Crafts acylation in order to verify that the structure was not destroyed or changed significantly. Figure 24 shows that after TCPP coating, the nanofibers appear as though they partially melted, resulting in slightly increased nanofiber diameters and an enlargement of pore size. Far from being destructive, this enlargement of the pores could actually be beneficial by enhancing the pore filling with TiO_2 or PCBM.

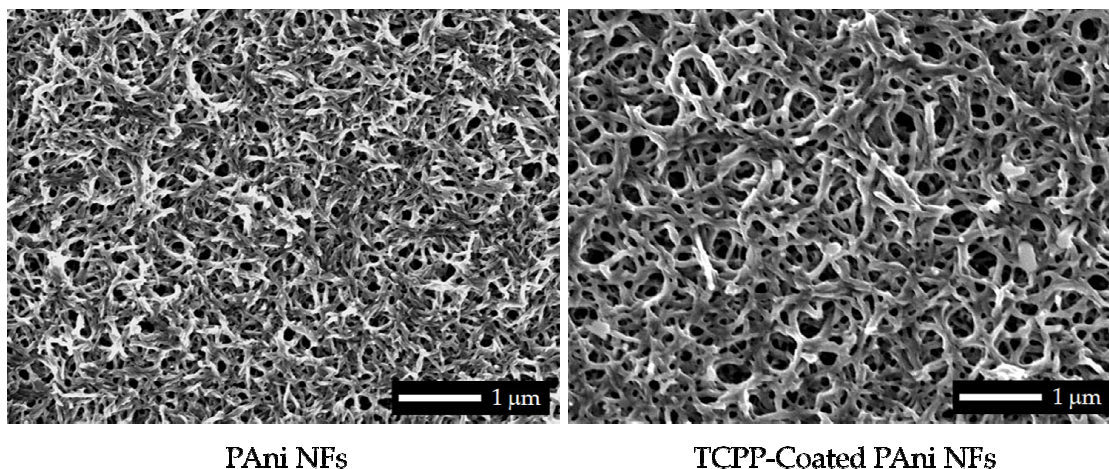


Figure 24. SEMs of a polyaniline nanofiber film before (left) and after (right) attachment of the TCPP dye by Friedel-Crafts acylation.

3.4 TiO₂ Deposition and Conversion to Anatase

Initially, both Li's^{94,95} and Imai's⁹⁹⁻¹⁰¹ methods were tested to determine which was more conducive to coating polyaniline nanofibers. Imai's method grew a film of TiO₂, on the order of a micron thick, made of packed needles oriented perpendicular to the substrate. The surface of the film was not clean, but covered with particles of varying morphologies. While the TiO₂ films appeared to be crystalline, an XRD signal was not able to be acquired, possibly indicating amorphousness. Initial attempts to coat polyaniline nanofiber films in this manner were unsuccessful. Since this method resulted in a specific nanostructured morphology, it would likely not be effective at coating a complex surface. Therefore, this method was passed over in favor of Li's, which results in highly conformal coatings.

Using Li's method of Tyzor LA hydrolysis, some initial TiO_2 depositions were done on blank FTO slides to find a good starting place and to develop the techniques for depositions onto polyaniline nanofibers. These initial experiments varied the time, temperature, and pH of the reactions. All of the reaction conditions tested resulted in a TiO_2 film deposited on the FTO substrate, though they varied by thickness and time needed to deposit the coating. The conditions decided upon for use in coating polyaniline nanofibers were chosen based on the time the reaction took and the thickness of the resultant TiO_2 coating. The two parameters were interrelated as a very short reaction time would result in homogeneous nucleation rather than the desired substrate coating by heterogeneous nucleation. Also, if the reaction time was too short, the reaction could go to completion before the substrate had been added. On the other hand, a very long reaction time is not only time-inefficient, but was also found to result in thinner films. A time of 3 to 4 minutes until the onset of cloudiness, followed by 1 additional hour reacting, was found to be ideal. From there, the same reaction conditions were used to coat films of polyaniline nanofibers with TiO_2 .

After the TiO_2 was deposited from Tyzor LA hydrolysis, a rinsing step was employed to clean the surface of the TiO_2 film. Initially 1 M HCl was used to ensure that the polyaniline in the device would remain doped. However, short circuiting during the metal electrode evaporation step and SEM investigation led to the discovery that the 1 M HCl completely dissolved the deposited TiO_2 off the substrate.

The remedy was found in switching to 5 mM HCl as that has a pH low enough to ensure the polyaniline remained doped but not so low that it dissolved the TiO₂.

The next logical step was to attempt a deposition of TiO₂ onto TCPP-coated polyaniline nanofibers. Included in this experiment were polyaniline nanofiber films doped with HCl, CSA, DBSA, or dedoped, and those coated with TCPP. The TiO₂ coatings were very similar on all films tested, indicating that the Tyzor LA process is not overly sensitive to the substrate. Figure 25 gives SEMs of some of the TiO₂ deposition results. Figure 25-a shows a bare polyaniline nanofiber film for comparison. Figure 25-b shows a TiO₂ coating on an HCl-doped polyaniline nanofiber film. Figure 25-c shows a TiO₂ coating on a TCPP-coated, HCl-doped polyaniline nanofiber film. The difference in the coating between Figure 25-b and c, specifically the layer of TiO₂ on top of the polyaniline nanofiber film, seems to have more to do with minute variations with the reaction conditions than it does with the Tyzor LA deposition's interaction with the specific substrate – similar reaction conditions do not always give, or avoid, the TiO₂ layer on top. The Tyzor LA method is highly sensitive to the reaction conditions, especially pH, so while the conditions are tightly controlled, there are sometimes slight variations between deposited films. Since this experiment was done, the depositions have become highly reproducible as the reaction's sensitivities are now well understood. Since the deposition results are

very similar for all tested dopant acids, HCl was chosen for the rest of the depositions as it is much easier to work with and cheaper than the others.

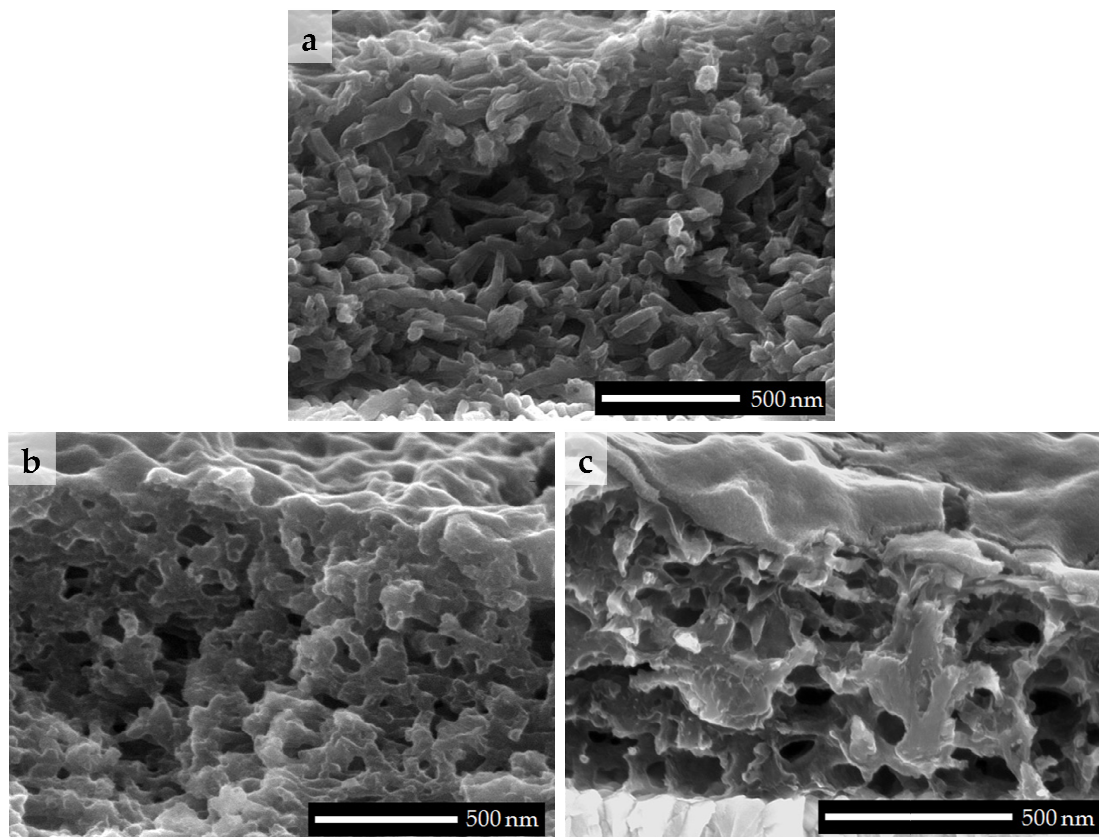


Figure 25. SEMs comparing (a) bare polyaniline nanofibers, (b) TiO₂-coated HCl-doped polyaniline nanofibers, and (c) TiO₂-coated TCP-coated HCl-doped polyaniline nanofibers.

Once the proper conditions were found for TiO₂ deposition, the pore filling could be more closely analyzed. Figure 26 shows before and after SEMs comparing a

bare polyaniline nanofiber film to a TiO₂-coated film of TCPP-coated, HCl-doped polyaniline nanofibers. These images clearly show how well Li's method, using Tyzor LA, coats complex morphologies. The polyaniline nanofibers appear to be completely coated with TiO₂ and the majority of the pore space has been filled as well. There are some holes in the filling, meaning there is room to improve in the future. However, additional performance from further pore filling is expected to be minimal. The nanofibers are completely coated, maximizing the surface area for charge separation, and the extent of pore filling is such that there are complete pathways for charge conduction within the device. An enhancement in pore filling would therefore only serve to modestly decrease the series resistance.

In order to determine if the pore filling could be improved by simple tweaking of the reaction conditions, an experiment was performed where the time of reaction and concentration of Tyzor LA were varied. The original concentration of 0.05 M Tyzor LA and reaction time of 1 hr were found to be ideal. When a lower concentration of Tyzor LA was used, the level of TiO₂ coating decreased dramatically to the point that at 0.025 M no TiO₂, visible by SEM, would deposit. At concentrations higher than 0.05 M, there was no visible difference in the amount of pore filling. The time to reaction completion was found to be about 1 hour, with shorter reaction times resulting in less pore filling and longer reaction times resulting in no noticeable increase in pore filling.

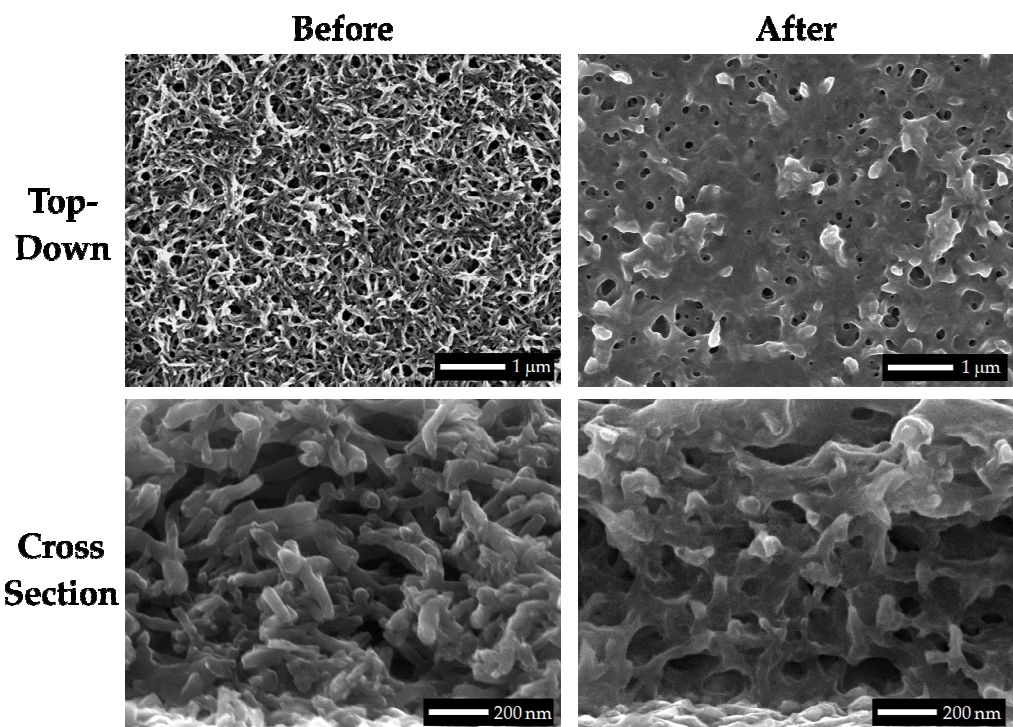


Figure 26. SEMs comparing a bare polyaniline nanofiber film to a TiO₂-coated polyaniline nanofiber film.

During the process of testing TiO₂ deposition by the Tyzor LA method, it was noticed that when the TiO₂ coating becomes too thick, large cracks form which split the polyaniline nanofiber film, exposing the underlying FTO electrode (Figure 27). This opens pathways for the devices to be short circuited during the metal electrode evaporation step. This is, however, not a problem for a sandwich type device where a solid electrode is pressed on top of this film. The cracking is caused by the shrinking of the TiO₂ film as it dries, building stresses great enough to pull the film apart, just as is seen in salt flats. It was found that to reliably keep cracks from forming in the

films, a very short reaction time was necessary. When the Tyzor LA reaction was allowed to proceed only until the reaction tube had just filled with cloudiness from the forming TiO_2 precipitate, crack formation was completely prevented. This does decrease the density of TiO_2 deposited in the pores, which will increase resistance to electron flow. However, it was found that two of these short depositions could be done, doubling the TiO_2 film thickness, if they were separated by a hydrothermal treatment. The hydrothermal treatment of the first coating reduces the stresses in the film and allows another layer to be deposited on top without any cracking in the film.

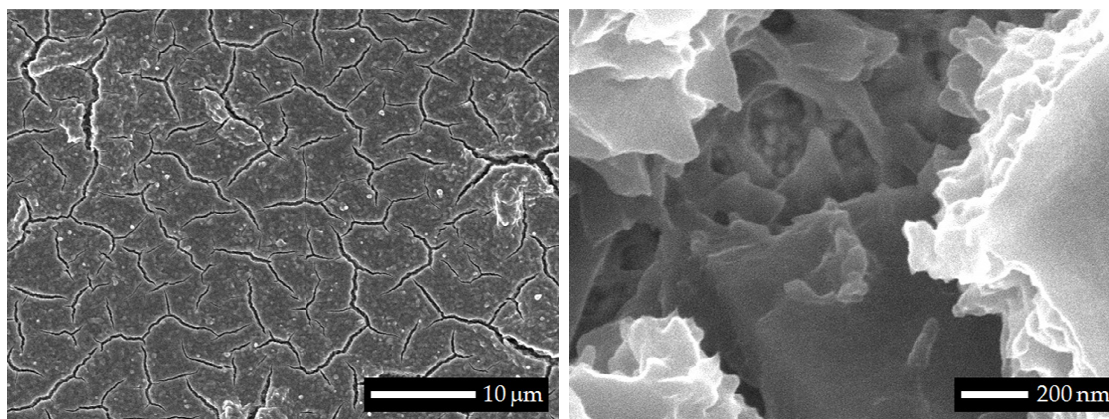


Figure 27. SEMs of a polyaniline nanofiber film coated with TiO_2 by the Tyzor LA method, showing the cracking of the film and exposed FTO resulting from a TiO_2 coating that was too thick.

Another approach to the issue of cracking was to use a layer of TiO_2 nanoparticles on top of the deposited Tyzor LA as a blocking layer to prevent evaporated metal from contacting the FTO electrode through the cracks. While TiO_2

nanoparticles clearly form a porous film, the making of these films has been well studied and films offering complete coverage can easily be made. Since metal evaporation is line-of-sight, the nanoparticle film should not need to be too thick to block all the metal vapor from penetrating into the film. Use of P25 either with or without Triton X-100 surfactant proved to not be capable of creating a reasonably thin film which evenly and completely covered the substrate. Interestingly, the TiO_2 nanoparticles from this method completely avoided filling the cracks in the TiO_2 -coated polyaniline nanofiber film.

It was found that films of Solaronix Nanoxide HT paste could easily be doctor bladed very thin and still completely cover the substrate (Figure 28). However, using this paste is not ideal due to the presence of a significant amount of surfactants and additives, as well as the lack of sintered connections between particles, all of which decrease the film's conductivity. Based on IV curve results, it was found that this method was successful in preventing short circuiting of the devices. However, the films were also found to create nonfunctional devices, likely due to photoelectron loss to recombination due to the low film conductivity and altered surface state energies resulting from the surfactants coating the nanoparticles.

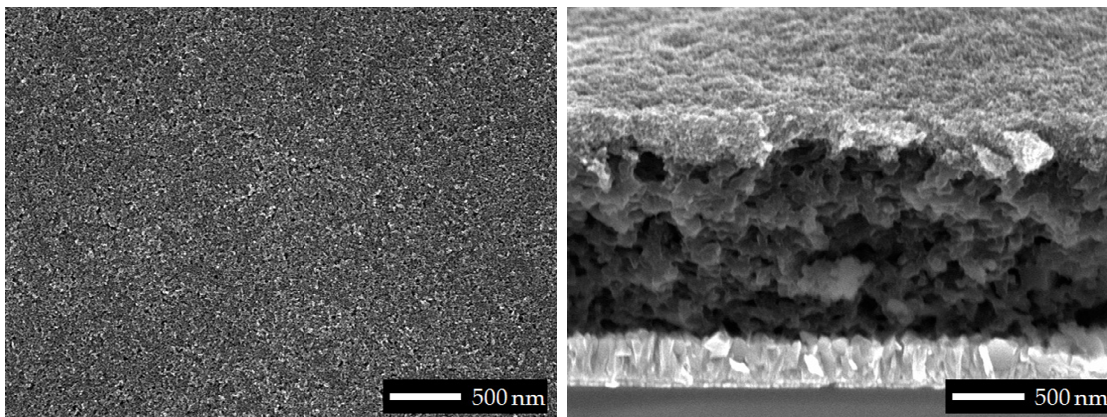


Figure 28. SEMs of a film of Nanoxide HT TiO_2 nanoparticles coating a polyaniline nanofiber film coated with TiO_2 by the Tyzor LA method.

In order to remove the surfactants, it was necessary to slightly alter the architecture of the inverse DSSCs. Instead of spreading the Nanoxide HT paste on top of the photoactive layers of the device, it was spread on the back electrode and then pressed on top of the front electrode. This required moving away from evaporated metal electrodes, and their favorable conformal nature, to a planar electrode surface. FTO was chosen for this application, spread with Nanoxide HT paste and sintered. This simple switch to using sintered nanoparticulate TiO_2 as a coating on the back electrode was all that was required to take the previously nonfunctional polyaniline nanofiber inverse DSSC design and generate a photocurrent with it.

This slight change in architecture led to the discovery that the TiO_2 deposited from the hydrolysis of Tyzor LA does not effectively act as the ETM in the polyaniline nanofiber inverse DSSC. Hydrolysis of titanium salts is known to usually result in an

amorphous titania gel, not a well defined crystal structure. Due to the lack of a developed crystal structure and the remaining OH groups, titania gel has a quasi-conduction band structure with a low density of states. It also has a high level of defects which act as long lifetime trap states.¹⁰² Because of this, the electron injection kinetics and electron mobility are slow. Since devices with hydrolyzed Tyzor LA as the only source of TiO_2 give no measureable external photocurrent, and those with the addition of nanoparticulate anatase TiO_2 do give a photocurrent, it is clear that the defects in the titania gel enhance the recombination rate to a point that it drains away all photogenerated electrons.

Upon hydrothermal treatment of the titania gel prepared by hydrolysis of Tyzor LA, many of the defects are removed. The titania gel undergoes more thorough condensation to remove many of the remaining OH groups and the crystal structure develops more fully. However, this still does not cause a device of this type to generate a measureable photocurrent. Many of the long lifetime trap states are removed and the conduction band develops with a higher density of states but this is also countered by formation of surface states which enhance recombination kinetics.¹⁰²

Some devices were prepared with no titania gel from Tyzor LA in the pores of the polyaniline nanofiber structure, but with the only TiO_2 present in the devices from a sintered Nanoxide HT layer on the FTO back electrode. In these devices the

interface was formed of a planar layer of Nanoxide HT on top of dye-coated polyaniline nanofibers. Despite having a well defined anatase crystal structure in the Nanoxide nanoparticles, these devices also would not generate a measureable photocurrent.

It was found that in order to generate a measureable photocurrent in the polyaniline nanofiber inverse DSSCs, the titania gel from Tyzor LA hydrolysis had to cover the TCPP-coated polyaniline nanofibers and also have a sintered Nanoxide HT-coated FTO electrode pressed on top. Without either, the devices would not function. It is thought that the titania gel acts as an insulating layer at the interface where electrons can be injected either into it or through it and into the anatase nanoparticles on the other side. Once the electrons are in the anatase nanoparticles, they are much more likely to travel through the nanoparticles and to the back electrode, due to their higher conductivity, than they are to go back through the titania gel layer and recombine with holes. Thus, the recombination rate is reduced, allowing the photogenerated electrons to follow their intended path out of the device. While titania gel is not ideal interfacial insulation, due to it separating the dye from the ETM, it functions well as a diagnostic tool.

Since the titania gel from hydrolyzed Tyzor LA has low electron mobility, and has been shown to not function properly as an ETM in the polyaniline nanofiber inverse DSSC, this indicates that the photoexcited electrons generated in the pores of

the polyaniline nanostructure would not be able to diffuse through the titania gel to the back electrode and out of the solar cell, but would rather be lost to recombination. This is supported by an experiment showing that the photocurrent of a typical high surface area polyaniline nanofiber inverse DSSC is very close to that of an inverse DSSC which leaves out the polyaniline nanofibers and is simply a planar photoactive interface. A more thorough explanation of this is given in Section 3.7 and the results are summarized in Table 2.

It was necessary to test if the hydrothermal treatment imparted any morphology change to the titania gel layer, deposited from Tyzor LA, as this could negatively affect performance of the device if the coating became any less conformal. Figure 29 shows that there is no perceivable difference between the treated and untreated films, indicating that the polyaniline/TCPP/TiO₂ interface has not been damaged by the hydrothermal treatment.

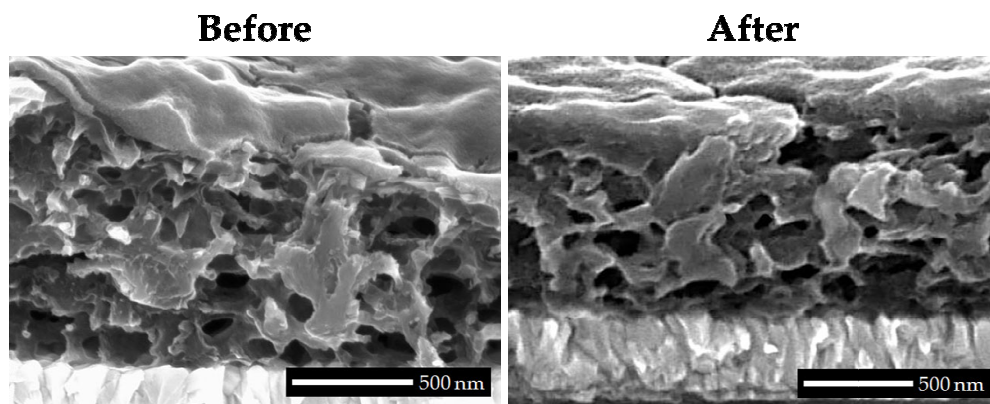


Figure 29. SEMs of TiO₂-coated films of TCPP-coated polyaniline nanofibers before and after undergoing the hydrothermal treatment.

As previously explained, the TiO_2 in a DSSC should ideally be in the anatase phase as this has the best electronic properties for use in this device. It was, unfortunately, not possible to get an XRD spectrum of the TiO_2 from Tyzor LA grown in the actual photovoltaic devices due to instrument limitations. Attempts to acquire XRD spectra of only films of TiO_2 from Tyzor LA, without the complication of the polyaniline and TCPP, also resulted in no signal. It was originally thought that this was due to the films containing too little sample, so a large batch of TiO_2 powder, which homogeneously nucleates out of the Tyzor LA reaction solution, was collected to test. Even this would not give a signal, until it was sent to Rigaku for analysis. Until Rigaku was able to acquire a spectrum (Figure 30), it was thought that the samples were simply completely amorphous, which would explain why no signal could be acquired. Their success with this sample of the TiO_2 powder was due to a higher beam current and different operating geometry than was previously used.

The TiO_2 sample was found to be 100% crystalline anatase. Since this sample was acquired from the homogeneously nucleated TiO_2 , and not that which heterogeneously nucleated on the polyaniline substrate, a direct comparison cannot be made to the TiO_2 deposited on polyaniline nanofibers. It does, however, give an indication that it should be possible to cause the TiO_2 to come out of solution as an anatase coating on the polyaniline, necessary for harvesting photoelectrons from deep in the pores of the nanofiber layer.

XRD spectra of the TiO_2 from Tyzor LA samples are given in Figure 30. The only noticeable difference between the spectra before (bottom) and after (top) the hydrothermal treatment is the slightly sharper peaks after the hydrothermal treatment. This is a result of Oswald ripening which caused the average particle diameter to increase from 27.5 to 28.8 nm during the hydrothermal treatment. This was also accompanied by a decrease in lattice strain from 2.2 to 0.9%, as expected due to the hydrothermal treatment's breaking of strained bonds to form less strained bonds (see Section 1.7).

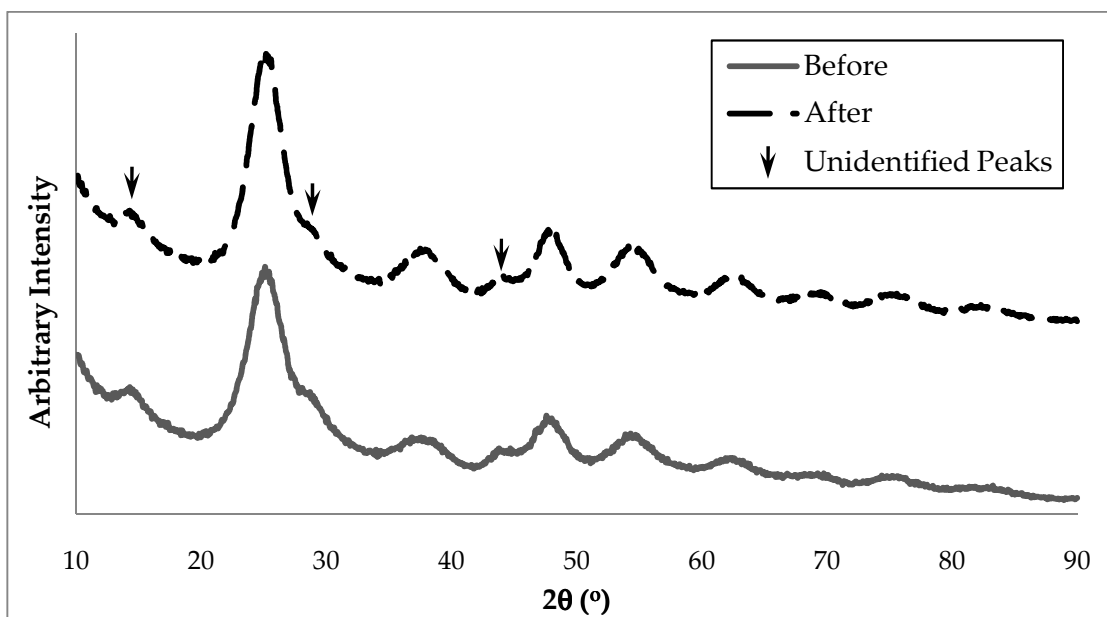


Figure 30. Powder XRD spectra of TiO_2 prepared by hydrolysis of Tyzor LA, before and after the hydrothermal treatment. All peaks, except those labeled as unidentified, are from anatase TiO_2 .

The resistance of TiO₂ films was also tested before and after hydrothermal treatment to determine what effect it has on the conductivity. Films of TiO₂ were deposited on FTO slides under identical conditions. One of these samples underwent the hydrothermal treatment and the other did not. Silver electrodes were then thermally evaporated on top of the TiO₂ and IV curves were taken. It was found that the resistance after hydrothermal treatment was less than 1/10th that of the sample which had not undergone the hydrothermal treatment. This is likely caused by a sintering process resulting in significantly better connections between TiO₂ particles. Also, the particle size increase observed by XRD would decrease the number of contact resistances by decreasing the number of particles along a given conductive pathway. There is also the possibility of an increased proportion of anatase TiO₂, which would increase the electron mobility.

3.5 PCBM Casting

PCBM has been widely studied and characterized for use as an ETM in a variety of thin film solar cells. Therefore, the only aspect which needed to be studied here was its ability to fill the pores in TCPP-coated polyaniline nanofiber films. Varying volumes of a 2 wt% solution of PCBM in chlorobenzene were drop cast onto polyaniline nanofiber films and dried. The resulting films were tested for pore filling by SEM (Figure 31). A bare polyaniline nanofiber film is included (Figure 31-a) for

comparison. Figure 31-b shows the result of 15 μL of the solution being deposited on a typical 12x16 mm polyaniline nanofiber film. Notice the good pore filling but large air pocket at the bottom of the film. In Figure 31-c 25 μL of solution were used and resulted in complete coverage of the polyaniline nanofibers with only minimal air gaps and no extra PCBM layer above the polyaniline nanofibers, which would add unnecessary electrical resistance. Figure 31-d shows the film with 35 μL of solution, Figure 31-e with 50 μL , and Figure 31-f with 75 μL . These last three all have complete, or nearly complete, pore filling but an undesirable PCBM layer of increasing size above the polyaniline nanofibers. For all future work, 25 μL of the solution were used as this gave the best balance of optimum pore filling and nanofiber coverage with minimal extra PCBM to increase electrical resistance.

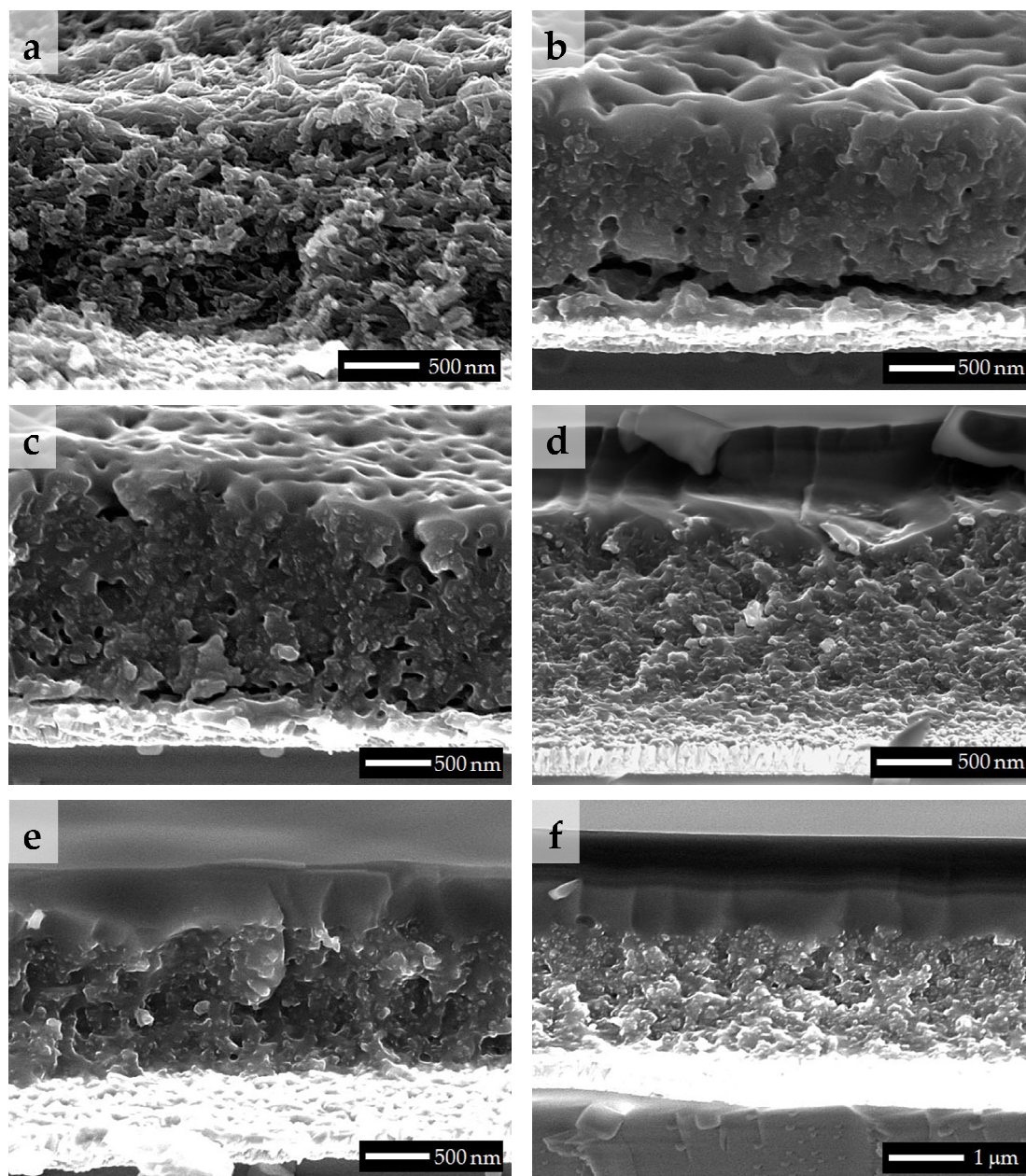


Figure 31. SEMs of (a) bare polyaniline nanofiber films, or coated with PCBM from (b) 15 μL , (c) 25 μL , (d) 35 μL , (e) 50 μL or (f) 75 μL of a 2 wt% solution of PCBM in chlorobenzene.

3.6 Back Electrode Preparation

Back electrodes were first prepared by thermal evaporation of aluminum tracks on top of the ETM (Figure 32-a). Every device using evaporated aluminum as the back electrode was found to function as a photosensitive galvanic cell instead of a photovoltaic cell. It is not known exactly what redox reaction was taking place to generate the current as no combination of half reactions could be found to result in the observed voltage. It was determined that the aluminum and polyaniline were involved, based on the fact that removing either stopped the galvanic reaction. Also, aluminum is a strongly reducing metal and therefore likely to be involved in such a reaction. The conductivity of the polyaniline was also found to greatly decrease in proportion to the amount of charge drained from the device. To eliminate this galvanic reaction a new metal had to be chosen for the back electrode. Aluminum had been originally chosen because its work function, -4.2 eV, is a close match to that of TiO₂ and PCBM, around -4 eV. Unfortunately it is also a strongly reducing metal, with a standard reduction potential of -1.7 V, which gave rise to the undesirable galvanic behavior.

Silver was chosen to replace the aluminum since it is a very weakly reducing metal, with a standard reduction potential of +0.80 V. Devices made with evaporated silver back electrodes did not display galvanic behavior, but they also did not generate a photocurrent. Their current-voltage relationship was found to be

nonlinear, indicating the presence of a built in electric field, an essential property of photovoltaic devices which causes exciton dissociation and gives rise to current directionality. Copper tape was also used as a quick side experiment and had very similar behavior to the devices with silver electrodes.

While switching to silver electrodes demonstrated that the aluminum was involved in the galvanic reaction, and that removing the aluminum from the devices stopped that behavior, it also created another problem. Silver's work function is -4.6 eV which makes it likely that a Schottky barrier formed at the Ag/TiO₂ interface impeding the flow of electrons out of the devices. Another metal had to be found which had both a work function very close to TiO₂ and was a weak reducing agent in order to avoid both formation of a Schottky barrier and the galvanic behavior. The metal needed to be at least 0.8 V less reducing than aluminum, since that is the V_{oc} the galvanic reaction displayed in the original devices. Indium was chosen due to its standard reduction potential of -0.34 V and its work function of -4.1 eV. The low work function of indium makes it ideally suited for creating an ohmic contact with TiO₂ since the work function of TiO₂ in an acidic environment is around -3.9 eV.

Several methods were attempted for using indium as the back electrode due to concerns about the possibility of short circuits developing from the metal evaporation. Attempts to make homemade conductive epoxy and conductive grease with indium powder were unsuccessful, so it was necessary to employ thermal

evaporation again. The devices prepared with thermally evaporated indium electrodes, however, would still not generate a photocurrent.

From here, evaporated metal electrodes were abandoned in favor of a back electrode similar to those commonly used by other researchers in standard DSSCs. The evaporated metal was replaced with electrodes of FTO coated with sintered TiO_2 nanoparticles from doctor bladed Nanoxide HT (Figure 32-b). The sintered TiO_2 nanoparticles were found to be necessary for proper electron injection and transport, explained in further detail in Sections 3.5 and 3.7. Their necessity was due to their electronic properties, not their nanostructure. Planar electrodes, such as FTO, were originally avoided due to their planarity not complementing the morphology of the TiO_2 from Tyzor LA coating the TCPP-coated polyaniline nanofibers of the front electrode. Despite the limited connection between front and back electrodes, when using this new design, the sintered TiO_2 was necessary for proper function of the devices, so this back electrode configuration was used.

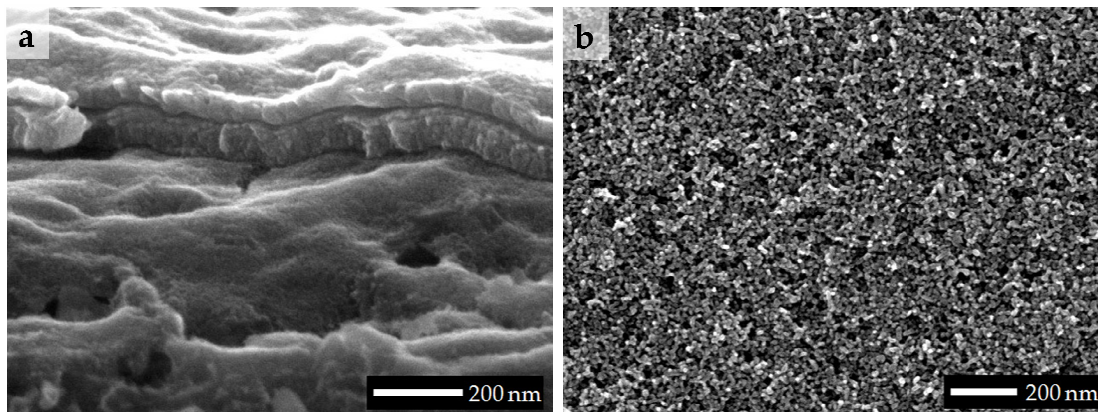


Figure 32. SEMs of a (a) thermally evaporated aluminum electrode on top of Tyzor LA TiO₂ and (b) sintered nanoparticulate TiO₂ from doctor bladed Nanoxide HT on FTO electrodes.

3.7 Photoactivity Characterization

The first complete polyaniline nanofiber inverse dye-sensitized solar cells were constructed of FTO, a polyaniline blocking layer, polyaniline nanofibers, TCPP, TiO₂ from Tyzor LA, the hydrothermal treatment, and evaporated aluminum back electrodes. Devices of this type were also prepared with a single component missing, such as the blocking layer, hydrothermal treatment, or TCPP in order to determine each component's effect on the device performance. In place of TiO₂, some devices were prepared using PCBM as the ETM. Some PCBM devices also had components left out in order to help determine their effect on device performance.

Instead of generating the intended photocurrent, the devices all behaved as photosensitive galvanic cells. They generated not only a light current, but also a lesser

dark current (Figure 33), indicating a redox reaction which was either catalyzed by light or proceeded faster due to decreased resistance of the photoconductive materials in the devices. As the charge was drained from these devices the current dropped and the internal resistance of the devices dramatically increased. This dark and light current behavior is very similar to what Murata et al. noticed when working with Schottky barrier photovoltaic devices and described as a photoaccelerated corrosion of the aluminum electrode.¹⁴²

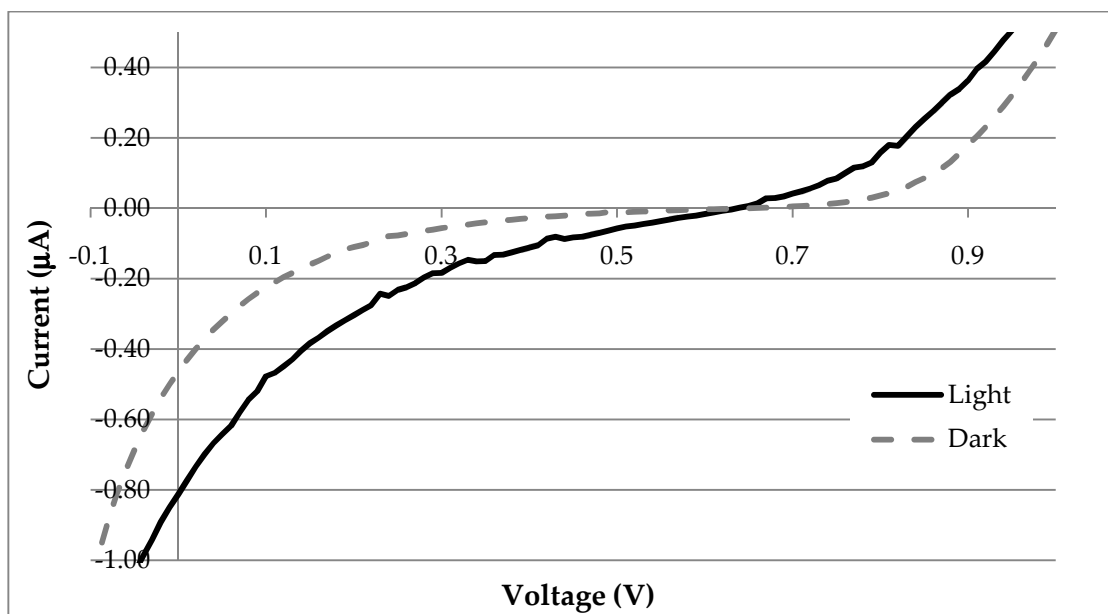


Figure 33. IV curve of a typical polyaniline nanofiber inverse DSSC with a thermally evaporated aluminum back electrode.

In addition to the increase in the internal resistance of the devices, the color of the polyaniline was observed to change from green to blue, indicating a loss of the proper redox and/or protonation state. It was also noticed that in devices with only the very thin polyaniline blocking layer and no polyaniline nanofibers, the dark current dropped to almost zero, indicating that the polyaniline was involved in the galvanic behavior. The most redox reactive component in the devices, the aluminum electrodes, were assumed to be the other half of the redox reaction. Since the polyaniline is critical to this device design, it was necessary to replace the aluminum electrodes.

A variety of alternatives were tested in order to find a better electrode material. Silver conductive grease was found to short circuit every device tested. Copper tape electrodes proved very difficult to work with and resulted in most devices being shorted due to scratching the photoactive film, and those which were not shorted did not generate a photocurrent. Thermally evaporated silver electrodes were also used and found to not generate a photocurrent (Figure 34).

Later work showed that the TiO_2 from Tyzor LA in these devices had been dissolved by a change in the rinsing step necessitated by the previously used rinse dedoping the polyaniline. However, before this was realized, the issue of silver forming a Schottky barrier with TiO_2 was discovered and led to changing the electrode material again.

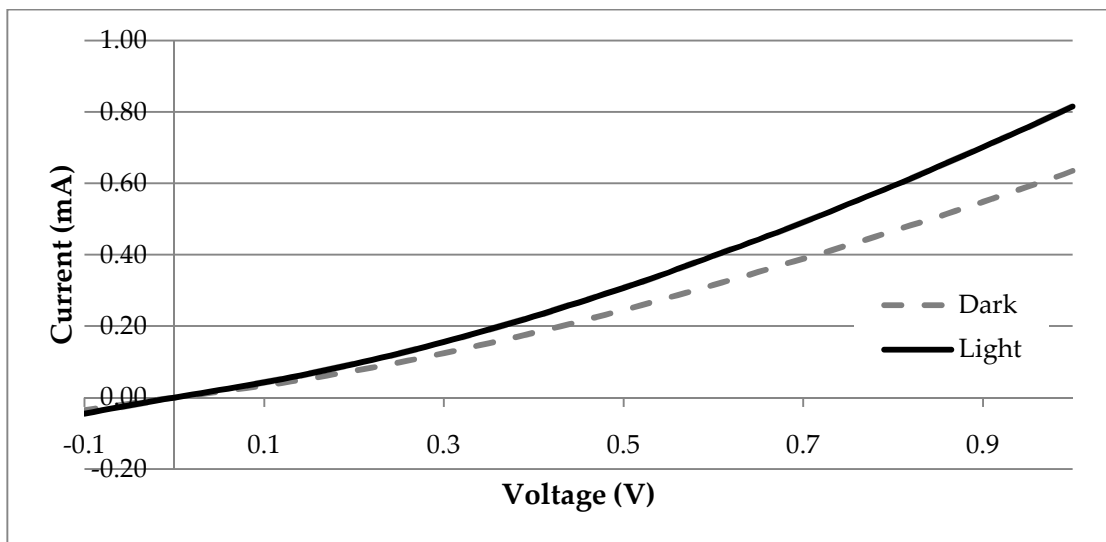


Figure 34. IV curve of a typical polyaniline nanofiber inverse DSSC with a thermally evaporated silver back electrode.

It was necessary to not only have the electrode material be a weak reducing agent to prevent the galvanic reaction, but there must also be an ohmic contact between the electrode material and ETM to avoid a built in electric field resisting the current flow within the device. This means either matching work functions or selecting a metal with a lower work function than the ETM.

Indium meets both of these requirements so it was used as the electrode material. In an attempt to avoid the recurrent problem of a portion of the prepared devices being short circuited, which was thought to be caused by the thermal evaporation, other means were explored to form electrodes of indium. Indium powder was mixed into both epoxy resin and silicon grease to make them

conductive, however the loading levels required for conductivity were unable to be achieved with the available materials.

Therefore, thermal evaporation was used again. Every device prepared with thermally evaporated indium electrodes, and TiO_2 from Tyzor LA as the ETM, was found to be short circuited between the FTO and indium as evidenced by the linear current-voltage relationship and no difference between the dark and light IV curves (Figure 35). It was at this point that, through SEM analysis, it was found that the TiO_2 from Tyzor LA had been dissolved by the rinsing step explained previously.

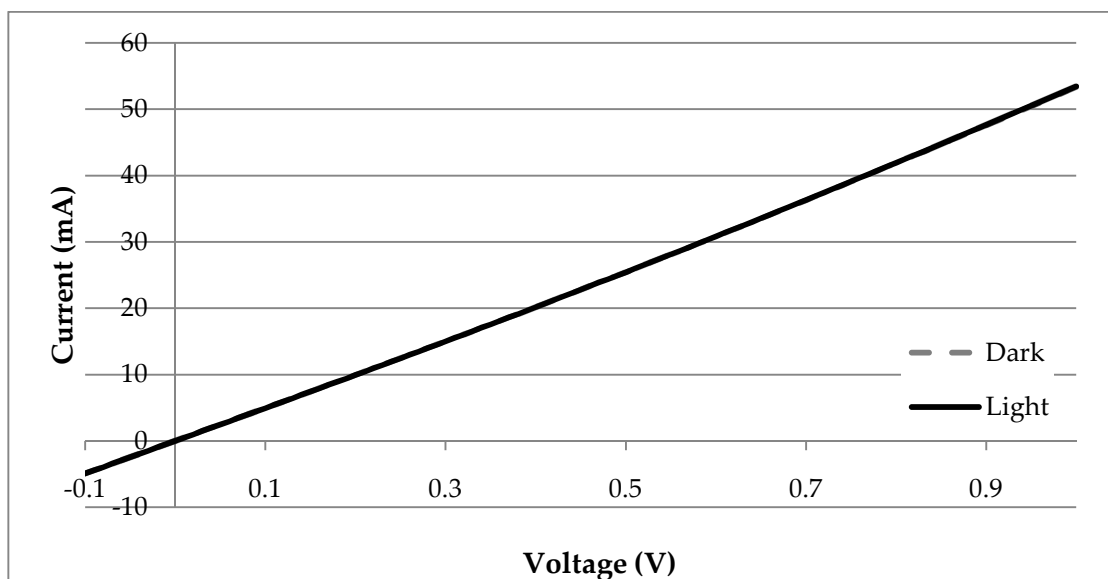


Figure 35. IV curve of a typical polyaniline nanofiber inverse DSSC with a thermally evaporated indium back electrode.

Devices prepared with thermally evaporated indium electrodes and PCBM as the ETM were not shorted, but also did not generate a photocurrent. The devices had quite a sharp breakdown at about 0.9 V where the device resistance changed from 20,000 Ω at 0.1 V applied, to 32.2 Ω at 1.0V applied (Figure 36). There was almost perfect overlap between the dark and light curves, with the only difference being the sharpness of the transition from the pre-breakdown slope to the post-breakdown slope. At this point PCBM was abandoned in an effort to simplify the process of finding and correcting the problem which prevented the polyaniline nanofiber inverse DSSCs from functioning as photovoltaic devices.

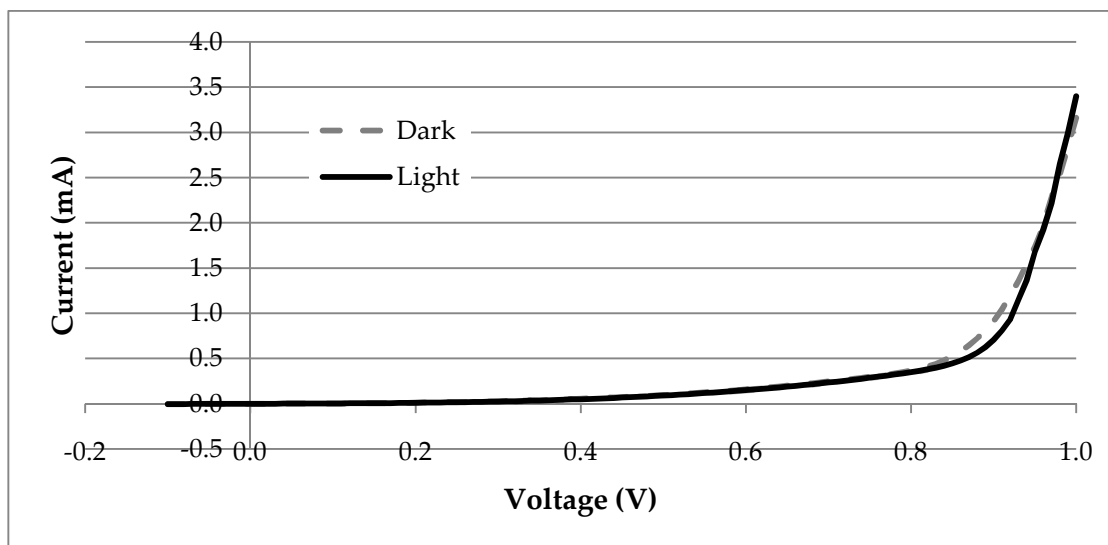


Figure 36. IV curve of a typical polyaniline nanofiber inverse DSSC with a thermally evaporated indium back electrode and PCBM as the electron transport medium.

Since the previous devices using indium electrodes and TiO_2 from Tyzor LA as the ETM were shorted, an additional step was taken to prevent the short circuits in the form of a thin doctor bladed layer of TiO_2 nanoparticles on top of the TiO_2 deposited from Tyzor LA. Devices of this type were no longer shorted but were also found to still not generate a photocurrent. The IV plot was curved and the dark and light lines were almost identical.

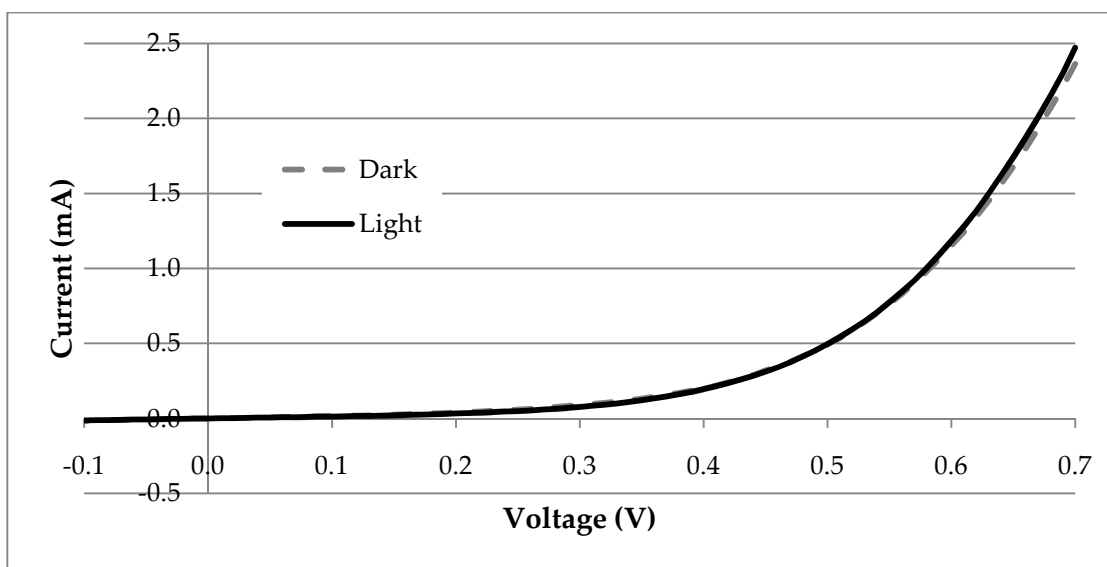


Figure 37. IV curve of a typical polyaniline nanofiber inverse DSSC with a doctor bladed layer of nanoparticulate TiO_2 on top of the TiO_2 deposited from Tyzor LA and a thermally evaporated indium back electrode.

Since there was no clear indication of what was preventing the devices from functioning at this point, an experiment was performed to attempt to expose the

weak link. A series of devices starting with the simplest possible device, using the same materials as a fully formed polyaniline nanofiber inverse DSSC, was constructed. Each device was composed of an FTO slide coated with a polyaniline blocking layer, followed by a doctor bladed layer of Nanoxide HT, and a thermally evaporated indium back electrode. Variations were made on this design by adding one component at a time, such as the TCPP, polyaniline nanofibers, TiO_2 from Tyzor LA hydrolysis, and so on all the way to the fully formed inverse DSSC. The idea was that this would help narrow down which component or components of the device were preventing it from generating a photocurrent. However, none of these device variations were found to generate a photocurrent. Their IV behavior ranged from short circuited, as in Figure 35, to strongly curved, as in Figure 37.

To determine if these devices behaved as diodes, indicating the presence of the built in electric field necessary for exciton dissociation and current directionality, IV scans were taken from -1 V to +1 V and rectification ratios were calculated. An example is given in Figure 38, for which the rectification ratio was calculated to be 15.2. The IV plot is curved as it should be, and the internal electric field is present. The only thing missing is the photocurrent, indicating that the photoexcitation is being lost internally to a recombination process.

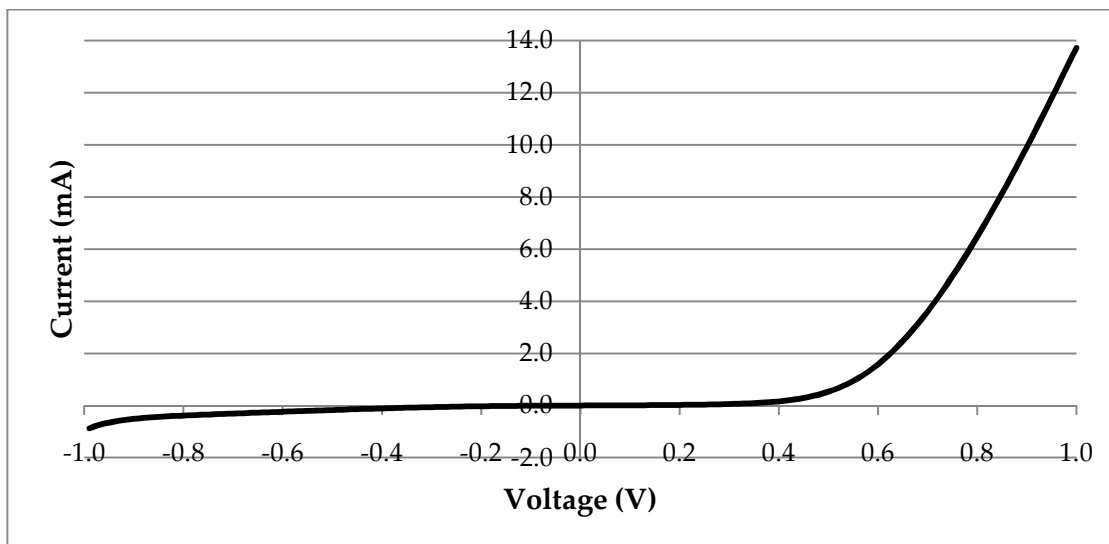


Figure 38. IV curve showing current rectification from a polyaniline nanofiber inverse DSSC with a doctor bladed layer of nanoparticulate TiO_2 on top of the TiO_2 deposited from Tyzor LA and a thermally evaporated indium back electrode.

Since not even the simplest version of an inverse DSSC would generate a photocurrent, another step back was taken. This time several devices were prepared, as close to standard DSSC construction as possible, using the same materials as in a polyaniline nanofiber inverse DSSC. The simplest version was constructed on two FTO electrodes. One electrode had a thick polyaniline blocking layer cast on it and the other electrode was coated with a sintered layer of doctor bladed Nanoxide HT TiO_2 nanoparticles coated with TCPP. Note that in these devices the thermally evaporated metal electrodes were replaced with sintered TiO_2 nanoparticles on FTO, and the TCPP was adsorbed onto the TiO_2 nanoparticles rather than covalently bound

on the polyaniline. The two electrodes were simply pressed together forming a planar interface consisting of numerous point contacts from where the TiO_2 nanoparticles touched the polyaniline layer. This is certainly not an ideal interface, but simply used as a means to elucidate the problem which had been preventing the inverse DSSCs from functioning properly. These standard construction devices were the first in this project to generate a photocurrent. The first device of this type had a V_{oc} of 0.17 V and an I_{sc} of 3.5 nA/cm². After three days this device was tested again and its performance was found to have improved dramatically, to a V_{oc} of 0.31 V and an I_{sc} of 13.5 nA/cm² (Figure 39). It is thought that this is caused by a relaxation of the TCPP on the TiO_2 nanoparticles, in which they spread out more evenly and minimize pinholes in the coating, thus reducing contact between the TiO_2 and polyaniline and thereby the shunt current. Figure 39 does not include the dark current data due to a high level of noise.

More devices of this type were prepared and it was found to be quite hit-and-miss with reproducibly making functional devices. Many would have the proper IV curve shape but no photocurrent. Since this indicates loss of photoexcitation to a recombination process, devices were prepared with deoxycholic acid coadsorbed on the TiO_2 with the TCPP to better insulate the interface. Every device of this type generated a photocurrent, further supporting the recombination idea, with the best

device giving a V_{oc} of 0.18 V and an I_{sc} of 7.0 nA/cm². This device was also tested three days later and found to improve to a V_{oc} of 0.17 V and an I_{sc} of 52 nA/cm².

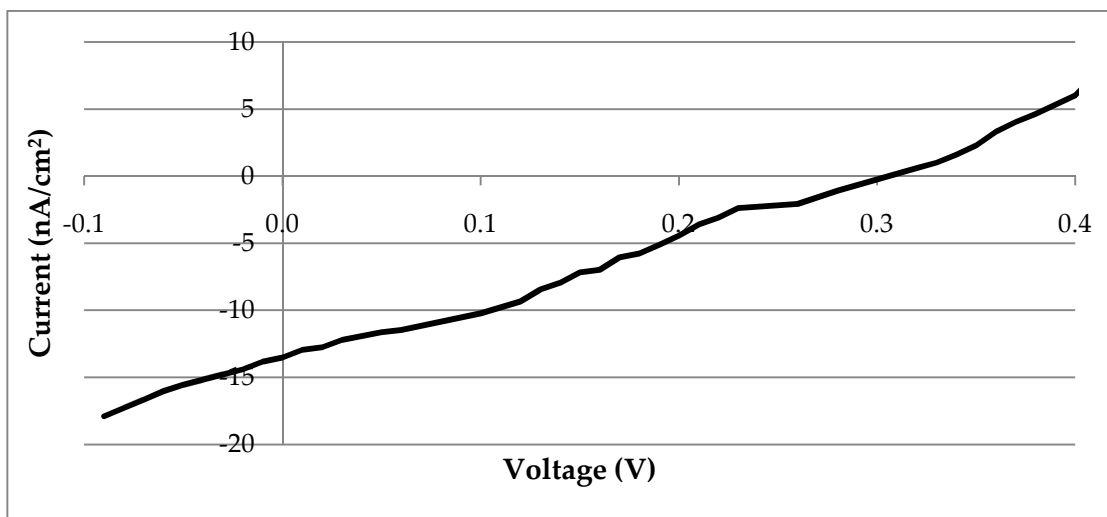


Figure 39. IV curve of a simple standard DSSC made by pressing two FTO electrodes together, one with a polyaniline blocking layer and the other with a TCPP-coated sintered TiO₂ nanoparticle coating.

An interesting observation is made when comparing the dark currents of devices which did not generate a measureable photocurrent and those that did. The dark currents of complete polyaniline nanofiber inverse DSSCs which did not generate a measureable photocurrent were on the order of micro to milliamps, while the dark currents of functional devices were on the order of nanoamps, three to six orders of magnitude lower. Dark currents give an indication of the rate of

recombination reactions within the device, but a direct comparison to recombination rates in devices functioning under exposure to light cannot be made due to the photoconductive nature of many of the materials employed. However, the observed difference in dark current of three to six orders of magnitude between the functional and nonfunctional devices clearly points to an inadequately insulated interface.

The two main recombination processes at the interface are electrons from TiO_2 reducing the oxidized dye or reducing the polyaniline. It is well known that the rate of electrons in TiO_2 reducing the oxidized dye is slow, assuming there is an adequate rate of electron transport out of the TiO_2 , leaving the reduction of polyaniline by electrons in TiO_2 as the culprit for the fast recombination kinetics. Fortunately, this reaction is the easiest of the two to prevent, and can be accomplished by simply providing adequate insulation at the interface.

For devices with slow recombination kinetics, the interfacial insulation provided by the dye proves sufficient for efficient device function. However, devices with fast enough recombination kinetics require additional interfacial insulation to prevent complete loss of the photocurrent to recombination, as is observed in a standard liquid electrolyte DSSC using bromide as the hole conductor instead of iodide.¹⁴³ Nevertheless, with proper insulation these devices can be made to generate a measureable photocurrent. In conventional DSSCs, the insulation is often provided

by a coadsorbent^{144,145} – typically a long molecule with a carboxylic acid moiety which adsorbs onto the TiO₂ and fills in the pinholes in the dye coating.

Since using DCA as a coadsorbent was successful in insulating the interface of a standard architecture DSSC, it was necessary to find a blocking agent which could be used in an inverse DSSC. Because the attachment method used was the same as that used to attach the dye, it was necessary to avoid functional groups in the blocking agent which would react with thionyl chloride, other than the carboxylic acid through which the attachment would occur. Decanoic acid was chosen as it meets this criterion as well as having a length slightly shorter than the width of a TCPP molecule. This allows the dye to protrude beyond the decanoic acid so electron injection into TiO₂ would not be hindered.

To ensure that decanoic acid would function as a blocking agent, similar to DCA, it was tested in a standard architecture DSSC. Dark IV curves of standard architecture DSSCs prepared with deoxycholic acid, decanoic acid or no blocking agent were taken and compared (Figure 40). The dark current gives an indication of the recombination rate by measuring the leakage current within the device. As shown, the dark current decreased with both blocking agents tested, and more so with decanoic acid, indicating that it does function as an effective blocking agent. In addition to what Figure 40 shows, the use of either blocking agent dramatically increases the percentage of prepared devices which generated a measureable

photocurrent over those devices which did not generate a photocurrent, even though they were not shorted.

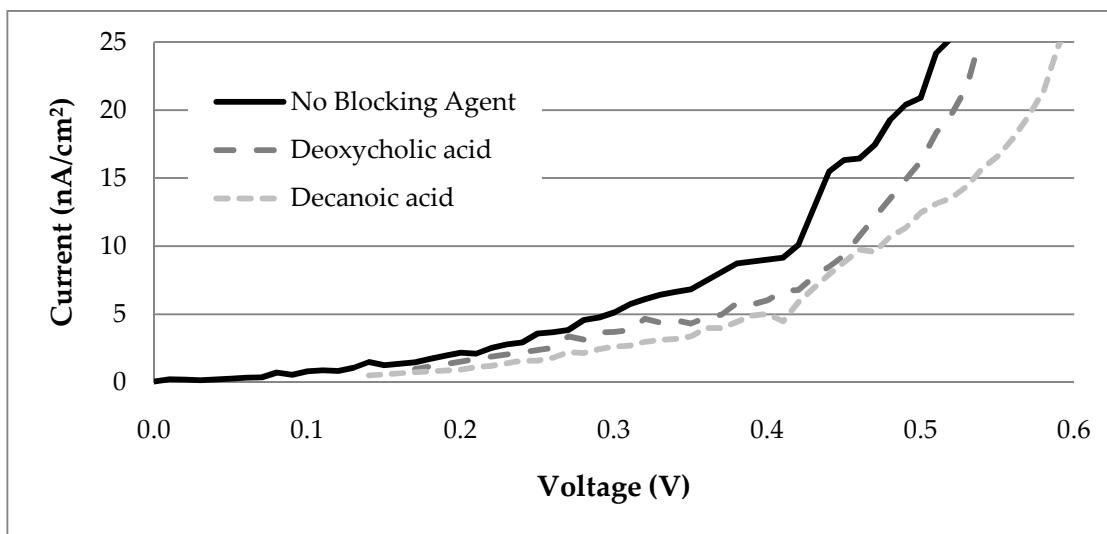


Figure 40. IV curves in the dark of standard construction DSSCs showing the effect of coadsorbents for passivating the interface.

Now that functional devices could be prepared in a standard DSSC architecture, the next step was to take what was learned and apply it to inverse DSSCs in order to make them functional. Inverse DSSCs were prepared with a number of variations in order to help determine the function and effect on performance of each component. At this point, functional devices were able to be reliably and reproducibly prepared. A typical IV curve is given in Figure 41, where the dark curve is seen to pass through the origin, indicating no galvanic reaction, and

the light curve is seen to clearly have a photocurrent. The specific architecture and performance figures for select types of these devices are given in Table 2. Only V_{oc} and I_{sc} are recorded for the performance figures due to the very low currents generated by these devices and the resultant noise in the IV curves preventing determination of meaningful resistance, power, efficiency, and other performance figures.

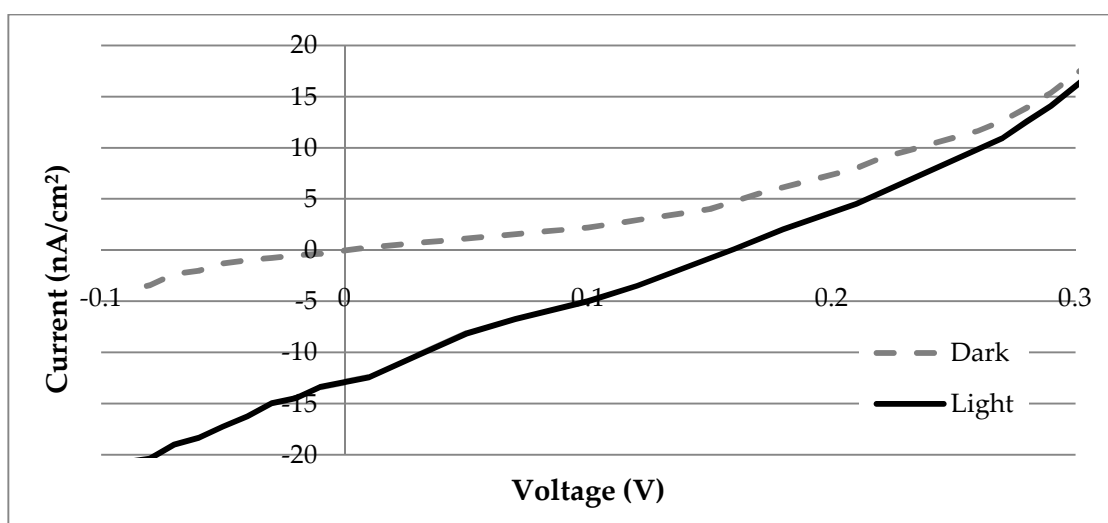


Figure 41. IV curve of a typical complete and functional polyaniline nanofiber inverse DSSC.

Type	Polyaniline Blocking Layer	Polyaniline Nanofibers	TCPP	Decanoic acid	TiO ₂ from Tyzor LA	Nonsintered TiO ₂ Nanoparticles	Sintered TiO ₂ Nanoparticles	Avg V _{oc} (V)	Avg I _{sc} (nA/cm ²)
1	X		X				X	-	-
2	X		X		X		X	0.22	7.0
3	X	X	X				X	-	-
4	X	X	X		X			-	-
5	X	X	X		X		X	0.17	5.7
6	X	X	X	X	X		X	0.14	30
7	X	X	X		X	X		-	-

Table 2. Architecture and performance figures for select polyaniline nanofiber inverse DSSC types. The X indicates which components are present in each device type. The double line indicates the division between the front and back electrodes, each of which is prepared on an FTO slide.

This experiment shed significant light on why the previous inverse DSSCs did not generate measureable photocurrents. Comparing devices of Type 1 to those of Type 2 as well as comparing Type 3 to Type 5 demonstrates that the devices will not function without the TiO₂ deposited from Tyzor LA. It is thought that this TiO₂, really titania gel, acts as an insulating layer at the interface which slows the rate of recombination thus allowing the generated photocurrent to move out of the

photovoltaic cell into an external circuit instead of being lost to recombination within the device.

The devices also needed to have the nanoparticulate anatase TiO_2 present, as shown by comparing Type 4 to Type 5. The anatase has the well defined, and properly positioned, conduction band necessary for electron injection from the dye and for electron transport out of the device. The titania gel deposited from Tyzor LA does not have the appropriate electronic properties to function as an ETM, so this well defined anatase is necessary. In addition to the anatase TiO_2 simply being present, it also was found necessary to have it as a sintered layer on the FTO back electrode for proper device function. This can be seen by comparing Type 5 to Type 7. If not sintered, the surfactants and other additives from the TiO_2 paste are still present between nanoparticles and decrease the conductivity of the film. This was found to prevent the devices from generating a measureable photocurrent.

The effect of having the high surface area from the polyaniline nanofibers is shown by comparing Type 2 to Type 5. Both the V_{oc} and I_{sc} are found to decrease with the presence of the nanofibers. In the design of the inverse DSSC, the polyaniline nanofibers serve as the agent which gives rise to the high surface area structure of the devices. The high surface area is necessary in order to achieve both a monolayer of dye, for optimal exciton dissociation and electron injection, and a high enough concentration of dye to absorb most, or all, of the incident light. For the high surface

area component to be effective, both the electron conductor and hole conductor in the interpenetrating network must have high conductivity in order to efficiently shuttle electrons and holes out to the electrodes. The problem in this device is that the titania gel deposited from Tyzor LA was found to have low conductivity, resulting in its inability to efficiently shuttle electrons to the back electrode. Rather than the electrons which had been injected into the titania gel deep in the pores of the device being able to travel through the titania gel to the back electrode, the low conductivity means that essentially all of these free electrons are lost to recombination. So the only photoexcitations which can add to the photocurrent are those generated very close to the planar interface between the polyaniline and the layer of nanoparticulate anatase TiO_2 sintered on the back FTO electrode.

As seen by comparing Type 2 and Type 5, the performance is not the same between devices with polyaniline nanofibers and those without. The devices with the nanofibers actually perform worse. This is due to the holes generated at the planar interface still needing to travel all the way through the nanofiber layer to the front electrode. Since this entire pathway is made of polyaniline nanofibers coated with titania gel, that gives a large surface area for the holes to recombine with electrons in the titania gel.

To further explore the need for good insulation at the interface to counteract the fast recombination rate, decanoic acid was attached to the polyaniline nanofibers

in some of the devices after the TCPP attachment step. This is seen in comparing Type 5 to Type 6, which shows a dramatic improvement in device performance. The V_{oc} does drop slightly, but this is more than made up for by the greater than five times improvement in the I_{sc} . This demonstrates that the decanoic acid is effective at filling the pinholes between TCPP molecules on the polyaniline nanofibers and therefore at preventing recombination at the interface. It also adds support to the idea that fast recombination kinetics is one of the main hindrances to better performance in polyaniline nanofiber inverse DSSCs.

Another observation, not shown in the table, is that the hydrothermal treatment was found to not impact the device performance in any significant way. For example, one of the devices prepared had a V_{oc} of 0.15 V and an I_{sc} of 13 nA/cm² before the hydrothermal treatment, and a V_{oc} of 0.13 V and an I_{sc} of 13 nA/cm² after. The hydrothermal treatment of titania gel from Tyzor LA, which is supposed to convert the titania gel into well defined anatase, was also found to not be a functional replacement for the sintered nanoparticulate TiO₂ as the ETM.

The output current of a complete inverse DSSC was recorded with time and found to slowly decay. Over the period of five hours the decay could be fit to a line (Figure 42). Extrapolating this rate resulted in the output current going to zero after about 24 hours. This is likely due to the same degradation process observed in the aging of polyaniline nanofibers, thought to be an irreversible oxidation, but has not

been explored experimentally. It is also possible that this decay could level off at a time beyond what was tested and go on to have a long functional lifetime.

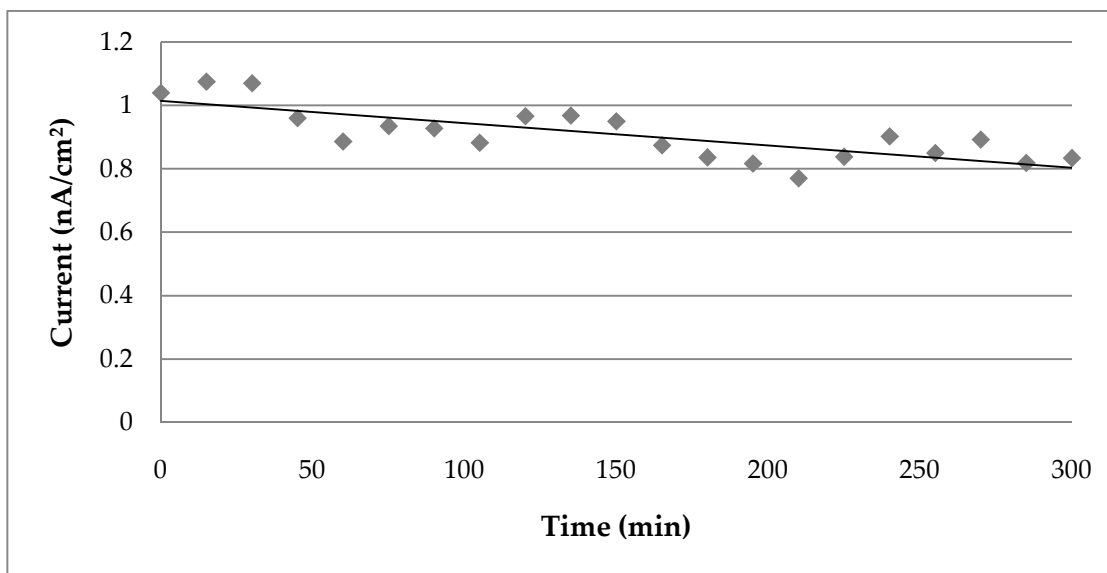


Figure 42. Plot of a polyaniline nanofiber inverse DSSC's current output with time.

The light intensity responsiveness was also tested for the inverse DSSCs (Figure 43). The V_{oc} was found to increase slightly with increasing light intensity. The I_{sc} was found to increase sharply near the low end of light intensity and then began to level off above one Sun. Due to the high level of noise in the data from the low currents, the light intensity which gives peak efficiency was unable to be calculated.

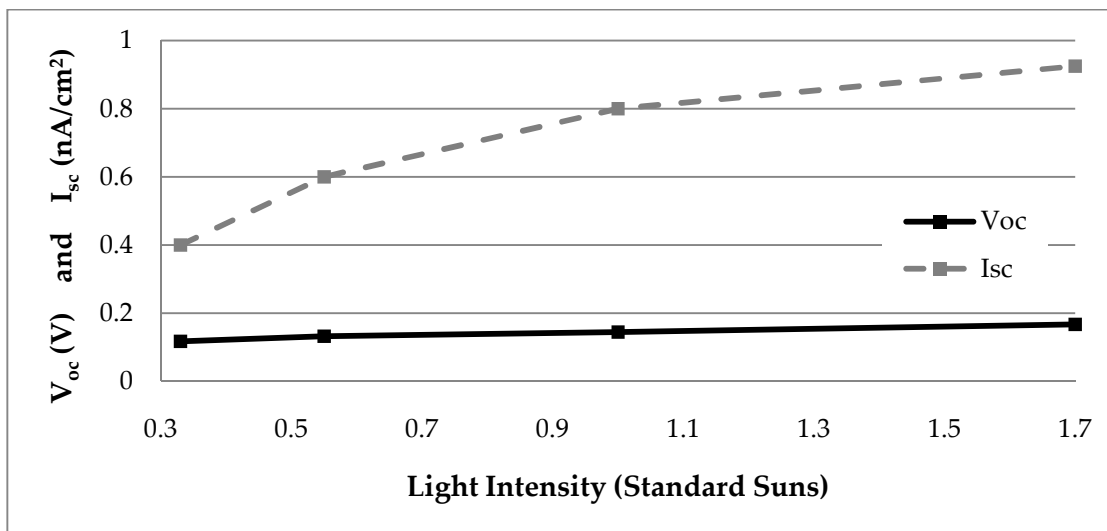


Figure 43. Plot of V_{oc} and I_{sc} vs. light intensity for a complete polyaniline nanofiber inverse DSSC.

None of the devices which used PCBM as the ETM in place of TiO_2 were found to generate a measureable photocurrent. This is likely due to the same fast recombination kinetics found to be responsible for the problems with the TiO_2 devices. Another possible factor is PCBM's oxygen sensitivity and the inability to keep the devices in an inert atmosphere throughout preparation, due to the procedures and equipment employed. Oxidative damage is known to change the electronic properties of fullerenes and could likely contribute to nonfunctionality of the devices.

While functional polyaniline nanofiber inverse DSSCs can now be reliably produced, their performance is poor. By addressing the fast recombination kinetics

with improved interfacial insulation, and addressing the inability of the titania gel to shuttle electrons out of the pores using either a treatment which will convert it to anatase or a different ETM, dramatic improvements in device performance could be realized.

CHAPTER 4. CONCLUSIONS

Functional polyaniline nanofiber inverse dye-sensitized solar cells were successfully prepared and tested. They were constructed on FTO glass slides in a layer-by-layer approach. The first layer was a polyaniline blocking layer, followed by polyaniline nanofibers. The nanofibers were coated with TCPP dye and then with titania gel from Tyzor LA hydrolysis. The back electrode, made of sintered anatase TiO_2 nanoparticles on FTO, was pressed on top.

Polyaniline blocking layers of 10-20 nm thickness were prepared by spin coating from a filtered solution of polyaniline in *m*-cresol. The layers completely covered the FTO substrate and contained no observable pinholes.

Polyaniline nanofiber layers, around 700 nm thick, were deposited from an aqueous colloid onto the polyaniline blocking layer. Strong adhesion was observed between these two layers. The conductivity of pressed pellets of the polyaniline nanofibers was measured to be 0.8 S/cm, in good agreement with polyaniline from other researchers. The HOMO of the polyaniline nanofibers was determined to be -4.6 eV, which is in very good agreement with other researcher's measurements, and positioned properly for device function.

TCPP was covalently attached to the polyaniline nanofibers by a Friedel-Crafts acylation. After optimization of the reaction conditions, surface coverage was

calculated to be 120%, indicating some degree of penetration into the nanofibers. The TCPP attachment process caused only a slight morphology change in the polyaniline nanofibers, leaving the necessary porous structure intact. Decanoic acid was found to be a successful interfacial insulator to prevent recombination. The photocurrents of devices with decanoic acid attached were five times higher than those without.

Titania gel was deposited from Tyzor LA by a controlled hydrolysis reaction. Thin films were prepared which completely coated the TCPP-coated polyaniline nanofiber structure. Titania gel was found to be ineffective as an ETM due to its unfavorable electronic properties. It was, however, found to function effectively as interfacial insulation slowing the rate of recombination between electrons in the TiO_2 and holes in the polyaniline enough to allow a measureable photocurrent to be generated. The high surface area of the devices was found to have a hindering effect on the photocurrent, rather than improving it, because the poor electronic properties of the titania gel prevented it from being able to transport photoelectrons generated deep in the film to the back electrode. Also, the holes in the polyaniline still needed to travel through the entire nanofiber film, with its high surface area contacting the titania gel, giving plenty of opportunities for recombination. The hydrothermal treatment of the titania gel was found to have no significant effect on the performance of the devices.

Sintered TiO_2 nanoparticle films were prepared by doctor blading Solaronix Nanoxide HT on the FTO back electrode. This layer was found to be necessary for device function, as it acted as the ETM in place of the titania gel.

While the polyaniline nanofiber inverse DSSCs did generate a measureable photocurrent, their performance was poor. This was found to be caused by the fast recombination kinetics within the devices, the inability of the titania gel to conduct electrons out of the pores in the nanofiber film, and the non-ideal interfacial insulation layer of titania gel which covered the dye and hindered electron injection into the nanoparticulate anatase TiO_2 . Dramatic improvements in device performance can be expected by addressing these shortcomings.

REFERENCES

- (1) Li, B.; Wang, L.; Kang, B.; Wang, P.; Qiu, Y. Review of recent progress in solid-state dye-sensitized solar cells. *Sol. Energy Mater. Sol. Cells* **2006**, *90*, 549-573.
- (2) Ameri, T.; Dennler, G.; Lungenschmied, C.; Brabec, C. J. Organic tandem solar cells: A review. *Energy Environ. Sci.* **2009**, *2*, 347-363.
- (3) Becquerel, E. Mémoire sur les effets électriques produits sous l'influence des rayons solaires. *C. R. Acad. Sci.* **1839**, *9*, 561-567.
- (4) Chapin, D. M.; Fuller, C. S.; Pearson, G. L. A new silicon p-n junction photocell for converting solar radiation into electrical power. *J. Appl. Phys.* **1954**, *25*, 676.
- (5) U.S. Energy Information Administration, *U.S. Energy Consumption by Energy Source*. http://www.eia.doe.gov/cneaf/alternate/page/renew_energy_consump/table1.html Accessed 4/13/2010,
- (6) Grätzel, M. Solar energy conversion by dye-sensitized photovoltaic cells. *Inorg. Chem.* **2005**, *44*, 6841.
- (7) Smestad, G. P.; Spiekermann, S.; Kowalik, J.; Grant, C. D.; Schwartzberg, A. M.; Zhang, J.; Tolbert, L. M.; Moons, E. A technique to compare polythiophene solid-state dye sensitized TiO₂ solar cells to liquid junction devices. *Sol. Energy Mater. Sol. Cell* **2003**, *76*, 85-105.
- (8) Putseiko, E. K.; Terenin, A. N. Photosensitization of the internal photoeffect in zinc oxide and other semiconductors by adsorbed dyes. *Zh. Fiz. Khim.* **1949**, *23*, 676-688.
- (9) Terepin, A. N.; Putseiko, E. K. Sensitization by dyes of internal photoeffect in semiconductors. *Usp. Nauch. Foto.* **1955**, *3*, 101-109.
- (10) Gerischer, H.; Michel-Beyerle, M. E.; Rebentrost, F.; Tributsch, H. Sensitization of charge injection into semiconductors with large band gap. *Electrochim. Acta* **1968**, *13*, 1509-15.
- (11) Tributsch, H. Electrochemical studies of sensitization properties and photochemical behavior of pseudoisocyanine dye aggregates on zinc oxide electrodes. *Ber. Bunsenges. Phys. Chem.* **1969**, *73*, 582-90.

- (12) Amadelli, R.; Argazzi, R.; Bignoz, C. A.; Scandola, F. Design of antenna-sensitizer polynuclear complexes. Sensitization of titanium dioxide with $[\text{Ru}(\text{bpy})_2(\text{CN})_2]_2\text{Ru}(\text{bpy}(\text{COO})_2)_2^{2-}$. *J. Am. Chem. Soc.* **1990**, *112*, 7099-103.
- (13) Nazeeruddin, M. K.; Liska, P.; Moser, J.; Vlachopoulos, N.; Graetzel, M. Conversion of light into electricity with trinuclear ruthenium complexes adsorbed on textured titanium dioxide films. *Helv. Chim. Acta* **1990**, *73*, 1788-803.
- (14) Tsubomura, H.; Matsumura, M.; Nakatani, K.; Nomura, Y. Dye sensitization at the zinc oxide electrodes in "wet" photocells. *Proc. - Electrochem. Soc.* **1977**, 77-3, 178-85.
- (15) Willig, F.; Eichberger, R.; Sundaresan, N. S.; Parkinson, B. A. Experimental time scale of Gerischer's distribution curves for electron-transfer reactions at semiconductor electrodes. *J. Am. Chem. Soc.* **1990**, *112*, 2702-2707.
- (16) Matsumura, M.; Nomura, Y.; Tsubomura, H. Dye-sensitization on the Photocurrent at Zinc Oxide Electrode in Aqueous Electrolyte Solution. *Bull. Chem. Soc. Jpn.* **1977**, *50*, 2533-2537.
- (17) Alonso V., N.; Beley, M.; Chartier, P.; Ern, V. Dye sensitization of ceramic semiconducting electrodes for photoelectrochemical conversion. *Revue Phys. Appl.* **1981**, *16*, 5-10.
- (18) O'Regan, B.; Moser, J.; Anderson, M.; Grätzel, M. Vectorial electron injection into transparent semiconductor membranes and electric field effects on the dynamics of light-induced charge separation. *J. Phys. Chem.* **1990**, *94*, 8720-8726.
- (19) Tsubomura, H.; Matsumura, M. Wet-type solar cell using a semiconductor. *Kagaku* **1997**, *32*, 238-40.
- (20) Tributsch, H.; Gerischer, H. Electrochemical studies on the mechanism of sensitization and supersensitization of zinc oxide single crystals. *Ber. Bunsenges. Phys. Chem.* **1969**, *73*, 251-60.
- (21) Hauffe, K.; Danzmann, H. J.; Pusch, H.; Range, J.; Volz, H. New experiments on the sensitization of zinc oxide by means of the electrochemical cell technique. *J. Electrochem. Soc.* **1970**, *117*, 993-9.
- (22) Hauffe, K.; Bode, U. Photosensitization of the charge transfer across zinc oxide interfaces by binary dye mixtures. *Faraday Discuss. Chem. Soc.* **1975**, *58*, 281-9.

- (23) Memming, R.; Tributsch, H. Electrochemical investigations on the spectral sensitization of gallium phosphide electrodes. *J. Phys. Chem.* **1971**, *75*, 562-70.
- (24) Memming, R. Photochemical and electrochemical processes of excited dyes at semiconductor and metal electrodes. *Photochem. Photobiol.* **1972**, *16*, 325-33.
- (25) Fujishima, A.; Iwase, T.; Watanabe, T.; Honda, K. Evidence for the oxidation of supersensitizers during photoelectrochemical supersensitization at the cadmium sulfide electrode. *J. Am. Chem. Soc.* **1975**, *97*, 4134-5.
- (26) Matsumura, M.; Nomura, Y.; Tsubomura, H. Chelation effect of alizarin dyes on the semiconductor-aqueous solution systems. *Bull. Chem. Soc. Jpn.* **1976**, *49*, 1409-10.
- (27) Tsubomura, H.; Matsumura, M.; Nomura, Y.; Amamiya, T. Dye sensitized zinc oxide: aqueous electrolyte: platinum photocell. *Nature* **1976**, *261*, 402-3.
- (28) O'Regan, B.; Grätzel, M. A low-cost, high-efficiency solar cell based on dye-sensitized colloidal titanium dioxide films. *Nature* **1991**, *353*, 737.
- (29) Nogueira, A. F.; Longo, C.; De Paoli, M.-A. Polymers in dye sensitized solar cells: overview and perspectives. *Coord. Chem. Rev.* **2004**, *248*, 1455-1468.
- (30) Luzzati, S.; Basso, M.; Catellani, M.; Brabec, C. J.; Gebeyehu, D.; Sariciftci, N. S. Photo-induced transfer from a dithieno-based polymer to TiO₂. *Thin Solid Films* **2002**, *403-404*, 52-56.
- (31) Gebeyehu, D.; Brabec, C. J.; Sariciftci, N. S. Solid-state organic / inorganic hybrid solar cells based on conjugated polymers and dye-sensitized TiO₂ electrodes. *Thin Solid Films* **2002**, *403-404*, 271-274.
- (32) Wang, P.; Zakeeruddin, S. M.; Moser, J. E.; Grätzel, M. A new ionic liquid electrolyte enhances the conversion efficiency of dye-sensitized solar cells. *J. Phys. Chem. B* **2003**, *107*, 13280.
- (33) Wang, P.; Zakeeruddin, S. M.; Moser, J.-E.; Humphry-Baker, R.; Grätzel, M. A solvent-free, SeCN⁻/(SeCN)³⁻ based ionic liquid electrolyte for high-efficiency dye-sensitized nanocrystalline solar cells. *J. Am. Chem. Soc.* **2004**, *126*, 7164-7165.

- (34) Komiya, R.; Han, L.; Yamanaka, R.; Islam, A.; Mitate, T. Highly efficient quasi-solid state dye-sensitized solar cell with ion conducting polymer electrolyte. *J. Photochem. Photobiol. A-Chem.* **2004**, *164*, 123.
- (35) Yum, J.-H.; Hagberg, D. P.; Moon, S.-J.; Karlsson, K. M.; Marinado, T.; Sun, L.; Hagfeldt, A.; Nazeeruddin, M. K.; Grätzel, M. A light-resistant organic sensitizer for solar-cell applications. *Angew. Chem. Int. Ed.* **2009**, *48*, 1576-1580.
- (36) Tan, S.; Xue, B.; Wan, M.; Meng, Q.; Li, Y.; Jiang, L.; Zhu, D. Property influence of polyanilines on photovoltaic behaviors of dye-sensitized solar cells. *Langmuir* **2004**, *20*, 2934-2937.
- (37) Gebeyehu, D.; Brabec, C. J.; Sariciftci, N. S.; Vangeneugden, D.; Kiebooms, R.; Vanderzande, D.; Kienberger, F.; Schindler, H. Hybrid solar cells based on dye-sensitized nanoporous TiO₂ electrodes and conjugated polymers as hole transport materials. *Synth. Met.* **2002**, *125*, 279-287.
- (38) Spiekermann, S.; Smestad, G.; Kowalik, J.; Tolbert, L. M.; Grätzel, M. Poly(4-undecyl-2,2'-bithiophene) as a hole conductor in solid state dye sensitized titanium dioxide solar cells. *Synth. Met.* **2001**, *121*, 1603-1604.
- (39) Senadeera, R.; Fukuri, N.; Saito, Y.; Kitamura, T.; Wada, Y.; Yanagida, S. Volatile solvent-free solid-state polymer-sensitized TiO₂ solar cells with poly(3,4-ethylenedioxythiophene) as a hole-transport medium. *Chem. Commun.* **2005**, 2259-2261.
- (40) Saito, Y.; Azechi, T.; Kitamura, T.; Hasegawa, Y.; Wada, Y.; Yanagida, S. Photo-sensitizing ruthenium complexes for solid state dye solar cells in combination with conducting polymers as hole conductors. *Coord. Chem. Rev.* **2004**, *248*, 1469-1478.
- (41) van Hal, P. A.; Christiaans, M. P. T.; Wienk, M. M.; Kroon, J. M.; Janssen, R. A. J. Photoinduced electron transfer from conjugated polymers to TiO₂. *J. Phys. Chem. B* **1999**, *103*, 4352-4359.
- (42) Däubler, T. K.; Glowacki, I.; Scherf, U.; Ulanski, J.; Hörhold, H.-H.; Neher, D. Photogeneration and transport of charge carriers in hybrid materials of conjugated polymers and dye-sensitized TiO₂. *J. Appl. Phys.* **1999**, *86*, 6915-6923.
- (43) Senadeera, G. K. R.; Kitamura, T.; Wada, Y.; Yanagida, S. Deposition of polyaniline via molecular self-assembly on TiO₂ and its uses as a sensitizer in solid-state solar cells. *J. Photochem. Photobiol.* **2004**, *164*, 61-66.

- (44) Tan, S.; Zhai, J.; Wan, M.; Meng, Q.; Li, Y.; Jiang, L.; Zhu, D. Influence of small molecules in conducting polyaniline on the photovoltaic properties of solid-state dye-sensitized solar cells. *J. Phys. Chem. B* **2004**, *108*, 18693-18697.
- (45) Tan, S. X.; Zhai, J.; Wan, M. X.; Jiang, L.; Zhu, D. B. Polyaniline as a hole transport material to prepare solid solar cells. *Synth. Met.* **2003**, *137*, 1511-1512.
- (46) Liu, Z.; Zhou, J.; Xue, H.; Shen, L.; Zang, H.; Chen, W. Polyaniline / TiO₂ solar cells. *Synth. Met.* **2006**, *156*, 721-723.
- (47) Wamser, C. C.; Kim, H.-S.; Lee, J.-K. Solar cells with porphyrin sensitization. *Opt. Mater.* **2003**, *21*, 221-224.
- (48) Kim, H.-S.; Wamser, C. C. Photoelectropolymerization of aniline in a dye-sensitized solar cell. *Photochem. Photobiol. Sci.* **2006**, *5*, 955-960.
- (49) Wamser, C. C.; Kim, H.-S.; Lee, J.-K. Corrigendum to: "Solar cells with porphyrin sensitization" [Optical Materials 21 (2002) 221-224]. *Opt. Mater.* **2004**, *25*, 445.
- (50) Yanagida, S.; Yu, Y.; Manseki, K. Iodine/iodide-free dye-sensitized solar cells. *Acc. Chem. Res.* **2009**, *42*, 1827-1838.
- (51) Schmidt-Mende, L.; Grätzel, M. TiO₂ pore-filling and its effect on the efficiency of solid-state dye-sensitized solar cells. *Thin Solid Films* **2006**, *500*, 296-301.
- (52) Walter, M. G.; Wamser, C. C. Synthesis and characterization of electropolymerized nanostructured aminophenylporphyrin films. *J. Phys. Chem. C* **2010**, *114*, 7563-7574.
- (53) Li, D.; Huang, J.; Kaner, R. B. Polyaniline nanofibers: A unique polymer nanostructure for versatile applications. *Acc. Chem. Res.* **2009**, *42*, 135-145.
- (54) Huang, W. S.; Humphrey, B. D.; MacDiarmid, A. G. Polyaniline, a novel conducting polymer. Morphology and chemistry of its oxidation and reduction in aqueous electrolytes. *J. Chem. Soc., Faraday Trans.* **1986**, *82*, 2385-2400.
- (55) MacDiarmid, A. G. Polyaniline and polypyrrole: Where are we headed? *Synth. Met.* **1997**, *84*, 27-34.

- (56) MacDiarmid, A. G.; Chiang, J. C.; Halpern, M.; Huang, W. S.; Mu, S. L.; Somasiri, N. L. D.; Wu, W. Q.; Yaniger, S. I. Polyaniline: Interconversion of metallic and insulating forms. *Mol. Cryst. Liq. Cryst.* **1985**, *121*, 173-180.
- (57) Huang, J.; Kaner, R. B. A general chemical route to polyaniline nanofibers. *J. Am. Chem. Soc.* **2004**, *126*, 851-855.
- (58) Genies, E. M.; Boyle, A.; Lapkowski, M.; Tsintavis, C. Polyaniline: a historical survey. *Synth. Met.* **1990**, *36*, 139-82.
- (59) Nalwa, H. S. *Handbook of Organic Conductive Molecules and Polymers*; John Wiley & Sons Ltd., 1997; Vol. 2.
- (60) Zhang, H.; Wang, X.; Li, J.; Wang, F. Facile synthesis of polyaniline nanofibers using pseudo-high dilution technique. *Synth. Met.* **2009**, *159*, 1508-1511.
- (61) Rahy, A.; Yang, D. J. Synthesis of highly conductive polyaniline nanofibers. *Mater Lett.* **2008**, *62*, 4311-4314.
- (62) do Nascimento, G. M.; Kobata, P. Y. G.; Temperini, M. L. A. Structural and vibrational characterization of polyaniline nanofibers prepared from interfacial polymerization. *J. Phys. Chem. B* **2008**, *112*, 11551-11557.
- (63) Epstein, A. J.; MacDiarmid, A. G. Polyanilines: from solitons to polymer metal, from chemical curiosity to technology. *Synth. Met.* **1995**, *69*, 179-182.
- (64) Prigodin, V. N.; Epstein, A. J. Nature of insulator-metal transition and novel mechanism of charge transport in the metallic state of highly doped electronic polymers. *Synth. Met.* **2002**, *125*, 43-53.
- (65) Novak, M.; Kokanović, I.; Babić, D.; Baćani, M.; Tonejc, A. Variable-range-hopping exponents 1/2, 2/5 and 1/4 in HCl-doped polyaniline pellets. *Synth. Met.* **2009**, *159*, 649-653.
- (66) Beau, B.; Travers, J. P.; Banka, E. NMR evidence for heterogeneous disorder and quasi-1D metallic state in polyaniline CSA. *Synth. Met.* **1999**, *101*, 772-775.
- (67) Zimbovskaya, N. A.; Johnson, A. T., Jr.; Pinto, N. J. Electronic transport mechanism in conducting polymer nanofibers. *Phys. Rev. B: Condens. Matter Mater. Phys.* **2005**, *72*, 024213/1-024213/4.

- (68) Pelster, R.; Nimtz, G.; Wessling, B. Fully protonated polyaniline: Hopping transport on a mesoscopic scale. *Phys. Rev. B: Condens. Matter Mater. Phys.* **1994**, *49*, 12718-12723.
- (69) Li, J.; Fang, K.; Qiu, H.; Li, S.; Mao, W.; Wu, Q. Micromorphology and conductive property of the pellets prepared by HCl-doped polyaniline nanofibers. *Synth. Met.* **2004**, *145*, 191-194.
- (70) Leite, F. L.; Alves, W. F.; Mir, M.; Mascarenhas, Y. P.; Herrmann, P. S. P.; Mattoso, L. H. C.; Oliveira, O. N. J. TEM, XRD and AFM study of poly(o-ethoxyaniline) films: new evidence for the formation of conducting islands. *Appl. Phys. A: Mater. Sci. Process.* **2008**, *93*, 537-542.
- (71) Huang, J.; Kaner, R. B. Nanofiber formation in the chemical polymerization of aniline: a mechanistic study. *Angew. Chem. Int. Ed.* **2004**, *43*, 5817-5821.
- (72) Li, D.; Kaner, R. B. Processable stabilizer-free polyaniline nanofiber aqueous colloids. *Chem. Comm.* **2005**, 3286-3288.
- (73) Huang, J.; Kaner, R. B. The intrinsic nanofibrillar morphology of polyaniline. *Chem. Commun.* **2006**, 367-376.
- (74) Chiou, N.-R.; Epstein, A. J. A simple approach to control the growth of polyaniline nanofibers. *Synth. Met.* **2005**, *153*, 69-72.
- (75) Li, D.; Kaner, R. B. Shape and aggregation control of nanoparticles: not shaken, not stirred. *J. Am. Chem. Soc.* **2006**, *128*, 968-975.
- (76) Nazeeruddin, M. K.; Bessho, T.; Cevey, L.; Ito, S.; Klein, C.; De Angelis, F.; Fantacci, S.; Comte, P.; Liska, P.; Imai, H.; Graetzel, M. A high molar extinction coefficient charge transfer sensitizer and its application in dye-sensitized solar cell. *J. Photochem. Photobiol. A-Chem.* **2007**, *185*, 331-337.
- (77) Hagberg, D. P.; Edvinsson, T.; Marinado, T.; Boschloo, G.; Hagfeldt, A.; Sun, L. A novel organic chromophore for dye-sensitized nanostructured solar cells. *Chem. Commun.* **2006**, 2245-2247.
- (78) Hagberg, D. P.; Marinado, T.; Karlsson, K. M.; Nonomura, K.; Qin, P.; Boschloo, G.; Brinck, T.; Hagfeldt, A.; Sun, L. Tuning the HOMO and LUMO energy levels of organic chromophores for dye sensitized solar cells. *J. Org. Chem.* **2007**, *72*, 9550-9556.

- (79) Campbell, W. M.; Jolley, K. W.; Wagner, P.; Wagner, K.; Walsh, P. J.; Gordon, K. C.; Schmidt-Mende, L.; Nazeeruddin, M. K.; Wang, Q.; Grätzel, M.; Officer, D. L. Highly efficient porphyrin sensitizers for dye-sensitized solar cells. *J. Phys. Chem. C* **2007**, *111*, 11760-11762.
- (80) Cherian, S.; Wamser, C. C. Adsorption and photoactivity of tetra(4-carboxyphenyl)porphyrin (TCPP) on nanoparticulate TiO₂. *J. Phys. Chem. B* **2000**, *104*, 3624-3629.
- (81) Nazeeruddin, M. K.; Humphrey-Baker, R.; Officer, D. L.; Campbell, W. M.; Burrell, A. K.; Grätzel, M. Application of metalloporphyrins in nanocrystalline dye-sensitized solar cells for conversion of sunlight into electricity. *Langmuir* **2004**, *20*, 6514-6517.
- (82) Campbell, W. M.; Burrell, A. K.; Officer, D. L.; Jolley, K. W. Porphyrins as light harvesters in the dye-sensitized TiO₂ solar cell. *Coord. Chem. Rev.* **2004**, *248*, 1363-1379.
- (83) Wang, Q.; Campbell, W. M.; Bonfantani, E. E.; Jolley, K. W.; Officer, D. L.; Walsh, P. J.; Gordon, K.; Humphrey-Baker, R.; Nazeeruddin, M. K.; Grätzel, M. Efficient light harvesting by using green Zn-porphyrin-sensitized nanocrystalline TiO₂ films. *J. Phys. Chem. B* **2005**, *109*, 15397-15409.
- (84) Vlachopoulos, N.; Liska, P.; McEvoy, A. J.; Graetzel, M. Efficient spectral sensitization of polycrystalline titanium dioxide photoelectrodes. *Surf. Sci.* **1987**, *189-190*, 823-831.
- (85) Bessho, T.; Zakeeruddin, S. M.; Yeh, C.-Y.; Diau, E. W.-G.; Grätzel, M. Highly efficient mesoscopic dye-sensitized solar cells based on donor-acceptor-substituted porphyrins. *Angew. Chem., Int. Ed.* **2010**, *49*, 6646-6649.
- (86) Masuda, Y.; Ieda, S.; Koumoto, K. Site-selective deposition of anatase TiO₂ in an aqueous solution using a seed layer. *Langmuir* **2003**, *19*, 4415-4419.
- (87) Liuxue, Z.; Peng, L.; Zhixing, S. Photocatalysis anatase thin film coated PAN fibers prepared at low temperature. *Mater. Chem. Phys.* **2006**, *98*, 111-115.
- (88) Coronado, D. R.; Poot, F. P.; Oskam, G. Transformation of amorphous TiO₂ into crystalline materials. *ECS Trans.* **2006**, *3*, 47-51.
- (89) Vega, A.; Reyes, D.; Oskam, G. Application of three TiO₂ polymorphs in photoelectrochemical solar cells. *ECS Trans.* **2006**, *3*, 233-237.

- (90) Froimovitch, A.; McGarry, S.; Smy, T.; Fraser, J. Ultrahigh-surface-area anatase thin films by direct oxidation of Ti film with hydrogen peroxide. *Electrochem. Solid-State Lett.* **2007**, *10*, K11-K12.
- (91) Fang, J.; Ding, B.; Yang, Z. Synthesis of nanocrystal titania sol with different ratio of rutile and anatase at low temperature. *Solid State Phenom.* **2007**, *121-123*, 311-314.
- (92) Takayanagi, M.; Imai, Y.; Tajima, K. Characteristics of amorphous TiO₂ particles prepared in various reaction systems. *Chem. Lett.* **2007**, *36*, 876-877.
- (93) Nikkanen, J.-P.; Kanerva, T.; Mäntylä, T. The effect of acidity in low-temperature synthesis of titanium dioxide. *J. Cryst. Growth.* **2007**, *304*, 179-183.
- (94) Li, X. S.; Fryxell, G. E.; Birnbaum, J. C.; Wang, C. Effects of template and precursor chemistry on structure and properties of mesoporous TiO₂ thin films. *Langmuir* **2004**, *20*, 9095-9102.
- (95) Li, X. S.; Fryxell, G. E.; Engelhard, M. H.; Wang, C. The synthesis of cadmium doped mesoporous TiO₂. *Inorg. Chem.* **2007**, *10*, 639-641.
- (96) Deki, S.; Aoi, Y.; Hiroi, O.; Kajinami, A. Titanium (IV) oxide thin films prepared from aqueous solution. *Chem. Lett.* **1996**, *6*, 433-434.
- (97) Deki, S.; Aoi, Y. Synthesis of metal oxide thin films by liquid-phase deposition method. *J. Mater. Res.* **1998**, *13*, 883-890.
- (98) Kishimoto, H.; Takahama, K.; Hashimoto, N.; Aoi, Y.; Deki, S. Photocatalytic activity of titanium oxide prepared by liquid phase deposition. *J. Mater. Chem.* **1998**, *8*, 2019-2024.
- (99) Yamabi, S.; Imai, H. Crystal phase control for titanium dioxide films by direct deposition in aqueous solutions. *Chem. Mater.* **2002**, *14*, 609-614.
- (100) Yamabi, S.; Imai, H. Synthesis of rutile and anatase films with high surface areas in aqueous solutions containing urea. *Thin Solid Films* **2003**, *434*, 86-93.
- (101) Watanabe, T.; Hayashi, H.; Imai, H. Low-temperature preparation of dye-sensitized solar cells through crystal growth of anatase titania in aqueous solutions. *Sol. Energy Mater. Sol. Cell* **2006**, *90*, 640-648.

- (102) Nishikiori, H.; Qian, W.; El-Sayed, M. A.; Tanaka, N.; Fujii, T. Change in titania structure from amorphousness to crystalline increasing photoinduced electron-transfer rate in dye-titania system. *J. Phys. Chem. C* **2007**, *111*, 9008-9011.
- (103) Koelsch, M.; Cassaignon, S.; Ta Thanh Minh, C.; Guillemoles, J.-F.; Jolivet, J.-P. Electrochemical comparative study of titania (anatase, brookite and rutile) nanoparticles synthesized in aqueous medium. *Thin Solid Films* **2004**, *451-452*, 86-92.
- (104) Park, N.-G.; van de Lagemaat, J.; Frank, A. J. Comparison of dye-sensitized rutile- and anatase-based TiO₂ solar cells. *J. Phys. Chem. B* **2000**, *104*, 8989-8994.
- (105) Jerman, M.; Mergel, D. Structural investigation of thin TiO₂ films prepared by evaporation and post-heating. *Thin Solid Films* **2007**, *515*, 6904-6908.
- (106) Vigil, E.; Saadoun, L.; Ayllón, J. A.; Domènech, X.; Zumeta, I.; Rodríguez-Clemente, R. TiO₂ thin film deposition from solution using microwave heating. *Thin Solid Films* **2000**, *365*, 12-18.
- (107) Yang, J.; Mei, S.; Ferreira, J. M. F. Hydrothermal synthesis of nanosized titania powders: influence of tetraalkyl ammonium hydroxides. *J. Am. Ceram. Soc.* **2001**, *84*, 1696-1703.
- (108) Mahltig, B.; Gutmann, E.; Meyer, D. C.; Reibold, M.; Dresler, B.; Günther, K.; Faßler, D.; Böttcher, H. Solvothermal preparation of metallized titania sols for photocatalytic and antimicrobial coatings. *J. Mater. Chem.* **2007**, *17*, 2367-2374.
- (109) Lee, S.-W.; Drwiega, J.; Wu, C. Y.; Mazyck, D.; Sigmund, W. M. Anatase TiO₂ nanoparticle coating on barium ferrite using titanium bis-ammonium lactato dihydroxide and its use as a magnetic photocatalyst. *Chem. Mater.* **2004**, *16*, 1160-1164.
- (110) Möckel, H.; Giersig, M.; Willig, F. Formation of uniform size anatase nanocrystals from bis(ammonium lactato)titanium dihydroxide by thermohydrolysis. *J. Mater. Chem.* **1999**, *9*, 3051-3056.
- (111) Gutiérrez-Tauste, D.; Zumeta, I.; Vigil, E.; Hernández-Fenollosa, M. A.; Domènech, X.; Ayllón, J. A. New low-temperature preparation method of the TiO₂ porous photoelectrode for dye-sensitized solar cells using UV irradiation. *J. Photochem. Photobiol. A-Chem.* **2005**, *175*, 165-171.

- (112) Uekawa, N.; Kajiwara, J.; Kakegawa, K.; Sasaki, Y. Low temperature synthesis and characterization of porous anatase TiO₂ nanoparticles. *J. Colloid Interface Sci.* **2002**, *250*, 285-290.
- (113) Oekermann, T.; Zhang, D.; Yoshida, T.; Minoura, H. Electron transport and back reaction in nanocrystalline TiO₂ films prepared by hydrothermal crystallization. *J. Phys. Chem. B* **2004**, *108*, 2227-2235.
- (114) Zhang, D.; Yoshida, T.; Furuta, K.; Minoura, H. Hydrothermal preparation of porous nano-crystalline TiO₂ electrodes for flexible solar cells. *J. Photochem. Photobiol. A-Chem.* **2004**, *164*, 159-166.
- (115) Imai, H.; Morimoto, H.; Tominaga, A.; Hirashima, H. Structural changes in sol-gel derived SiO₂ and TiO₂ films by exposure to water vapor. *J. Sol-Gel Sci. Technol.* **1997**, *10*, 45-54.
- (116) Winder, C.; Matt, G.; Hummelen, J. C.; Janssen, R. A. J.; Sariciftci, N. S.; Brabec, C. J. Sensitization of low bandgap polymer bulk heterojunction solar cells. *Thin Solid Films* **2002**, *403-404*, 373-379.
- (117) Theander, M.; Inganaes, O.; Mammo, W.; Olinga, T.; Svensson, M.; Andersson, M. R. Photophysics of substituted polythiophenes. *J. Phys. Chem. B* **1999**, *103*, 7771-7780.
- (118) Sariciftci, N. S.; Heeger, A. J. Role of Buckminsterfullerene, C₆₀, in organic, polymeric, photoelectric devices. *Proc. SPIE* **1995**, *2530*, 76-86.
- (119) Sariciftci, N. S.; Heeger, A. J. Photophysics of semiconducting polymer-C₆₀ composites: a comparative study. *Synth. Met.* **1995**, *70*, 1349-52.
- (120) Guenes, S.; Neugebauer, H.; Sariciftci, N. S. Conjugated polymer-based organic solar cells. *Chem. Rev. (Washington, DC, U. S.)* **2007**, *107*, 1324-1338.
- (121) Pivrikas, A.; Sariciftci, N. S.; Juska, G.; Osterbacka, R. A review of charge transport and recombination in polymer/fullerene organic solar cells. *Prog. Photovoltaics* **2007**, *15*, 677-696.
- (122) Tiwana, P.; Parkinson, P.; Johnston, M. B.; Snaith, H. J.; Herz, L. M. Ultrafast terahertz conductivity dynamics in mesoporous TiO₂: Influence of dye sensitization and surface treatment in solid-state dye-sensitized solar cells. *J. Phys. Chem. C* **2010**, *114*, 1365-1371.

- (123) Mihailetschi, V. D.; Xie, H.; de Boer, B.; Koster, L. J. A.; Blom, P. W. M. Charge transport and photocurrent generation in poly(3-hexylthiophene): Methanofullerene bulk-heterojunction solar cells. *Adv. Funct. Mater.* **2006**, *16*, 699.
- (124) Micaroni, L.; Nart, F. C.; Hümmelgen, I. A. Considerations about the electrochemical estimation of the ionization potential of conducting polymers. *J. Solid State Electrochem.* **2002**, *7*, 55-59.
- (125) Zhang, D. On the conductivity measurement of polyaniline pellets. *Polym. Test.* **2007**, *26*, 9-13.
- (126) Bissessur, R.; White, W.; Dahn, D. C. Electrical characterization of conductive polymers and their intercalated nanocomposited with molybdenum disulfide. *Mater Lett.* **2006**, *60*, 248-251.
- (127) *Inorganic Crystal Structure Database*. <http://www.fiz-karlsruhe.de/jcsd.html> Accessed 09/14/10,
- (128) Williamson, G. K.; Hall, W. H. X-ray line broadening from fcc aluminum and tungsten. *Acta Metall.* **1953**, *1*, 22-31.
- (129) Trivedi, D. C. In *Handbook of Organic Conductive Molecules and Polymers*; Nalwa, H. S., Ed.; Wiley: Chichester, NY, 1997; Vol. 2. Conductive Polymers: Synthesis and Electrical Properties, p 509-510.
- (130) Wu, C.-G.; Chiang, C.-H.; Jeng, U.-S. Phenol assisted deaggregation of polyaniline chains: Simple route to high quality polyaniline film. *J. Phys. Chem. B* **2008**, *112*, 6772-6778.
- (131) Duić, L.; Mandić, Z. Counter-ion and pH effect on the electrochemical synthesis of polyaniline. *J. Electroanal. Chem.* **1992**, *335*, 207-221.
- (132) Huang, J.; Kaner, R. B. Flash welding of conducting polymer nanofibers. *Nat. Mater.* **2004**, *3*, 783-786.
- (133) Li, D.; Xia, Y. Welding and patterning in a flash. *Nat. Mater.* **2004**, *3*, 753-754.
- (134) Huang, J.; Virji, S.; Weiller, B. H.; Kaner, R. B. Polyaniline nanofibers: facile synthesis and chemical sensors. *J. Am. Chem. Soc.* **2003**, *125*, 314-315.

- (135) Posdorfer, J. R.; Werner, B.; Wessling, B.; Heun, S.; Becker, H. In *Organic Light-Emitting Materials and Devices VII*; Kafafi, Z. H., Lane, P. A., Eds. Bellingham, WA, 2004; Vol. 5214, p 188-196.
- (136) van der Pauw, L. J. A method of measuring specific resistivity and Hall effect of discs of arbitrary shape. *Philips Res. Rep.* **1958**, *13*, 1-9.
- (137) Kim, H.-S.; Hobbs, H. L.; Wang, L.; Rutten, M. J.; Wamser, C. C. Biocompatible composites of polyaniline nanofibers and collagen. *Synth. Met.* **2009**, *159*, 1313-1318.
- (138) Porter, T. L.; Minore, D.; Sykes, A. G. Counterion and dopant induced effects on the structure of electropolymerized polyaniline thin films. *J. Vac. Sci. Technol. A* **1995**, *13*, 1286-1289.
- (139) Zhang, X.; Chan-Yu-King, R.; Jose, A.; Manohar, S. K. Nanofibers of polyaniline synthesized by interfacial polymerization. *Synth. Met.* **2004**, *145*, 23-29.
- (140) Gilbert, A.; Baggott, J. In *Essentials of Molecular Photochemistry*; CRC Press: Boca Raton, 1991, p 84-87.
- (141) Li, W.; Wamser, C. C. Synthesis and characterization of interfacially polymerized films of tetraphenylporphyrin derivatives. *Langmuir* **1995**, *11*, 4061-4071.
- (142) Murata, K.; Ito, S.; Takahashi, K.; Hoffmann, B. M. Photocurrent from photocorrosion of aluminum electrode in porphyrin/Al Schottky-barrier cells. *Appl. Phys. Lett.* **1997**, *71*, 674-676.
- (143) Gregg, B. A.; Pichot, F.; Ferrere, S.; Fields, C. L. Interfacial recombination processes in dye-sensitized solar cells and methods to passivate the interfaces. *J. Phys. Chem. B* **2001**, *105*, 1422-1429.
- (144) Kay, A.; Grätzel, M. Artificial photosynthesis. 1. Photosensitization of TiO₂ solar cells with chlorophyll derivatives and related natural porphyrins. *J. Phys. Chem.* **1993**, *97*, 6272-6277.
- (145) Kay, A.; Humphry-Baker, R.; Grätzel, M. Artificial photosynthesis. 2. Investigations on the mechanism of photosensitization of nanocrystalline TiO₂ solar cells by chlorophyll derivatives. *J. Phys. Chem.* **1994**, *98*, 952-959.